DISSERTATION

LAGRANGIAN MIXING AND TRANSPORT IN HURRICANES

Submitted by

Blake Rutherford

Department of Mathematics

In partial fulfillment of the requirements

For the Degree of Doctor of Philosophy

Colorado State University

Fort Collins, Colorado

Spring 2010

COLORADO STATE UNIVERSITY

March 29, 2010

WE HEREBY RECOMMEND THAT THE DISSERTATION PREPARED UNDER OUR SUPERVISION BY BLAKE RUTHERFORD ENTITLED LAGRANGIAN MIXING AND TRANSPORT IN HURRICANES BE ACCEPTED AS FULFILLING IN PART REQUIREMENTS FOR THE DEGREE OF DOCTOR OF PHILOSOPHY.

<u>Committee on Graduate Work</u>

Michael Kirby

Patrick Shipman

Wayne Schubert

Advisor: Gerhard Dangelmayr

Department Head: Gerhard Dangelmayr

ABSTRACT OF DISSERTATION

LAGRANGIAN MIXING AND TRANSPORT IN HURRICANES

This study examines the role of transport and mixing in the dynamics of tropical cyclones from a mathematical viewpoint and their implications for intensity. While this topic has seen extensive study, much of it has lacked the mathematical rigor allowed by a new class of Lagrangian techniques, which allow the study of particle transport through time-dependent flows. Lagrangian coherent structures (LCS's) are time-dependent boundaries which partition the flow into distinct regions, controlling the systematic transport of material between regions. In this study, the mathematics of Lagrangian transport is developed, and adapted to several tropical cyclone models. Three models are utilized to study mixing; the axisymmetric model of Rotunno and Emanuel (1987), the nondivergent barotropic 2D model of Schubert et al. (1999), and the 3D Penn State-NCAR mesoscale model (MM5). For the study of mixing on the axisymmetric model, a new class of mixing rates is proposed which vary in initial time and integration time, and it is shown that mixing events precede changes in intensity. For the nondivergent barotropic model, orthogonal flow separation reveals coherent structures that are persistant through strong shear, and mixing is quantified through the shear during mesovortex interaction. The extension of the orthogonal separation methods to 3D provides a method for decomposing Lagrangian hyperbolicity from shear. The method is applied to the MM5 model to find the Lagrangian eye-eyewall interface (LEEI), which is responsible for dictating transport between the two regions. A new ridge extraction algorithm is used to extract the 2D manifolds of the 3D Lagrangian fields. By extending and automating this algorithm across varying initial time, a time-dependent and spatially smooth representation of the LEEI in terms of Fourier descriptors and radial basis functions is computed. The dynamics of the time-dependent LEEI indicate that the higher wavenumber asymmetries vanish, but the lower wavenumber asymmetries remain, quantifying the degree of axisymmetry in the storm from a transport perspective. The last study applies the new 3D techniques to an intensifying storm by studying the interaction of vortical hot towers (VHT's). VHT's are shown to not only be coherent structures, but to be associated with hyperbolic LCS's which play an important role in their interaction and in the formation of an eyewall. The length of the LCS's indicate that the VHT's have impact on a broad range that affects environmental flow into the primary vortex.

Blake Rutherford
Department of Mathematics
Colorado State University
Fort Collins, Colorado 80523
Spring 2010

ACKNOWLEDGMENTS

I would first like to thank Prof. Gerhard Dangelmayr for his incredible amount of work as my advisor. In addition to being an exceptional mathematician, Gerhard is a great person and advisor. He has spent an incredible amount of time and energy teaching the mathematics that was neccessary for this work, proposing new paths for this research, and reviewing the output in great detail. Gerhard's involvement has had a very positive impact on this work and in my development as a mathematician. His patience and professionalism through this process is greatly appreciated.

The members of my committee were instrumental in providing insight and motivation through this study.

I would like to thank Prof. Wayne Schubert for his help on this work. I appreciate his careful reading of manuscripts, and the formulation of ideas.

I would like to thank Prof. Michael Kirby for his ideas in the areas of data reduction and time-series analysis, and for providing the computers neccessary for this study.

It was an honor to have had the opportunity to work with Prof. Dan Rudolph. His enthusiasm for mathematics was umsurpassed, and I will miss his support. I would like to thank Prof. Patrick Shipman for stepping in on my committee, and for his organization of the dynamics seminar, which provided a good place to present ideas.

Much of this work came from ideas in the CSU math hurricane research group. There were many people involved in this group that helped with the ideas in this study, both at CSU and at the Naval Postgraduate School (NPS).

I would like to thank John Persing for his help in relating many of the mathematical ideas to an atmospheric framework, and for providing the data used in the computations in this work.

I would also like to thank Michael Montgomery for his role in this study. Mike has collaborated with the CSU group extensively, and was always quick to point out the important meteorological aspects that we needed to consider.

There were many others who also had a role in this effort as a part of the research group.

Among these are Eric Hendricks, Kate Musgrave, Jonathan Vigh, Christopher Rozoff, and Arthur Jamshidi from CSU and Michael Riemer from NPS. I would also like to thank Saraubh Bharve and Van Sang Nguyen from NPS for providing data.

I would also like to acknowledge the National Science Foundation for their support of this interdisciplinary work, through NSF cooperative agreement ATM-0715426.

DEDICATION

For my wife Tisza, who supported me all the way through this.

Contents

List of Figures

List of Tables

Chapter 1

Introduction

The study of the tropical cyclone (TC) dynamics is a topic that is very important to society, since the destruction caused by these storms has a huge cost and impacts many people. TC's have tremendous impact on global shipping, and on the lives of residents of coastal communities, where damage from high winds and storm surges have enormous economic and social consequences. The related areas of storm tracking, intensification, and storm formation all share the benefits from additional knowledge of the storms, and more directed future research may help each of these areas.

There have been many studies in atmospheric science about hurricanes, which have led to a greater understanding of them. Many of the studies have focused on tracking and prediction, while other studies have focused on the structure, physics, and thermodynamics of the heat engine that drives the storms. The area of intensification has also seen extensive work from researchers, but a lack of plane flights and data measurements has limited knowledge of this process. While these are generally considered separate areas of hurricane research, advances in understanding storm structure lead to better prediction of intensity and tracking.

1.1 Cyclogenesis

The study of cyclogenesis, or the transition from a tropical depression to a tropical cyclone, is important for many reasons. Understanding a storm in its early stages and determining whether it will intensify allows cost savings and efficiency in other research by providing the locations for field data measurements, which are limited in availability. More and earlier data would certainly be of use for storm tracking and prediction.

A key theory in the study of cyclogenesis was recently proposed by [DMW09] and termed *marsupial theory*. This study basically asserts that tropical storms are more likely to transition into hurricanes if the warm core of the storm is protected from outside environmental influences, enabling an upscale organization within a warm core to occur. Flow dividing streamlines are proposed as the mechanism that prohibits the interaction of the core with outside air masses, which deprive the storm of energy and moisture. The concept of a dividing streamline provides a connection between the fields of meteorology and dynamical systems, where invariant manifolds have seen extensive study. While the study offers a simple explanation for the neccessary conditions for tropical cyclogenesis, *marsupial theory* is unproven due to the fact that the structures observed in the developing storms are seen from an Eulerian view, which lacks the ability to make inferences about the very complex time-dependent flows that characterize hurricanes. The structures that dictate the transport of material through the time-dependent flow of a hurricane can be validated by Lagrangian methods, and may help to validate *marsupial theory*.

1.2 Models

Since storm data is difficult to obtain, the use of models is very common in meteorology. Models have several advantages over real data, including smaller data sets, the ability to control parameters, and a reduction in the dimension of the data.

Interest in the dynamics of hurricanes has motivated the use of dimensionally reduced models, which limit the complexity of the flow geometry, and perhaps as important, the size of the data sets. There are many 2-dimensional models that are used in both research and prediction. Notably, the axisymmetric model of [RE87] produces an axisymmetric vortex and provides wind and thermodynamic data in the radial and vertical directions. Also, the planar model of [SMT^{+}99], and studied by [KS01] and [KE01], provides a 2D nondivergent flow to study vortex evolution and interaction, and is important for its simplicity in viewing a polygonal eyewall formation.

Though more complex, a number of 3D models have been developed. For this study, the fifth generation Penn State/NCAR mesoscale model (MM5), described by [GDS95] and [Dud93], will be used for the generation of 3D velocity and thermodynamic variables.

1.3 Lagrangian mixing

In the different studies of hurricanes, the mathematical sophistication is at a limited level with respect to the time variation of the flow. Almost every study of hurricanes views properties of the storm at a fixed time, and the data from that time is used to make inferences about the entire system, see [SMT+99]. This is known as a Eulerian reference frame. Since hurricanes show significant temporal variation, a moving reference frame, or Lagrangian frame is more useful for examining structures within a time-dependent system.

The field of Lagrangian dynamics has only recently (in the last 20 years) seen significant advances, likely because time-dependent fluid flows require massive amounts of data to completely analyze. The use of powerful computers has allowed the study of Lagrangian dynamics, and has driven the theory in recent years.

There are two primary influences on the field of Lagrangian dynamics. The work of Stephen Wiggins and George Haller both appeared in about 1997, and took different paths to understanding fluid mixing in time-dependent velocity fields. Wiggins took the approach of extending the ideas of a hyperbolic fixed point and manifolds to a time-dependent flow, while Haller took the approach of directly computing the manifolds, which led to efficient algorithms for manifold detection.

The work of Wiggins centered on the idea of a distinguished hyperbolic trajectory (DHT) for time-dependent flows, [MW98]. Analagous to a hyperbolic fixed point for steady flows, the DHT was shown to have stable and unstable manifolds that remain invariant to particle transport and partition the flow. Time-dependence of the velocity field allows intersections of the manifolds. Lobes form between adjacent intersection points and are bounded by a segment of the stable and unstable manifold. The study of lobe dynamics completely characterized the transport of fluid for velocity fields with bounded aperiodic time-dependence, and may characterize mixing in geophysical flows [CW00] and [MW98] if the velocity field has sufficiently bounded temporal and spatial variation. Algorithms used to detect DHT's, [ISW02], are often numerically stable in flows with general but bounded time dependence. Applications of lobe dynamics to fluid motion across a jet is studied by [RMPJ99] and [DW96].

The work of Haller is mostly devoted to understanding hyperbolic separation through the behavior of nearby trajectories, [HP97], [Hal00], and [Hal01a]. The definition of finite-time Lyapunov exponents (FTLE's) as a measure of Lagrangian flow separation led to efficient algorithms for direct computation of manifolds for time-varying velocity fields, [Lek03, LL04]. FTLE's measure the relative separation as a grid of trajectories is integrated. Regions with high FTLE values, or ridges of the FTLE field are the finite-time manifolds. The work of Haller has been extended and many properties of the FTLE's proven, such as invariance of the manifolds, and robustness of the method under velocity errors and approximations [Hal02]. This work has transformed the field of computational fluid dynamics with applications to a variety of fluid flows, including oceanographic, atmospheric, and aerodynamic flows.

The methods of Haller have led to many similar methods, including finite-size Lyapunov exponents (FSLE's) [KL02, GRH07], total instability time, and relative dispersion, [HMG01]. The varying methods have contrasting advantages and disadvantages for flows with different aspect ratios, temporal variation, or divergence.

The work of Haller motivated the use of statistical methods to characterize mixing. The work of Antonsen [AJFOGL96], and related work by [ABC+97], [VHG02], and [VTSG03] have used the statistical distributions of the Lagrangian fields developed by Haller.

A key part of the class of methods developed by Haller is the ability to extract ridges from scalar fields to view manifolds. Ideas from differential geometry have been used by Mathur et al. [MHP+07] and Shadden [Sha06] to extract ridges. Additional studies in visualization of coherent structures have been done by [GGTH07], [GRH07], and [TMH+09]. The link between image processing and dynamical systems is still very new and will certainly be a topic of much future research.

Though the applications of Haller's work are very impressive given their relative age, few studies have applied any of the methods to atmospheric flows. There are basically three reasons why this is the case. Atmospheric data sets are generally very large, and the computing power neccessary for a detailed Lagrangian analysis has not been readily available. There is also a lack of interdisciplinary research between atmospheric scientists and mathematicians. A key reason, which will be addressed here, is that the methods have deficiencies when applied to sheared flows, which are often present in atmospheric flows, and are ubiquitous within tropical cyclones.

1.4 Contents

This study is an attempt to merge the fields of dynamical systems, image processing, and atmospheric science to gain a greater understanding of the mechanisms of transport and mixing in hurricanes. Because of the difficulty in separating the mathematical and atmospheric work involved in this study, the organization will be first divided along the separate atmospheric results. New mathematical ideas are presented in each study, and will be addressed along with their physical meaning for hurricanes. Chapter 2 will be used to discuss the preliminary atmospheric ideas and the body of atmospheric literature devoted to mixing and transport in tropical cyclones. Chapter 3 will introduce the preliminary mathematical ideas from dynamical systems in a very general time-dependent setting, and will introduce the key ideas of Wiggins and Haller. Some basic ideas from differential geometry and image processing that will be useful for the visualization of structures will also be included.

The next five chapters will be separate studies of the mechanisms of hurricane mixing. These studies have all resulted in submitted refereed papers. Work on all of these studies has been done with the help of coauthors. In particular, Gerhard Dangelmayr has helped extensively in each work, and has ensured the mathematical quality of the studies, and with the writing of results. His help has been crucial in the formulation of many of the ideas. Michael Kirby has also helped on the mathematical parts of some studies. The atmospheric aspects of this paper have come from the ideas of research generated by collaboration with Michael Montgomery, Wayne Schubert, and John Persing. Their work on the atmospheric implications and interpretation of the mathematical results have greatly aided in the combining of these separate fields.

The atmospheric studies begin in Chapter 4 with a study on the mechanisms of mixing in an axisymmetric hurricane model. The model is a 2D representation of a hurricane with vertical and radial wind fields. Methods of Antonsen [AJFOGL96] and Huber [HMG01] are extended to a difficult domain and over varying initial time to compute time-varying mixing rates. The rates are then correlated to measures of intensity to show that eye-eyewall mixing correlates to intensity and precedes fluctuations in intensity, suggesting that local eye bouyancy is responsible for changes in intensity. Results from this study have been published in *Atmospheric Chemistry and Physics Discussions*, [RDP$^+$09] and are under review for publication in *Atmospheric Chemistry and Physics*.

Chapter 5 is the study of radial mixing on a 2D nondivergent barotropic model, which exhibits high shear and forms a polygonal eyewall before a breakdown into a monopole. The methods of [HI03] are used, and extended to detect hyperbolic lines that persist through shear. The conclusions that coherent structures can persist through shear becomes important for many aspects of hurricane research, while the methods used in this study motivate the ideas that are used in the 3D studies. Results from this study have been published in *Atmospheric Chemistry and Physics*, see [RDP+10].

In Chapter 6, the 2D shear decomposition is extended to 3D, and the methods applied to the 3D MM5 model. A Lagrangian eye-eyewall interface is found that provides a definition of the eye-eyewall boundary in relation to particle transport. A maximal persistent shearing surface is found to reside outside the eye-eyewall interface. The surfaces are extracted with a surface extraction algorithm that is built on ridge extraction algorithms. Results from this study have been submitted to *Quarterly Journal of the Royal Meteorological Society*, see [RD09].

An extension of the fields from Section 6 to varying initial time provide a time-varying eye-eyewall boundary, in Chater 7. An algorithm based on the Fourier descriptors of the Lagrangian fields is developed to automate the surface extraction algorithm across varying initial time. The dynamics of the time-dependent structures are then studied, along with a method for data reduction and inferences on the axisymmetric nature of the storm. Results from this study are in preparation for publication.

Chapter 8 deals with the application of the new mathematical methods to an intensifying hurricane, and the structures involved in vortical hot tower interaction are observed and classified. Their relation to environmental structures ties together many important theories from atmospheric science in a rigorous mathematical framework. Results from this study are in preparation for publication.

Concluding remarks and an outlook for future studies are given in Chapter 9.

Chapter 2

Tropical Cyclones

The atmospheric studies in this work are motivated by work on hurricanes that suggests that mixing and transport are important in the evolution and formation of hurricanes. Because the scope of the word mixing is very broad, specific definitions of mixing must be used in the different contexts. At a basic level, differential advection, or the transport of trajectories, must be differentiated from turbulent diffusion, which is nearer to true mixing. In fact, advective mixing boundaries are important for prohibiting transport. Measuring diffusive mixing can be seen as quantifying the degree of uncertainty within a system, while advective mixing reduces the complexity on certain spatio-temporal scales. Another way of viewing the advective and diffusive processes is by the time scale that governs the mixing. Advection takes place on a short time scale, and is affected by the local flow geometry, whereas diffusion is a property that is generally more representative of an entire system in the limit of long times.

This study is generally concerned with advective mixing, which is equivalent to the location and classification of storm boundaries and structures, such as an eyewall or rainband formation. Lagrangian methods may be used to find structures within the time-dependent velacity fields of hurricanes. The location of eye-eyewall structures has been addressed by many studies on hurricane models, see e.g. [SMT$^+$99, KE01, LH82, Mur86], and in observations of real storms, where structures similar to those in the models such as polygonal eyewalls have been observed in Hurricanes Hugo (1989), [BM91], and Gilbert,[BW92].

2.1 Structure

Many studies apply directly storm structure, which concerns the interaction and location of separate storm regions. The eye and eyewall make up the inner core of the hurricane, where the maximal vorticity and winds are located in the eyewall, which surrounds the still dry air of the eye. The heaviest moisture is located outside of the eyewall in rainbands. A low-level inflow is the greatest source of fuel for the storm, while the material that rises through the eyewall exits the storm through an upper level outflow. Additional structures that may be considered include outside air masses that may interact with the core.

Larger scale environmental studies provide the neccessary conditions for storm development, including studies by Roll, [Rol65], and Smagorinsky, [Sma63], which provide a view of the tropical atmosphere and ocean interactions. Studies involving the interaction of storms with environmental flow were the subject of [FR99] and [FR01].

2.1.1 Eye-eyewall structure

A considerable number of studies have considered eye-eyewall structure, [Ema97, Bra02], or thermodynamics of the inner core, [BE98, BE97]. Structural and thermodynamic properties play a key role in the transport of material and energy between the inner core regions.

2.1.2 Wave disturbances and shear

Shear is a factor that is present in all vortices, and is marked by the sliding of layers of particles across each other. The sliding induces wave disturbances called Rossby waves to form. The growing disturbances can lead to transport across shearing regions, and may be responsible for the formation of polygonal eyewall structures. There have been many studies in hurricanes that have dealt with Rossby waves, including [ME98] and [ML97] which show the importance of Rossby waves in the formation of asymmetries.

2.1.3 Symmetry and asymmetry

A dominant wavenumber Rossby wave disturbance can sometimes occur in the vortex, which can be seen as a structural deformation of the vortex as a polygonal vortex boundary. For an intensifying storm, many wavenumber disturbances are present, including high wavenumbers. As the storm intensifies, the high wavenumber asymmetries vanish first, leaving the low wavenumber asymmetries. The behavior of the low wavenumber asymmetries is important for the evolution of the inner core, [RMMJG99], and has implications for maximum intensity and tracking, [SIM95].

2.1.4 Mixing

There are two main classes of interaction that we consider in this study, the inner core mixing between the eye and eyewall, and large scale environmental interaction. The time scales for the two types of behavior are quite different, and are generally addressed by different methods and time scales, see e.g. [RH97].

Inner core mixing is believed to have an impact on hurricane intensity through energy transfer. The heat exchange between the regions and induced convection, [BE98, Ema97], is seen as one path to intensification. Inner core mixing is the topic of studies by [ZY02] and [SMZ05], which promotes local buoyancy and its role in enhancing the overall energy as a reason for intensification. Local buoyancy in the eye can transition to the eyewall, providing fuel to the updraft, [Bra02]. The thermodynamic properties of the eye have been discussed in [Wil01]. A Lagrangian view of eye-eyewall transport was the subject of [CPMB07] and showed that trajectory transport between all inner core regions does occur. The implications of eye-eyewall mixing on hurricane intensity have been studied by [PM03] and [MBAB06]. Inner core interaction with the environment was studied by [ENB94].

The role of wave instabilities also play a role in inner core mixing. Vortex Rossby waves generated by shear instabilities may induce transport across regions, [ME98]. Wave interaction in the inner core has also been studied by [CY01] and [CBY03].

2.1.5 Intensity

The interaction of a storm with the environment is also important for the TC lifecycle, as the introduction of additional air masses may certainly impact the storm, [RMB05]. For example, the introduction of a second air mass representing vertical wind shear will weaken the storm, [RMN09]. Other studies have focused on the role of environmental features and their interaction with the inner core, see for example [FR99, FR01]. The maximum intensity of hurricanes has been studied by [PM03] and [RE87].

2.1.6 Formation

Cyclogenesis occurs during the early stages in the TC lifecycle as a storm gains energy and vorticity, often originating from regions of deep convection, [FJ69]. Both convective heating, [HJLB09], and Rossby waves, [ME98], play a role in intensification. However, there are two main paths to cyclogenesis that have seen recent interest, the interaction of vortical hot towers (VHT's), and wind induced surface heat exchange (WISHE).

VHT's are localized convective structures with high vorticity, that are observed during TC intensification [HMD04] in tropical atmospheres by [FJ69] and [RMB05]. The interaction of the structures is shown to have an effect on intensification by the mixing of vorticity, entropy, and angular momentum through their interaction and by providing local buoyancy to the storm, [MNCS06].

The role of WISHE in TC intensification is investigated in the studies of [SMN09] and [MNSP09]. The specific heat of ocean water carries more energy than the air, and is supposed to increase the overall energy within a storm by an exchange of energy into the low-level atmosphere.

Additional studies in the intensification of TC's are conducted with model data, including [MVD02] and [NSM08]. The use of a reduced dimensional model for predictability was studied by [SS08].

2.2 Gaps between atmospheric science and mathematics

While many studies examine the thermodynamic and vorticity mixing, the true nature of mixing within time-dependent flows requires new Lagrangian techniques. So far, there has been little collaboration between dynamical systems and hurricane researchers, which has limited the use of the new methods in meteorological applications. There are three main areas where ideas from mathematics could aid future meteorological results, the use of time-dependent trajectory analysis, the implications of time-dependent structures on transport, and the use of fully 3D techniques.

2.2.1 Fixed time assumptions

In autonomous flows, the streamlines of the velocity field partition the flow. Under the assumption that the velocity field is steady, the concept of a flow dividing manifold is identical to that of a general trajectory. There are many atmospheric studies which utilize phase diagrams from a steady velocity field to portray the motion of trajectories within the unsteady flow. For example, the study of [DMW09] shows the structures that protect the inner core during formation from outside air masses as streamlines from a steady velocity field. The ideas from this study provide an extremely important theory in the formation of hurricanes, but many of the results could be further validated with the use of more rigorous mathematics.

2.2.2 Eulerian measures

Many atmospheric studies use Eulerian assumptions in analyzing mixing. The studies of [SMT+99], [KS01], and [KE01], investigate mixing in a nondivergent barotropic model by viewing the mixing of vorticity, which is nearly conserved. Particle separation is analyzed through the Eulerian measure of the Okubo-Weiss criterion. Trajectory computations indicate that the time-scale on which trajectories follow the Okubo-Weiss criterion is only a few minutes. A Lagrangian version of the Okubo-Weiss criterion has been shown to provide a better indication of particle separation for time-dependent flows, but many of the current Lagrangian methods even show improvements over the Lagrangian Okubo-Weiss criterion, and are more suitable for the hurricane models, but have not been applied before this study. [DMW09] showed structures that are involved in the interaction between the inner core and environmental flow, but it is still unclear if the structures can exist in the time-dependent velocity field.

2.2.3 Reduced dimension representation

Many atmospheric studies have utilized reduced dimensional models, notably the studies of [SMT+99] and [KE01] which used the nondivergent barotropic model to study polygonal eyewall formation. While the reduced dimensions are very useful for analyzing shear and Rossby-wave disturbances, which occur dominantly in the horizontal plane along lines of shear, it becomes neccessary to investigate 3D structures within real storms due to the influences of heating and convection.

Many of the studies in Lagrangian mixing are presented first in a 2D setting, and then extended to 3D. There are many reasons why most Lagrangian fluid studies have not used fully 3D velocity fields. The algorithms are not as easy to implement, and require substantially more computing power in 3D. Also, the manifolds in a 3D setting become 2D, which greatly adds to the complexity. Lastly, visualization of 3D structures is a very challenging task, and is itself an area of active research.

2.2.4 Lack of collaboration

Lagrangian methods have been used in some atmospheric studies, but have thus far been limited due to the lack of collaboration between atmospheric scientists and mathematicians, and the size of atmospheric data sets. So far, the studies of [KL02], [JL01], [HMG01], and [TMH+09] have been the most noted applications of Lagrangian techniques to atmospheric studies. Currently, few mathematicians have access to atmospheric data sets, though a greater focus on interdisciplinary research will certainly improve accessibility.

Chapter 3

Lagrangian Mixing Preliminaries

Mixing is a term that is subject to broad interpretation. In atmospheric dynamics, mixing of physical quantities such as temperature and moisture is often studied. In this study, the interest is on the interaction of particle trajectories, which are solutions of the differential equation associated with a velocity field $\mathbf{u}(\mathbf{x}, t)$.

$$\dot{\mathbf{x}} = \mathbf{u}(\mathbf{x}, t) \tag{3.1}$$

with the initial condition

$$\mathbf{x}(0) = \mathbf{x}_0. \tag{3.2}$$

Trajectories are advected under the time T flow map

$$\mathbf{x}_0 \mapsto \phi_{t_0}^{t_0+T}(\mathbf{x}_0) = \mathbf{x}(t_0 + T). \tag{3.3}$$

The evolution of trajectories under this map will be important for the study of the dynamics of both 2D and 3D velocity fields. To begin the discussion of flow boundaries and stability, we assume that the velocity field is 2D.

3.1 Steady flows

A flow is steady if it has no time dependence,

$$\dot{\mathbf{x}} = \mathbf{u}(\mathbf{x}). \tag{3.4}$$

A point $\mathbf{x}_f$ is called a fixed point of $\mathbf{u}$ if $\mathbf{u}(\mathbf{x}_f) = 0$, that is $\mathbf{x}_f$ is held constant under the flow map. The local flow is governed by the Jacobian $\nabla\mathbf{u}(\mathbf{x})$. The eigenvalues of the Jacobian determine the stability of $\mathbf{x}_f$. If the eigenvalues of the Jacobian are of opposite signs, then a fixed point is said to be hyperbolic.

Associated with hyperbolic fixed points are 1-dimensional sets, which are solutions of (3.4), that are exponentially attracted or repelled from the fixed point. The attracting set is called the stable manifold, while the unstable set is called the unstable manifold. Note that the only intersection of the stable and unstable manifolds is at the hyperbolic fixed point. The manifolds partition the flow, that is trajectories do not cross the manifolds.

3.2 Time-periodic flows

If the flow is time-periodic, $\mathbf{u}(\mathbf{x}, t+p) = \mathbf{u}(\mathbf{x}, t)$, the fixed point of the Poincare return map emits stable and unstable manifolds, whose transverse intersections form enclosed regions called lobes. The movement of lobes governs the transport of traectories.

3.3 Time-dependent flows

3.3.1 Hyperbolicity and DHTs

Assume a velocity field over a finite time interval is given by

$$\frac{d}{dt}\mathbf{x}(t) = \mathbf{u}(\mathbf{x}, t),\ \ t \in [t_0, t_L] \tag{3.5}$$

Hyperbolicity is a linear property since the characteristics of a hyperbolic trajectory are determined from the linearized velocity field

$$\frac{d}{dt}\boldsymbol{\xi} = \frac{d\mathbf{u}}{d\mathbf{x}}(\mathbf{x}(t), t)\boldsymbol{\xi},\ \ t \in [t_0, t_L] \tag{3.6}$$

To define hyperbolicity, we define exponential dichotemy, which means the nearby trajectories seperate at an exponential rate. Let $X(t, t_0)$ be the fundamental matrix solution to the linearized system (3.6), i.e. the matrix where columns that are linearly independent solutions of the linear system:

$$\dot{\mathbf{x}} = A(t)\mathbf{x}, \tag{3.7}$$

where $A(t) = \frac{d\mathbf{u}}{d\mathbf{x}}(\mathbf{x}(t), t)$ is an $n \times n$ matrix continuous in t.

Def. 1 Exponential Dichotemy

The linearized system is said to have *exponential dichotemy* on $[t_0, t_L]$ if there exists a projection matrix P, i.e. $P^2 = P$ and positive constants K, L, α, and β such that

$$|X(t)PX^{-1}(s)| \leq Ke^{-\alpha(t-s)},\ s \leq t < \infty \tag{3.8}$$

$$|X(t)QX^{-1}(s)| \leq Le^{-\beta(s-t)},\ s \geq t > -\infty \tag{3.9}$$

where $Q = I - P$ and I is the indentity matrix.

We now look at what it means for a trajectory to be hyperbolic. Let $\mathbf{x}_h(t)$ be a trajectory of (3.5). Then $\mathbf{x}_h(t)$ is said to be hyperbolic if the linearized system given by (3.6) has exponential dichotemy over the time interval (t_0, t_L).

For a given velocity field, there can be an infinite number of hyperbolic trajectories. A DHT or distinguished hyperbolic trajectory is the trajectory that does not experience exponential growth or decay as $t \to \infty$.

3.3.2 Nonlinear flows

Let the velocity field have the form

$$\frac{d}{dt}\mathbf{y} = D\mathbf{y} + \mathbf{g}^{(NL)}(\mathbf{y}, t) \tag{3.10}$$

where $D \in \mathbb{R}^{n \times n}$ is a constant diagonal matrix which gives a time independent part, and $\mathbf{g}^{(NL)}(\mathbf{y}, t) \in \mathbb{R}^n$ is the time-dependent nonlinear part.

Def. 2 DHT

A trajectory $\mathbf{x}_{dht}(t)$ is a DHT for (3.10) if it satisfies:

1. It is hyperbolic

2. There exists a region R in the phase space such that the DHT remains in R for all time, and all other trajectories starting in R leave R in finite time either forward or backward.

3. It is not contained in the chaotic invariant set created by the intersections of stable and unstable manifolds of another hyperbolic trajectory.

Generally, DHT may not be unique. Instead, associated with a particular DHT is a region R in which no other DHT's can exist. The region R has significance for the stable and unstable mainfolds as well. Points that are on the unstable manifold leave R forward in time, while points on the stable manifold leave R backward in time and points that are not on either manifold or the DHT leave R both forward and backward in time.

3.3.3 General time dependence

A DHT can also be defined in terms of the general velocity field given by (3.5). Assume there is an invertible coordinate change from $\mathbf{x}$ to $\mathbf{y}$ such that (3.5) is transformed into (3.10), and let $\mathbf{y}_{dht}(t)$ satisfy the properties of Definition 2. Then $\mathbf{y}_{dht}(t)$ is a DHT of (3.10), and $\mathbf{y}_{dht}(t)$ corresponds to a trajectory $\mathbf{x}_{dht}(t)$ which is a DHT of (3.5). The coordinate change and algorithms for computing DHT's are provided by [MW98], while algorithms for computing the stable and unstable manifold of a hyperbolic trajectory are given by [ISW02, MSWI03, MSW04]. The methods have been applied to geophysical flows with aperiodic time dependence by [DW96, CW00, RMPJ99, Wig05, PH99]. Because the velocity fields in TC's have very strong time dependence, the algorithms often fail, but the studies still provide the theoretical framework for advective mixing in time-dependent flows.

In the case that a velocity field has aperiodic time dependence, there are in general no hyperbolic fixed points. However, at a fixed time t, the velocity field may show instantaneous stagnation points (ISP's), denoted $\mathbf{x}_{sp}(t)$, which are fixed points of the velocity field at fixed time t. If the time dependence is small, then there may be a point $\mathbf{x}_{dht}(t)$, related to $\mathbf{x}_{sp}(t)$, which is a particle trajectory that maintains hyperbolic stability. The hyperbolic trajectory emits stable and unstable manifolds which are time-dependent, and may have intersections at points other than at the hyperbolic trajectory.

Wiggins introduced lobe dynamics as a method for measuring the flux across boundaries. A separatrix is a flow boundary formed by continuous segments of stable and unstable manifolds. Lobes are enclosed regions formed by a single segment of a stable and unstable manifold, and adjacent intersection points. As the manifold segments evolve, the separatrix may be deformed, and lobes may pass across the separatrix boundary. Since the lobes are invariant, the material contained within the lobe remains in the lobe, and is transported across the boundary.

3.4 Alternative methods for time-dependent flows

In flows with general time-dependence, the velocity field may not show persistent ISP's, so DHT's related to ISP's may not exist, or the numerical algorithms of [MW98] and [ISW02] may not converge. In this case, the manifolds of hyperbolic trajectories may exist, and may still form a tangle that is responsible for the transport of trajectories. The difference between flows with general time-dependence and steady flows is that the manifolds of time-dependent flows are of finite length, since they can be computed over only finite time.

A class of scalar field methods was developed by Haller and coauthors, [Hal01a, HY00, HP97], which compute the relative separation of sets of nearby trajectories seeded on a uniform grid and integrated for finite times. In this approach the manifolds are seen as ridges of the scalar fields. Many variations of the scalar field methods exist and show similar stretching properties.

3.4.1 FTLE's

Haller defined the finite-time Lyapunov exponents (FTLE's), [Hal01a], as a means for determining trajectory separation. The closely related direct Lyapunov exponent (DLE) was defined by [HP97, HY00]. The field of FTLE's measures maximal stretching [SLM05]. Consider an infinitesimal perturbation $\mathbf{x}_0'$ of the point $\mathbf{x}_0$. After a time T, the perturbation becomes

$$\begin{aligned} \mathbf{x}'(t_0+T) &= \phi_{t_0}^{t_0+T}(\mathbf{x_0}+\mathbf{x_0'}) - \phi_{t_0}^{t_0+T}(\mathbf{x}_0) \qquad (3.11) \\ &= \frac{d\phi_{t_0}^{t_0+T}(\mathbf{x}_0)}{d\mathbf{x}_0}\mathbf{x}_0' + \mathcal{O}(\|\mathbf{x}_0'\|^2). \qquad (3.12) \end{aligned}$$

To find the magnitude of the growth rate of the perturbation, we drop the $\mathcal{O}(\|\mathbf{x}_0'\|^2)$ term and take the Euclidean norm

$$\|\mathbf{x}'(t_0+T)\| = \sqrt{\langle \mathbf{x}_0', \Delta \mathbf{x}_0' \rangle} \qquad (3.13)$$

where the matrix

$$\Delta = \frac{d\phi_{t_0}^{t_0+T}(\mathbf{x_0})^*}{d\mathbf{x_0}} \frac{d\phi_{t_0}^{t_0+T}(\mathbf{x_0})}{d\mathbf{x_0}} \qquad (3.14)$$

(the asterisk denotes the transpose of a matrix or vector) is symmetric and gives a finite time representation of the Cauchy-Green deformation tensor. If $\|\mathbf{x}_0'\|$ is held constant, the maximal expansion occurs when $\mathbf{x}_0'$ is aligned with the eigenvector corresponding to the largest eigenvalue, $\lambda_{max}(\Delta)$, of Δ,

$$\begin{aligned} \max_{\mathbf{x}_0'} \|\mathbf{x}'(t_0+T)\| &= \sqrt{\lambda_{max}(\Delta)}\|\mathbf{x}_0'\| \\ &= \exp\left(\sigma_{t_0}^{t_0+T}(\mathbf{x}_0')|T|\right)\|\mathbf{x}_0'\|, \end{aligned}$$

where

$$\sigma_{t_0}^{t_0+T}(\mathbf{x}_0) = \frac{1}{2\,|T|} \log \lambda_{max}(\Delta) \qquad (3.15)$$

is the largest finite time Lyapunov exponent for the integration time T at the point $\mathbf{x}_0$ at initial time t_0. The FTLE is computed forward ($T > 0$) and backward ($T < 0$) in time, which allows detection of forward time repelling and attracting material lines, respectively.

An initial grid of seeded trajectories can be advected to give a scalar field of FTLE values dependent on initial-time. High FTLE values correspond to large separation of trajectories. Ridges of FTLE fields are defined as Lagrangian coherent structures (LCS's) and are shown to be invariant by [SLM05], and may form separatrices which govern transport. The extraction of all ridges from a time varying FTLE field is still a difficult problem, but the structures are often obvious from visual inspection. FTLE's are easily computed and have shown important flow boundaries in many time-dependent geophysical flows, see e.g. [SIJ08], [JW02], and [dFHG04].

For computation of the FTLE field, the flow gradient $\frac{d\phi_{t_0}^{t_0+T}(\mathbf{x_0})}{d\mathbf{x}_0}$ can be calculated on a uniform grid of trajectories

Many of the efforts in dynamical systems for ridge extraction hinge on the ideas of gradient climbing. Given a scalar field $\phi(\mathbf{x})$, trajectories of the gradient dynamcal system

$$\dot{\mathbf{x}} = \nabla\phi(\mathbf{x}), \tag{3.16}$$

evolve towards ridges of ϕ before they are attracted by local maxima along slow manifolds. An alternative formulation of the gradient dynamical system was given by [MHP$^+$07]. Points converge onto ridges through gradient climbing, which makes it useful for visualization of ridges in 2D. However, the points evolved from a set of initial conditions are not ordered, making it difficult to measure transport, and eventually they cluster around maximal values instead of residing on the ridge. Criteria to stop gradient climbing yield some improvement, but do not solve the clustering problem for noisy scalar fields. Multiple ridges within a field, which is common for discretely defined turbulent flows, pose additional challenges to gradient climbing. Scale space ridges, [Lin98], offer an automated alternative, but the method has the shortcoming of not providing exact ridges. The ridge extraction problem is still an area of active research and vital for accurately quantifying transport.

Volume rendering methods compute level surfaces to visualize ridges, however the surfaces obtained are often crude approximations to a true ridge. Advanced methods of surface extraction are used in the analysis of MRI's and ultrasound data by researchers in medical imaging, see e.g. [TPGB00], but the adaptation to time-varying fields and the collaboration between researchers in computer imaging and dynamical systems is still lacking.

Since Lagrangian fields depend on an initial time, time variation leads to a series of scalar fields containing manifolds. Identifying ridges across sets of images must also be considered as a part of the ridge extraction process. In 2D, ultrasound techniques show promise, as do hierarchal clustering algorithms.

3.5 Convergence

Because of the large number of trajectory integrations required to produce scalar fields, especially over a moving time frame, covergence of the Lagrangian methods deserves consideration. [HI03] provide an orthogonal version of FTLE's and suggest faster convergence than FTLE's. [KL02] computed FSLE's for the stratospheric polar vortex and suggest that the convergence of FSLE's may be faster than FTLE's for atmospheric or other divergent flows. Studies by [GGTH07] and [TCH10] show that improvements in the FTLE algorithm may be achieved by refining the grid mesh during integrations, or by predefining the directions of initial separation based on velocity data information.

Though the manifolds are of finite length for time-dependent fields, using less model data and shorter integration times produce fewer ridges in the case of high time-dependence, which may allow easier interpretation of outputs. Thus, resolving ridges under shorter integration times is also an important issue for consideration.

3.6 Shear

All of the previously discussed Lagrangian methods assume that the manifolds have hyperbolic stability. Hyperbolic separation occurs in a direction not aligned with the Lagrangian velocity, while shear separation occurs in the direction of the Lagrangian velocity. Several studies have viewed transport through shear, including [Sam92] and [DW96], which computed transport across jets in flows with small time-dependence. [Hal01a] and [Hal05] offer partitions of the domain into hyperbolic, elliptic, or parabolic stability.

The effect of shear is different from that of hyperbolicity by its effects on a vector aligned orthogonal to the Lagrangian velocity. Hyperbolic stretching lengthens the vector in the direction orthogonal to the Lagrangian velocity, while shear involves a rotation of the vector toward the Lagrangian velocity direction. A decomposition of shear from hyperbolicity through the solutions of a transformed variational equation was done by [HI03]. The existence of hyperbolic structures that persist through shear is important for tropical cyclone dynamics, and is a main focus of this study.

Other studies have attempted to distinguish hyperbolicity from shear. McIntyre, [McI80], provided the notion of a generalized Lagrangian mean as a method of subtracting the shear from the velocity fields, but the methods are computationally difficult and may not be suitable for dominant shear.

3.7 Vortices

Vortices are structures commonly seen in hurricanes on many scales, from the storm as a whole to mesoscale VHT's during intensification, as well as small vortices that are shed during Rossby wave disturbances. Dynamically, vortices have elliptic or neutral stability. The eigenvalues associated with the orthogonal separation are small, as is the degree of rotation of a normal vector. Haller [Hal05] provides Lagrangian stability for vortices. Several additional papers are devoted to the dynamics of vortices, [Tru54, Saf81, Sha92, SL92], and their entrainment of particles, [DG04, ECL02, CK94], which plays a key role in intensification, [DMW09]. The study of vortices has been extended to the Lagrangian frame by [SDM06]. Interaction between vortices is crucial to the interaction of VHT's, and has been studied by [Pro99, SL02, YM02, VT80], while vortex crystals have been studied by [FCFD95].

Chapter 4

Lagrangian mixing in an axisymmetric hurricane model

4.1 Summary

This chapter discusses the extension of established Lagrangian mixing measures to make them applicable to data extracted from a 2D axisymmetric hurricane simulation. Because of the non-steady and unbounded characteristics of the simulation, the previous measures are extended to a moving frame approach to create time-dependent mixing rates that are dependent upon the initial time of particle integration, and are computed for nonlocal regions. The global measures of mixing derived from finite-time Lyapunov exponents, relative dispersion, and a measured mixing rate are applied to distinct regions representing different characteristic feautures within the model. It is shown that these time-dependent mixing rates exhibit correlations with maximal tangential winds during a quasi-steady state, establishing a connection between mixing and hurricane intensity.

4.2 Background and overview

The question of the interaction between different characteristic regions of a hurricane, in particular the eye, eyewall, and near-core, is considered of fundamental importance in the study of structure and intensity, [FR99], [FR01], [KE01], [KS01], [SMT$^+$99], [Wil01]. In particular, mixing in the lower troposphere at the eye-eyewall interface, [CPMB07], [MBAB06], [PM03], has been proposed to play an important role for intensification. The proposed mechanisms are either direct and mechanical or indirect and thermodynamic. Direct and mechanical mechanisms reduce intensity as air with low absolute angular momentum from the eye is stirred to the radius of maximum winds (RMW). Indirect and thermodynamic mechanisms stir air with high entropy from the eye to the eyewall that will generate enhanced local buoyancy, [SMZ05], [Bra02], [ZY02], leading to an enhanced energetic cycle for the hurricane as a whole (e.g. as a modified heat cycle). Maximum tangential winds (found in the eyewall generally at $z \approx 1$ km) will be used here as the principal measure of intensity.

Mixing in hurricanes is often viewed in an Eulerian manner, based on the instantaneous velocity fields. If the velocity fields are time varying, the Eulerian structures may not be representative of the actual particle motion. In recent work in fluid dynamics, time dependent Lagrangian hyperbolic invariant manifolds have been studied that partition the domain into distinct regions and are visualized as ridges of Lagrangian scalar fields, [HP97], [Hal02], [Hal00], [HY00], see Chapter 5 for a recent application to a 2D hurricane-like vortex model. Most of these studies are for time-varying 2D velocity fields in closed and bounded domains. An extension of the use of these methods to the 3D case is given by [GRH07]. In this chapter we investigate a 2D flow that is more complicated because the domain is unbounded and there is an inflow and outflow. Lagrangian structures associated with boundaries have been identified by [Hal04] and [SH08], and generally differ from the Eulerian separation points.

Statistical measures of Lagrangian mixing have been applied to 2D fluid models by [VTSG03] and [AJFOGL96], but the mixing characteristics are time-dependent only in the sense that they vary with the integration time. While this is sufficient for steady or periodic velocity fields, in general time-varying velocity fields there is also a significant dependence on the initial time at which the trajectories are seeded. This holds for all statistical measures used so far, including relative dispersion, which has been used to diagnose atmospheric mixing by [HMG01] in a limited way in a global circulation problem.

In this chapter we apply Lagrangian techniques to study mixing in the axisymmetric hurricane model of [RE87]. The model of the hurricane shows the principal structures of 3D hurricanes (e.g., eye, eyewall updraft, near-surface inflow, and outflow jet), while resolving the 2D velocity fields in the radial and vertical directions. The advantages of axisymmetric models are that the size of the problem is reduced and the geometry is simpler. The structures found to be characteristic for the mixing processes within an axisymmetric model may, with caution, be extended to give clues about mixing within 3D models or reality. The model of [RE87] yields time-dependent 2D velocity fields that show complex spatial and temporal variation about a quasi-steady state, leading to a variety of dynamically interesting, time-dependent structures . The fluid is not incompressible, which is assumed in the derivation of many measures of mixing, and the domain is unbounded, which presents a challenge in the implementation of many techniques currently used to compute such measures. The temporal complexity of the velocity fields makes the extraction of coherent structures difficult, as structures may have very short times of existence.

Given the complexity and time-dependent nature of the velocity field in the Rotunno and Emanuel model, it is neccessary to develop a hybrid (local-global) approach to measuring mixing rates. Local Eulerian flow structures are generally not valuable for characterizing mixing in the entire flow if the structures do not exist in a coherent manner. However, global measures of mixing are not suitable for this model either, because much of the mixing occurs around the eyewall updraft region, which is where the maximum winds occur. Outer environment and eye behavior are very separate processes from the mixing that occurs in and around the updraft, hence diagnosing the mixing for the entire domain from a single measure is not reasonable. Most current methods are either local or global.

Local methods established in the Lagrangian frame study particular features such as hyperbolic trajectories and their stable and unstable manifolds, and track the effects of these features. Global measures attempt to define a rate of mixing that is representative of the entire system. In the axisymmetric hurricane model used in this study, the strong time dependence makes structures too complicated to distinguish after several minutes, and their mixing properties are lost. To diagnose mixing in a domain that has distinct mixing regions, which have little interaction with other regions, we adapt both local and global mixing diagnostics to quantify mixing between nonlocal regions. The nonlocality of the regions requires extracting mixing measures from ensembles of trajectories, which makes these measures statistical in nature.

Our approach to solving the hurricane mixing problem will be guided by considering time and space dependence of mixing processes. The dynamically distinct regions of hurricanes (e.g., the eye, the eyewall, near-core, etc.) require that the space dependence of mixing properties follows a regional approach. The domain is partitioned into regions, and a mixing rate is calculated for each region, giving a spatial dependence to the mixing rates.

For general time dependence, not only variations in the integration time, but also variations in the initial time have to be used to define the mixing rates. The result is a time series of mixing rates computed for each spatial region. The initial time-dependent mixing rates are then compared with measures of intensity to establish correlations between these characteristic quantities. The correlation analysis shows that the mixing rates computed for some of the regions are sigificantly correlated with the maximum tangential winds.

A mixing rate is a measure of how quickly an initial tracer in a fluid becomes homogenized. The homogenization process has been studied for autonomous or time-periodic velocity fields in bounded and closed domains, and gives a mixing rate for the entire system. This rate can be compared to other rates derived from measures of advection or diffusion. The time dependence of the axisymmetric model makes diffusion very difficult to measure because the filamentation that occurs with a diffusive process undergoes bifurcations as soon as the filaments develop. Advective measures of mixing converge fast in integration time making them more suitable for this model. Since this follows from particle trajectories, the associated mixing rates are Lagrangian in nature, and measure the interaction of features that move with the flow.

The outline of the chapter is as follows. Section 4.3 gives an overview of current Lagrangian mixing rates. In Section 4.4 we describe the characteristics of the axisymmetric model that is used for this study. The adaptation of current methods to make them applicable to our non-steady and open fluid-flow problem, along with the numerical methods used is described in Section 4.5. The results of our study are presented in Sections 4.6-4.9. In Section 4.6 we show and discuss the Lagrangian scalar fields. Section 4.7 gives a Lagrangian characterization of the eye-eyewall interaction, and Section 4.8 shows how the Lagrangian structures are related to low and high intensity steady state approximations. In Section 4.9, we analyze correlations between measures of intensity and mixing rates. A discussion and conclusions are given in Section 4.10.

4.3 Overview of current Lagrangian methods

Lagrangian mixing measures have advantages over Eulerian measures for their applicability to time dependent fluid flows. For time dependent flows, trajectories may cross Eularian boundaries, and diverge from instantaneous features of the flow. Lagrangian techniques capture the total separation of trajectories and provide structures that are invariant under the flow. The current methods can generally be classified as either local and global. The local techniques quantify the local rate of stretching of an initial area element. Places with the highest stretching give time dependent manifolds, which are invariant and determine the local transport properties by following the manifolds through the flow. These techniques are useful for incompressible flows where the velocity field varies slowly both in space and time. Some of the local techniques currently in use are finite-time Lyapunov exponents, [Hal00], [Hal02], [HP97] and direct Lyapunov exponents, [HY00]. Distinguished hyperbolic trajectories have been studied by [Hal01a], [ISW02], and [SIJ08]. Finite-size Lyapunov exponents have been used by [ABC+97], [dFHG04], and [GRH07], and applied in a study of [KL02] to the stratospheric polar vortex. Relative dispersion was studied by [HMG01] to diagnose transport in the troposphere.

Global Lagrangian techniques provide representative mixing characteristics of an entire domain, without exact extraction of structures, and are statistical in nature. Global mixing measures have been applied to flows in bounded domains with no dominant flow characteristics, and with with no general time dependence. The global measures are related to the homogenization of a tracer within the domain, and are usually extensions of local measures to the entire domain. The measured mixing rate determines how fast the tracer is homogenized, [VTSG03]. Another global mixing rate is defined through the distribution of the values of finite-time Lyapunov exponents, and is an extension of the local measure of advection to the entire domain, see [AJFOGL96].

4.3.1 Measured mixing rate (MMR)

The mixing rate of a system can be measured by calculating the rate at which an initial tracer becomes homogenized by the flow. Let

$$\mathbf{x_0} \mapsto \phi_{t_0}^{t}(\mathbf{x_0}) \tag{4.1}$$

be the flow map from time t_0 to time t associated with a 2D non-steady velocity field $\mathbf{v}(\mathbf{x}, t)$, that is, the solution of $\dot{\mathbf{x}} = \mathbf{v}(\mathbf{x}, t)$ with initial condition $\mathbf{x}(t_0) = \mathbf{x}_0$. If an initial tracer is planted uniformly over a subdomain at time t_0 and evolved, then the variance of the tracer concentration should decay over time as the tracer fills the entire domain. If $\rho_0(\mathbf{x})$ is the initial tracer density at time t_0, and $\rho(t, t_0, \mathbf{x}) = \rho_0(\phi_t^{t_0}(\mathbf{x}))$ the tracer density at time t, then the variance $\Sigma_\rho(t, t_0)$ of ρ should decay exponentially over time and thus can be modeled by

$$\Sigma_\rho(t, t_0) = A_0 e^{-r|t-t_0|} + A_1. \tag{4.2}$$

The relaxation constant r is called the measured mixing rate (MMR), [VTSG03]. The use of $|t - t_0|$ accounts for both forward and backward time integration, which allows comparison to other Lagrangian methods utilizing forward and backward integration times. It is assumed here that r is representative of the entire system, and the initial tracer profile is not important in a long enough integration time, since the positions of fluid particles in a closed domain eventually become indistinguishable with respect to their initial conditions. For the non-autonomous axisymmetric model, we make this rate space and time dependent by varying the initial spatial region R in which trajectories are seeded, as well as the initial time t_0.

For R we choose regions in the eye, eyewall updraft, and the boundary layer inflow, which are representative of particular features of the flow. These regions have very different mixing properties, and different associated mixing rates. Since the fluid in this model does not eventually become homogenized, the mixing rate is a measure of how trajectories characteristic of a certain feature disperse, e.g. become advected through a jet. Trajectories that enter the eyewall updraft exit the domain through the upper level outflow jet, so there are many trajectories that exit the domain in finite time, and there are large regions of the domain that trajectories from the core will not enter. To accomodate this trajectory behavior, a finite-time version of the mixing rate is used here. Trajectories are advected for an integration time such that they remain within the spatial domain. The mixing rate $r(R, t_0)$ then approximates the long time scalar variance decay by the homogenization over a short time. We note that for flows that do not eventually reach a homogenized state, the *degree* of homogenization, $A_1/(A_0 + A_1)$, can be a relevant measure of mixing. This measure is different from the *rate* r of homogenization in that it measures how clustered the set remains as it is advected.

Finite-time Lyapunov exponents have been introduced in Chapter 3.4.1. While the exact extraction of LCS's as ridges of the FTLE-field is generally not possible, FTLE's still give the total separation of trajectories within a region, and the statistical distribution of FTLE values allows definition of global mixing rates. [AJFOGL96] have shown that for autonomous or time-periodic velocity fields in closed and bounded domains, the variance of a tracer coincides with the quantity

$$G(t,t_0) = \int \sigma^{(1/2)} e^{-\sigma t} P(\sigma,t,t_0) d\sigma, \tag{4.3}$$

where $P(\sigma,t,t_0)$ is the probability distribution function of the FTLE values. For non-steady velocity fields in open domains this coincidence cannot be expected, but still the function $G(t)$ may show a similar exponential decay like the tracer variance. Thus, assuming that $G(t)$ has the form

$$G(t) = A_0' e^{-r'|t-t_0|} + A_1', \tag{4.4}$$

we can solve numerically for r' to obtain a predicted FTLE mixing rate (FMR), [AJFOGL96]. This rate is meant to measure the advective mixing processes determined by initial trajectory separation, and does not account for the diffusive processes that govern the long time mixing. However, the integration time, T, used must be sufficiently long so that the FTLE's resolve LCS's, and performing integrations in a moving time frame within a finite time range imposes an upper bound on T. The optimal integration time will be discussed in more detail in Section 4.5.

The FMR method was originally designed for closed bounded domains and steady or time-periodic velocity fields, see [VTSG03] for an application to a time-periodic velocity field with chaotic trjectories. Since the axisymmetric model has general time dependence, and important mixing properties are localized in time and space, we adapt this measure to include initial time dependence and initial space dependence. The resulting time series of mixing rates are then compared to the time series of the measured mixing rates, and to measures of intensity.

4.3.2 Relative dispersion (RD)

Relative dispersion is based on the average displacement of an ensemble of initially proximate trajectories from a mean particle position, [HMG01]. When an ensemble is taken to be a well defined set of trajectories, relative dispersion can differentiate between sets of initial conditions that have different mixing properties. For a set R with an ensemble of initial conditions $\mathbf{x}_0 \in R$, the root mean squared (RMS) displacement of the ensemble of trajectories seeded at time t_0 in R is defined as

$$\sigma(t) = \langle \|\mathbf{x}(t) - \overline{\mathbf{x}}(t)\|^2 \rangle^{\frac{1}{2}}, \tag{4.5}$$

where $\langle . \rangle$ denotes the average over the set, and $\overline{\mathbf{x}}$ is the mean particle position. The relative dispersion $K(t)$ is defined by

$$K(t) = \frac{1}{2}\frac{d}{dt}\sigma^2(t), \tag{4.6}$$

and $\sigma(t)$ has either a power law relationship for $t \to t_0$, [HMG01],

$$\sigma(t) \propto |t - t_0|^{\gamma}, \tag{4.7}$$

or an exponential relationship for large $t - t_0$,

$$\sigma(t) \propto \exp\left(\gamma|t - t_0|\right). \tag{4.8}$$

For an initial set the relative dispersion is dependent on the time scales at which mixing occurs. For a given integration time $T = t - t_0$, we consider the relative dispersion (RD) as a function of an initial set R, and the initial time t_0, $K(R, t_0)$.

4.3.3 Relative dispersion from FTLE's (FRD)

While FTLE's and relative dispersion are similar measures of trajectory separation, the FMR is not directly comparable to the RD in their given forms. To allow a comparison between the FTLE mixing rate and relative dispersion, we define the RMS displacement of an ensemble of trajectories in the direction of maximal expansion through the FTLE values by

$$\begin{aligned} D_{t_0}^{t}(R) &= \left\langle \exp(2\sigma_{t_0}^{t}(\mathbf{x})|t - t_0|)\right\rangle^{1/2} && (4.9) \\ &\propto |t - t_0|^{\gamma'}, && (4.10) \end{aligned}$$

which gives a power γ' for $t \to t_0$. The FTLE based relative dispersion (FRD) is then defined by

$$K_f(t) = \frac{1}{2}\frac{dD^2}{dt}(t), \tag{4.11}$$

and is, for the integration time $T = t - t_0$, considered as a function of the region R and t_0, similar to the RD. The FRD can be considered as an average stretching factor for an ensemble of trajectories.

4.4 Model overview

The axisymmetric, nonhydrostatic, cloud-resolving hurricane model of [RE87] is integrated on a staggered C grid using a fixed radial (3.75 km) and fixed vertical (312.5 m) grid spacing at one-fourth the originally published grid spacing. Ice physics are not simulated and explicit convection is employed using a fixed precipitation fall speed of 7 ms^{-1}. Subgrid-scale turbulence is parameterized using a modified [Sma63] formulation with horizontal mixing length of 750 m. Radiation is simply represented by Newtonian relaxation to the initial basic state potential temperature profile with a cooling rate capped at 2 K day^{-1}. A sponge layer is provided above the model tropopause. Surface fluxes of momentum and enthalpy are conducted with a bulk aerodynamic formulation with the ratio of drag and enthalpy coefficients set to unity and the drag allowed to vary with wind speed by Deacon's formula, [Rol65]. The initial sounding is that of 4x run by [PM03]. Data output is at a two-minute interval starting with a time (day 13) when a quasi-steady intensity ($\approx$ 85 m s^{-1}) is reached for the simulation.

The (u,w)-flow (in the radial/vertical plane of motion) (shown in Fig. 4.1 at t = 400 min.) has several dominant characteristics which are often separated by lines of high shearing. The main feature is the axisymmetric eyewall. It appears as a slanted, vertically oriented structure that separates from the sea surface at approximately r=20 km, and goes upward to a maximum height of z=15 km. Inside of the eyewall is the eye which has very slow velocities. The eyewall updraft takes trajectories upward and is separated from the eye by a line of high vertical shearing. The boundary layer inflow is the main source of material that enters into the updraft. As material moves through the updraft, it enters the upper level outflow, where it goes outward and leaves the domain. There is also a midlevel inflow that brings material inward. This inflow is not as strong as the boundary layer inflow, and trajectories that enter through this inflow mix into the updraft through a tangle of hyperbolic manifolds.

4.5 Numerical methods

Mixing rates are computed by adapting the techniques from Section 4.2 to seeded sets of trajectories. Trajectories are advected in radius and height through a fourth order Runge-Kutta method. Since the locations of seeded particles do not become eventually homogenized throughout the entire domain and some trajectories leave the domain, the initial locations of particles become important.

Trajectories are seeded into initial boxes, which are representative regions for different aspects of the flow (Fig. 4.2). The boxes are placed in the low level inner core region of the

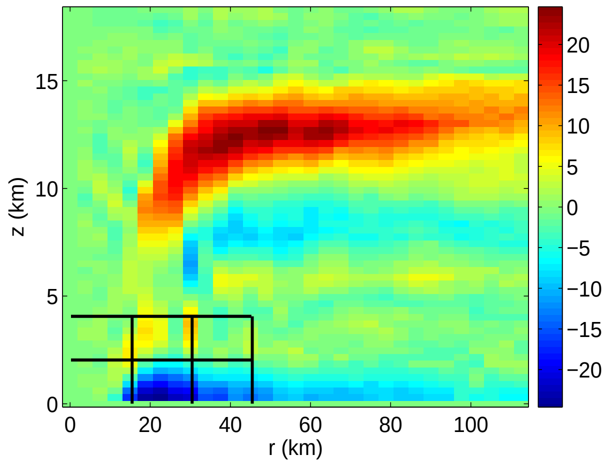

(a)

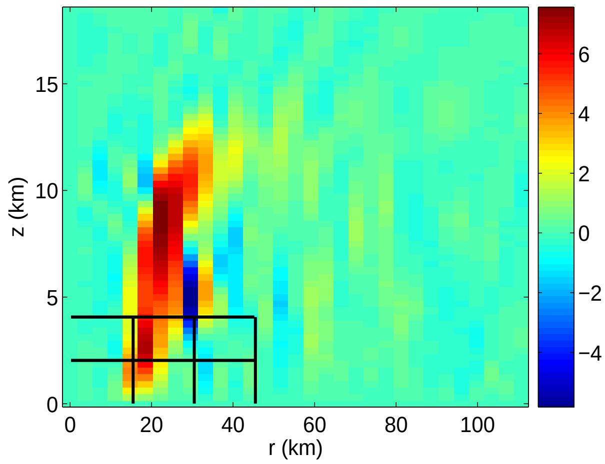

(b)

Figure 4.1: Velocity fields at t=400 min. Radial velocity field (a) and vertical velocity field (b) with boxes used for computing mixing rates in the lower left of each image.

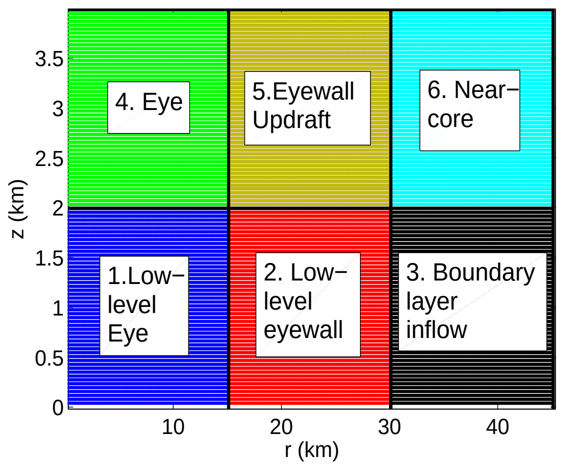

Figure 4.2: Locations of boxes in the lower inner core.

hurricane. The boxes approximately split the eye and eyewall updraft (Fig. 4.1(b)), with two boxes in the vertical direction used to distinguish boundary layer properties from other low level properties. The split between the eye and eyewall updraft boxes in the radial direction is placed at the approximate location of the 1 m/s vertical wind contour. Two additional boxes are placed outside the eyewall to capture the processes in the boundary layer inflow for the lower box, and hyperbolic convective processes in the near-core for the upper box.

Trajectories are seeded in the initial boxes at a resolution of 64 times model resolution in the radial direction and 8 times in the vertical direction, giving 256 by 50 total trajectories for each box. The same resolution of trajectories is used for the computation of the FTLE fields, which gives a balance between clear ridges and computational expense.

The MMR requires the computation of a trajectory density, which is measured for a given box as the ratio of the number of trajectories in the box at a given time divided by the total number of initial trajectories starting in the given seed box. For counting the number of final trajectories, we have divided the entire domain into a 8 vertical by 20 horizontal grid of boxes of the same size as the six representative boxes, allowing trajectory movement into a domain of 16 km height by 300 km radius. The variance is then computed from the density in all final boxes.

For a fixed initial time, the mixing rates from the concentration and from FTLE fields both follow an exponential decay as a function of integration time. The mixing rate limit A_1 is determined by taking the minimum concentration variance over the finite integration time, and the initial value $A_0 + A_1$ is the initial variance. The MMR r is found by taking the log of the time-series $\Sigma_\rho(t) - A_1$, where A_1 is 90% of the minimum value of $\Sigma_\rho(t)$, and the slope of the linear function is found using a linear least-squares best fit. The concentration variance Σ_ρ, $\log \Sigma_\rho(t, t_0)$, and the standard deviation of the error for the best fit over the time interval $(t_0, t_0 + T)$ are shown in Fig. 4.3 as functions of T.

For the FMR, the initial value $A_0' + A_1'$ is determined by the initial FTLE distribution, while the limit A_1' is again determined by taking 90% of the minimum value of $G(T)$ over the integration times. The mixing rate r' is determined in the same manner as the MMR (Fig. 4.4).

The relative dispersion $K(t, t_0, R)$ is computed for the initial sets given by the six initial boxes. Because of the aspect ratio of the atmosphere, radial dispersion will factor more strongly into the K measure than vertical dispersion. The FRD is computed from the FTLE values in the six initial boxes to compute an effective RMS displacement. By varying initial time, time-series of mixing rates can be compared to time-series of maximum winds (shown below). The integration time is also varied to view the short and long time aspects of the dispersion.

4.6 Lagrangian fields

The Lagrangian fields were calculated for a variety of integration times to capture short and long time mixing processes. Lines of high FTLE values in both the forward and backward time fields mark a transition region between the eye and eyewall (Figs. 4.5,4.6). The FTLE's do not distinguish well between stretching and shear because they are computed over a finite time. Moreover, the eigenvalues of the symmetric tensor $\frac{d\phi}{d\mathbf{x}}$ are associated with directions varying along trajectories, whereas shear in particular is associated with distance growth in the direction tangential to trajectories. Trajectories originating in the eyewall updraft reach a radius of 140 km in the outflow in 120 minutes, where the outflow jet[1] governs the mixing, and the low level effects cannot be seen.

There are several factors to consider in the choice of integration time. The integration time must be chosen long enough so that the LCS's are resolved, and so that the decay functions $\Sigma_\rho(t_0, T)$ and $G(t_0, T)$ begin to show an exponential decay. Since the methods aim

[1] The cores of jets show low mixing regions (blue) in the FTLE field as there is very little relative advection of neighboring trajectories there. Jets are bounded by high shear regions, which lead to large relative advection (red) and large FTLE values.

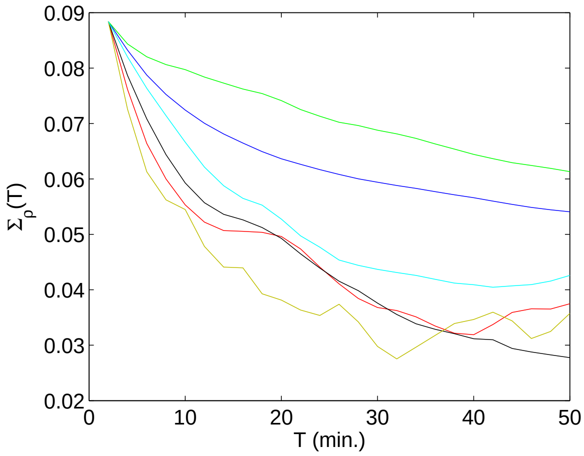

(a)

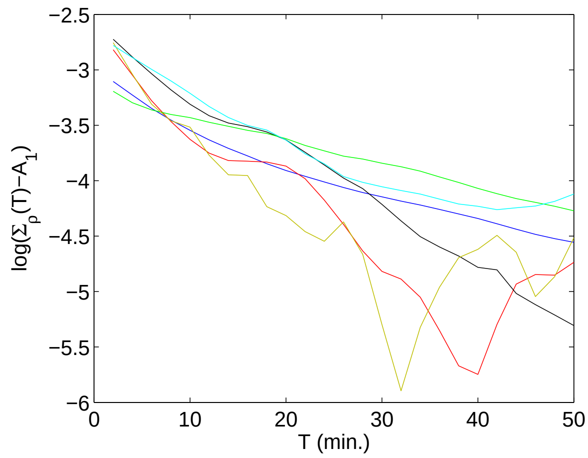

(b)

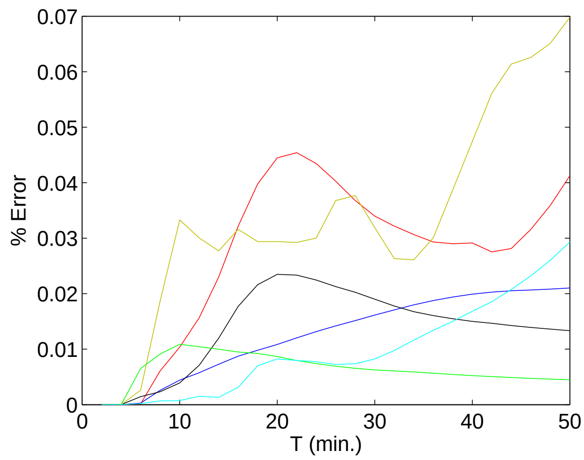

(c)

Figure 4.3: Concentration variance $\Sigma_\rho(t, t_0)$ (a), $\log(\Sigma_\rho(t, t_0) - A_1)$ (b), and relative error (c) plotted versus integration time T for the 6 mixing boxes with trajectories seeded at $t_0 = 400$ min. Other initial times give similar decay structure but different quantitative details.

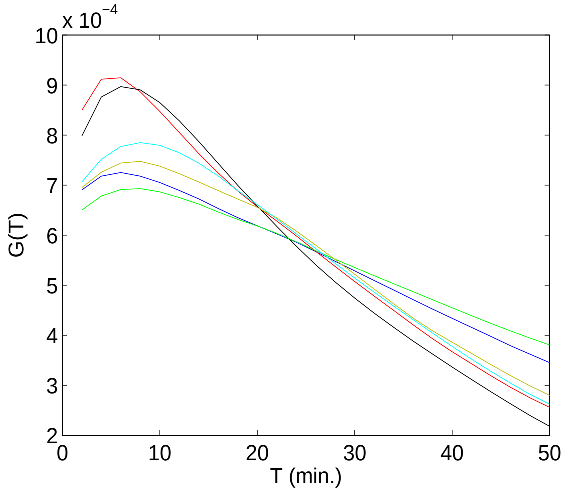

(a)

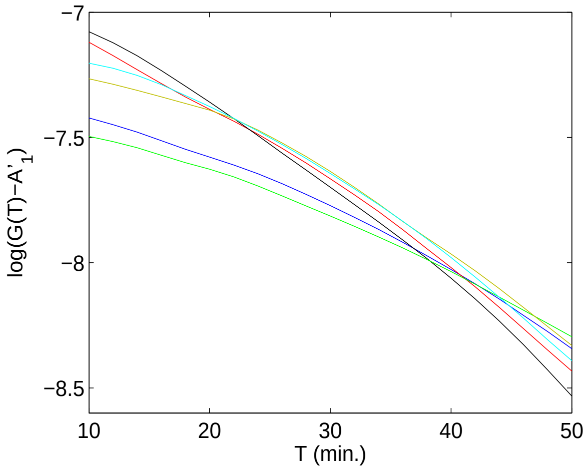

(b)

Figure 4.4: FTLE distrbution function $G(t, t_0)$ (a), and $\log(G(t, t_0) - A1')$ plotted versus integration time T for the 6 mixing boxes with trajectories seeded at $t_0 = 400$ min. Other initial times give similar decay structure but different quantitative details.

to capture advective mixing properties, integration time must be chosen short enough so that diffusion is not dominant. Diffusion dominates advection over long integration times, as manifolds lengthen and become indistinguishable (Fig. 4.7). In addition, the strong time dependence of the velocity field causes the wrapping of manifolds into a tangle, which makes the identification of contigous manifold segments more difficult (Fig. 4.7), and requires a more dense trajetory seeding. Thus a longer integration time imposes computational limitations by requiring more (and longer) trajectory computations.

Dominant flow features such as inflow, outflow and updraft jets govern much of the trajectory movement. High separation often occurs when nearby trajectories split and one enters a jet. LCS's that are strongly hyperbolic cannot exist near a dominant jet, making shearing LCS's vital for characterizing mixing. Fast trajectory flights enable shearing LCS's to be resolved more quickly than hyperbolic LCS's, promoting a shorter integration time.

4.7 Eye-eyewall interaction

An Eulerian eye-eyewall boundary at low z-levels may be defined as the spatial location that separates the strong upward motion of the eyewall from the weak vertical motion of the eye, e.g. a representative contour of the vertical velocity field, however the strong variation of the velocity field in space and time make such a structure discontinuous in time. From a Lagrangian point of view, the eye-eyewall boundary at low z-levels can naturally be defined as the place where there is greatest separation of trajectories, with neighboring trajectories residing in the slow velocity region of the eye and the fast velocity region of the eyewall. This boundary is revealed as a distinguished LCS in the backward FTLE field that persists over all initial times and for integration times of 20 min. and above, see Figures 4.8,4.9 (the LCS is marked in Figure 4.9(b)).

The LCS aligns upward from the sea-surface at about r=15 km and extends vertically to a height of about 4 km, with nearly the same slope radially outwards for all initial times. It is aligned horizontally and located slightly above the sea-surface for $r > 15$ km. Since this LCS appears as a ridge of the backward time FTLE fields, it is attracting. Although it is found from only a 20 minutes integration time, it is invariant for much longer times, and persists over the complete period of analysis of the quasi-steady state intensity. In Figure 4.8(a) and (b), the positions of trajectories seeded on a uniform grid at 400 minutes are displayed after 20 and 60 minutes, superimposed on the backward FTLE fields at initial

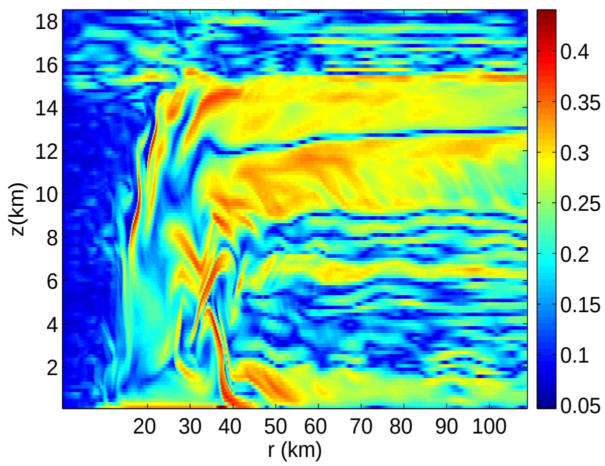

(a)

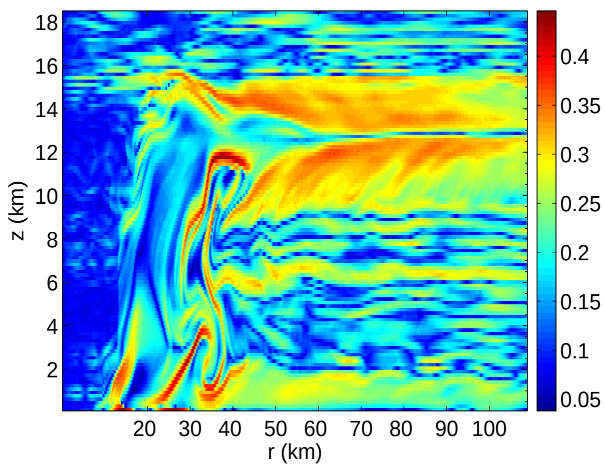

(b)

Figure 4.5: Forward (a) and backward (b) time FTLE fields integrated 20 minutes with an initial time of 400 minutes.

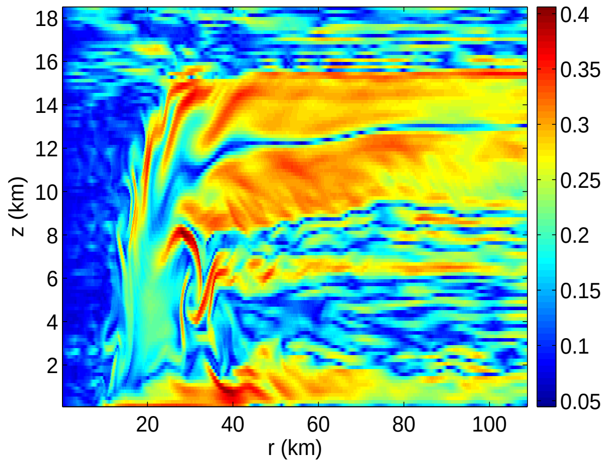

(a)

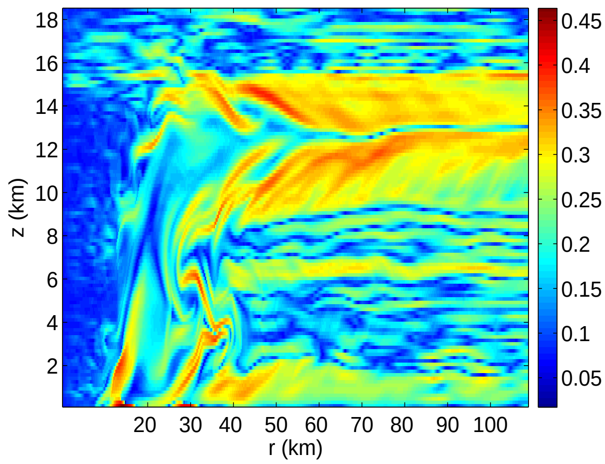

(b)

Figure 4.6: Forward (a) and backward (b) time FTLE fields integrated 20 minutes with an initial time of 420 minutes.

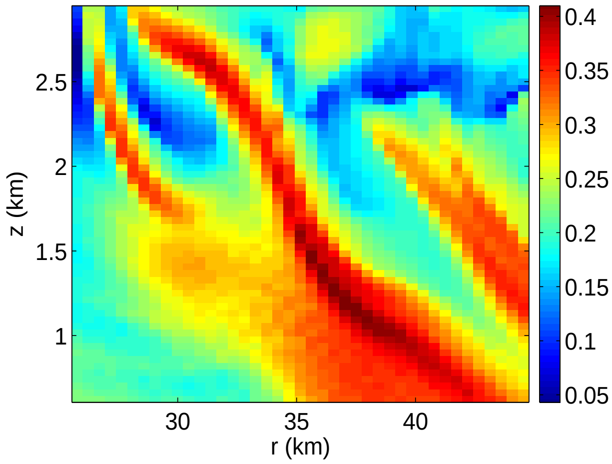

(a)

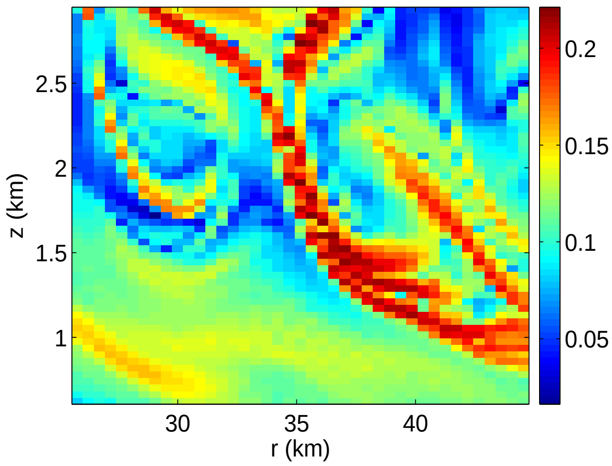

(b)

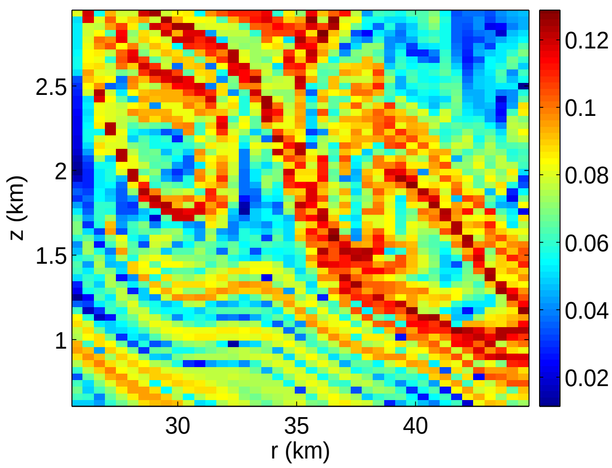

(c)

Figure 4.7: Ridge of forward time FTLE field at initial time of 400 minutes integrated 20 (a), 60 (b), and 120 (c) minutes

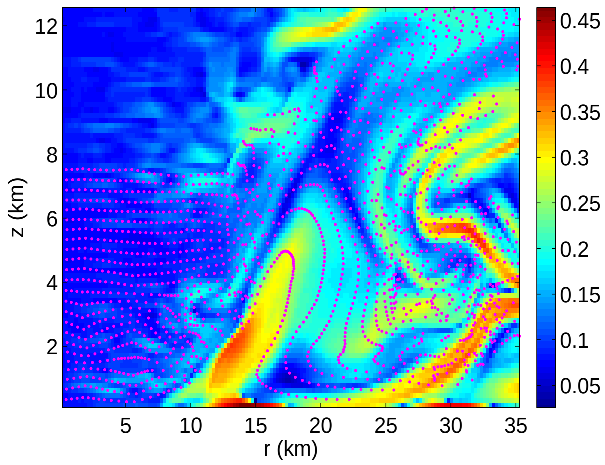

(a)

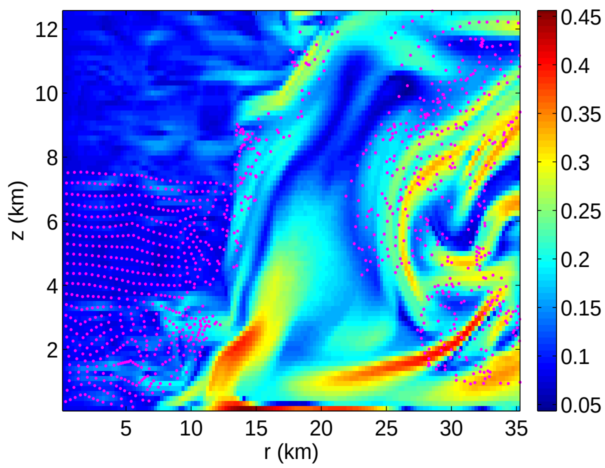

(b)

Figure 4.8: Backward time FTLE field integrated $T = -20$ min. for initial times of 420 minutes (a) and 460 minutes (b). The red dots mark the positions at time $t = t_0$ of trajectories seeded on a uniform grid at 400 min.

times of $t_0 = 420$ and 460 minutes, respectively. The figures show that trajectories in the eye have little movement relative to the LCS, while updraft trajectories show strong movement transverse to the LCS. This transverse motion makes the ridge Lagrangian with nearby trajectories quickly leaving it.

In Figure 4.9 we show both the forward and backward FTLE fields at $t_0 = 400$ minutes, with the 1 m/s Eulerian vertical wind contour superimposed, which may be considered as an Eulerian eye-eyewall boundary. At this time the wind contour is aligned along the LCS; at other times (not shown) it is aligned across the LCS. Seeding trajectories along the LCS (not shown) reveals that trajectories travel transverse to the LCS without crossing, but may cross the Eulerian wind contour.

4.8 Steady state approximations

The velocity fields reside in a quasi-steady state for a period of several hours, between about 400-800 minutes. During this time period of 400 minutes the maximum tangential winds remain in a range of 75 to 88 m/s, where they oscillate rapidly, but in an aperiodic nature. Aside from the differences in intensity, the velocity fields show structural differences in the periods of high maximum tangential winds and lower maximum tangential winds.

The model gives strong time dependent velocity fields, even in a relatively steady state of intensity, leading to different structures for different initial times. The presence of a secondary convective region outside of the main updraft changes the structures associated with the updraft, and is important for changes in the eyewall near-core flux.

In atmospheric studies, Eulerian velocity fields are often used to approximate time-dependent flows, [DMW09]. The idea is that Eulerian markers, such as instantaneous stagnation points, may indicate dynamical structures such as hyperbolic trajectories. Although the time-dependence of this model is too high to infer Lagrangian behavior from Eulerian stagnation points, we make Eulerian approximations associated with high and low wind speeds, and relate them to short-time effects. We compute two composite-averaged velocity fields from the quasi-steady state period, refered to as strong and weak composites (Fig. 4.10), which are representative of the phases with strong and weak maximum tangential winds, respectively. The strong (weak) composite is computed by averaging over the instantaneous velocity fields that generate maximum tangential winds at the highest 20% (lowest 20%) of maximum tangential winds over the time interval of 400-800 minutes.

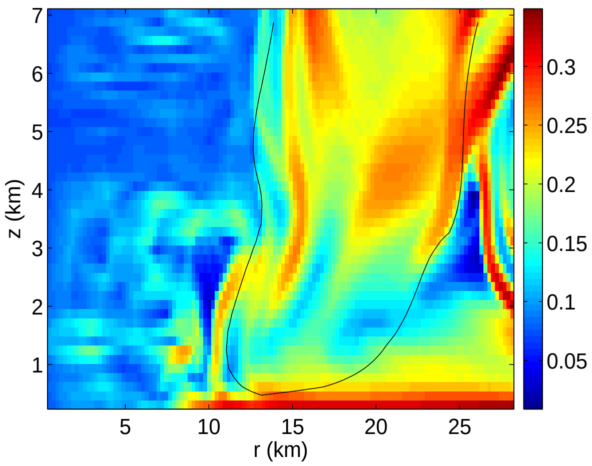

(a)

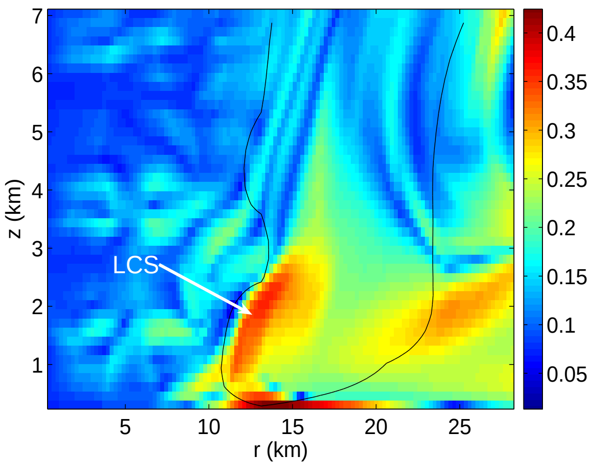

(b)

Figure 4.9: Forward (a) and backward (b) time FTLE fields at $t_0 = 400$ minutes with 1 m/s vertical wind contour. The persistent LCS is marked in (b).

The vertical component of the strong composite shows a single strong updraft, while the vertical wind field of the weak composite shows a dual updraft structure, but with weaker updraft velocities. The radial velocity fields show a more defined outflow jet for the strong composite.

The composite fields can be considered as autonomous velocity fields. The forward and backward FTLE fields for an autonomous velocity field correspond to finite-time, and thus shorter in length, versions of the unstable and stable manifolds of hyperbolic fixed points. Since the velocity field maintains high or low velocities for only a few minutes, invariant structures can only be resolved over a similarly short integration time. Short time structures of the autonomous velocity field can be viewed as markers for finite-time coherent structures of the full velocity fields. The manifolds of the composite velocity fields yield very different structures, not only in the size of the FTLE values, but also in the location and orientation. The outflow jet takes a straighter path in the strong composite FTLE field. At the boundary layer, the weak composite FTLE field shows high values where the boundary layer inflow meets the eyewall updraft, allowing fewer trajectories to enter the eyewall. The secondary updraft at 35 km takes some of the boundary layer trajectories through a region with several LCS's in the forward and backward FTLE fields of both composite fields (Fig 4.11), and moves them upward into the region just outside of the eyewall, before a downdraft takes them inward to the eyewall updraft. Mixing rates for the composite fields (Tables 4.1-4.4) provide a comparison of the mixing in our six initial seed boxes, and for weak and strong maximum tangential winds. All of the mixing rates are generally higher for the strong composite field, for both forward and backward integrations, showing that higher intensity coincides with greater mixing. The FMR and MMR are comparable and are generally of the same order, with the FMR showing higher values in more regions. The FRD and RD are comparable, with the FRD giving higher values in the boundary-layer inflow region due to the presence of a series of LCS's that cause trajectories to be transported into the eyewall updraft, or recirculation within an eddy that forms during low velocity times in the near-core region.

The eye has little trajectory movement, and therefore little relative separation, yielding low mixing rates for all measures. The updraft jet has little separation even with long trajectory flights over short time intervals, and also gives low mixing rates. The highest mixing rates occur at the boundary-layer inflow, where separation from the sea surface

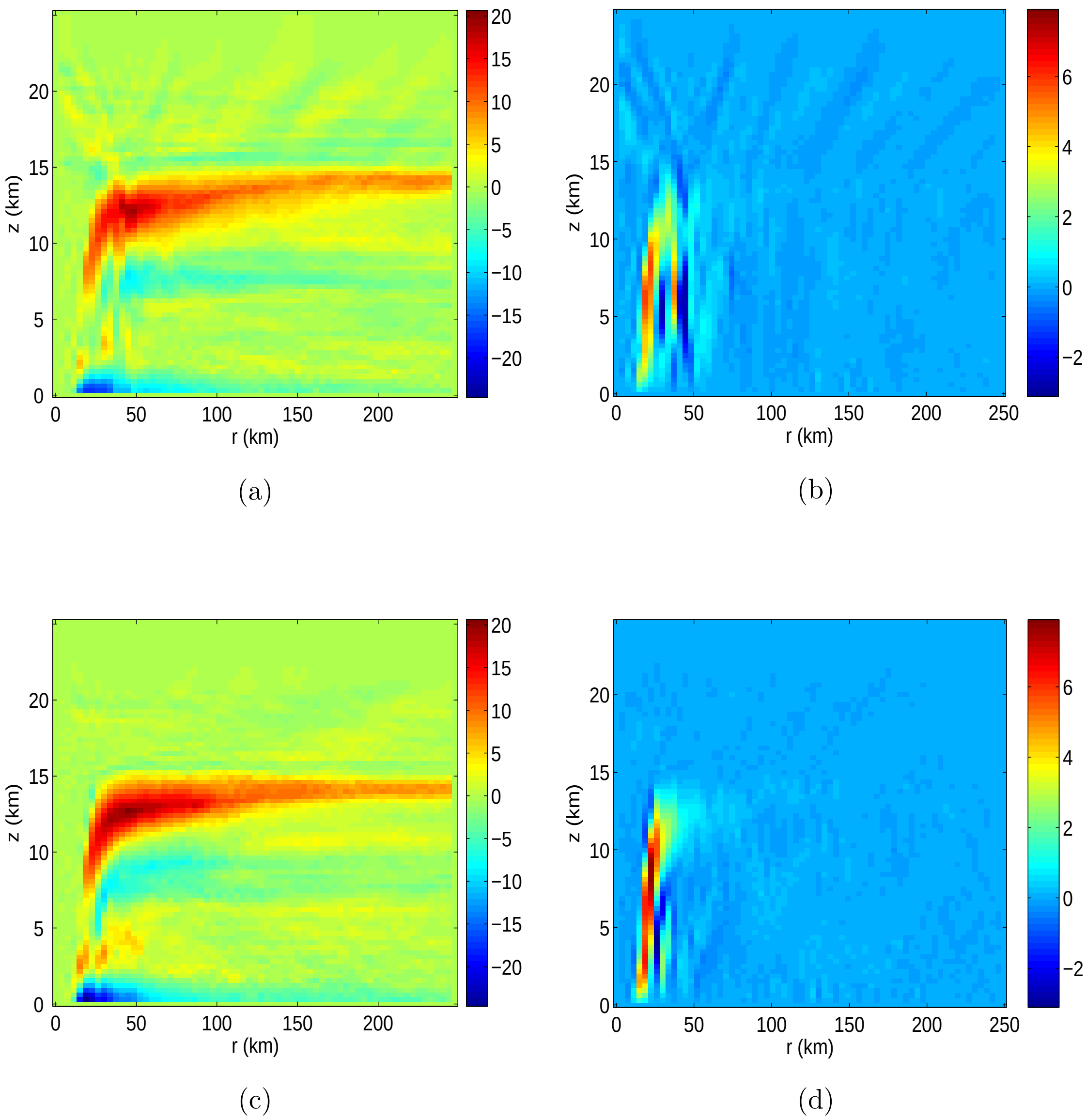

Figure 4.10: Weak composite radial (a) and vertical (b) velocity fields, and strong composite radial (c) and vertical (d) velocity fields.

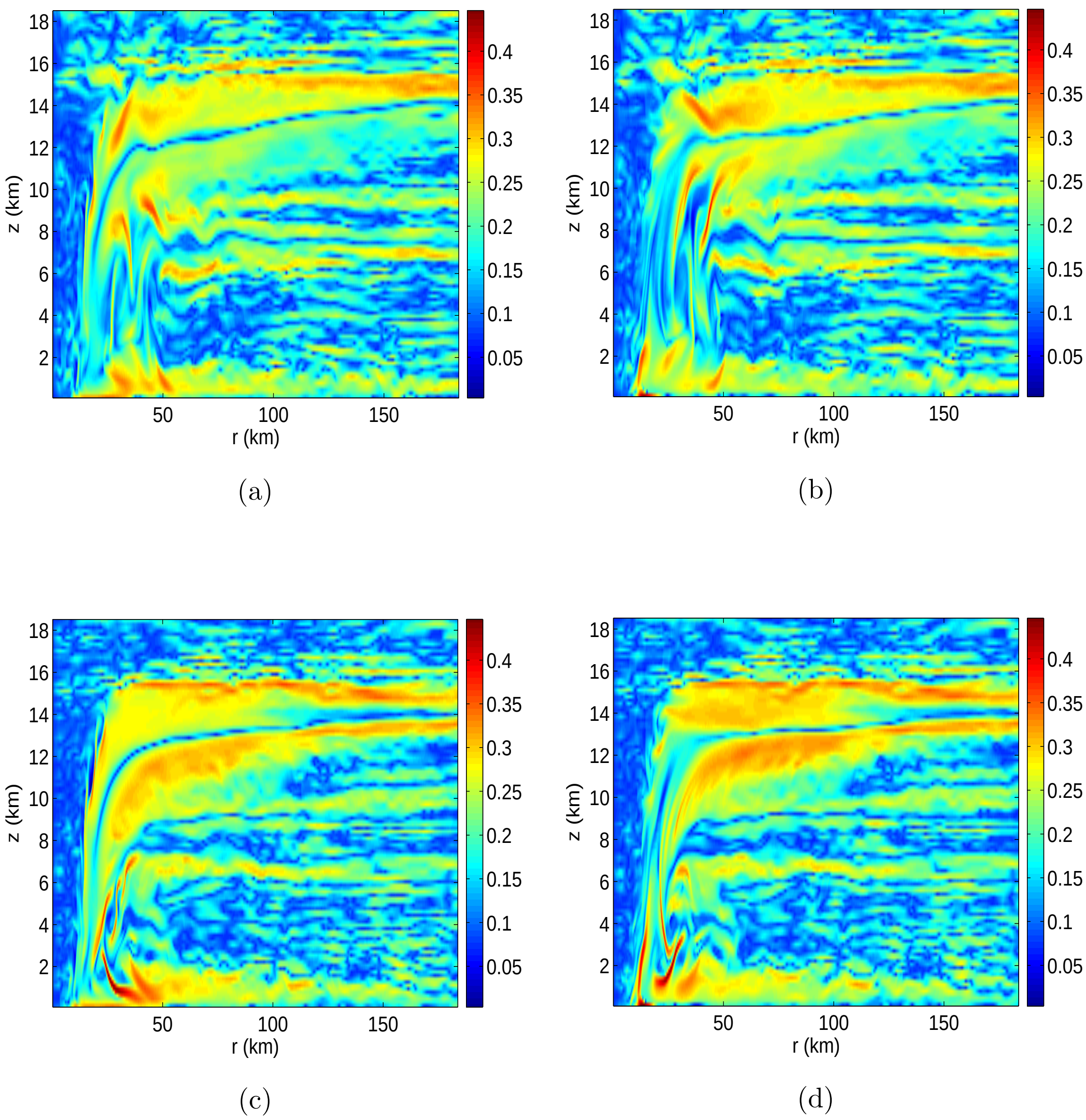

Figure 4.11: Weak composite forward (a) and backward (b) FTLE fields, and strong composite forward (c) and backward (d) FTLE fields, integrated for 20 minutes.

and transport of some trajectories into the updraft give a high separation of trajectories. The near-core has hyperbolic characteristics as a transition between a single eyewall and a secondary region of convection occurs, but higher mixing rates are not indicative of higher eyewall velocities, but of more hyperbolic mixing characteristics in this region.

Table 4.1: Mixing rates of strong composite velocity field for six initial boxes with 20 minutes forward integration time. For each region the mixing rates are MMR (top left), FMR (top right), RD (bottom left), and FRD (bottom right).

.0878	.0267	.0479	.0200	.0641	.0884
.0369	.1655	.0609	.1700	.2284	.0097
eye		updraft		near-core	
.0488	.0224	.0638	.1288	.0878	1.147
.0264	.1683	.0811	.1852	.2183	.5303
low-level eye		updraft		BL inflow	

Table 4.2: Mixing rates of strong composite velocity field for six initial boxes with 20 minutes backward integration time. For each region the mixing rates are MMR (top left), FMR (top right), RD (bottom left), and FRD (bottom right).

.0460	.0175	.0519	.0279	.0629	.0930
.0294	.1692	.0509	.1750	.1380	.2621
eye		updraft		near-core	
.0553	.0400	.0718	.1567	.0770	.6421
.0181	.1666	.0482	.1833	.1849	.2837
low-level eye		lower eyewall		BL inflow	

4.9 Time series analysis

The dependence of the mixing rates on the initial time gives time series that can be analyzed to establish correlations between different quantities. The MMR, FMR and RD were all computed for different integration times for the sequence of initial times.

For a quasi steady-state hurricane, the connection between intensity and mixing rates

Table 4.3: Mixing rates of weak composite velocity field for six initial boxes with 20 minutes forward integration time. For each region the mixing rates are MMR (top left), FMR (top right), RD (bottom left), and FRD (bottom right).

.0286	.0184	.0274	.0103	.0381	.3446
.0322	.1368	.0466	.1452	.0841	.3084
eye		updraft		near-core	
.0281	.0135	.1361	.1288	.0574	16.33
.0209	.1406	.0625	.1996	.1277	2.929
low-level eye		updraft		BL inflow	

Table 4.4: Mixing rates of weak composite velocity field for six initial boxes with 20 minutes backward integration time. For each region the mixing rates are MMR (top left), FMR (top right), RD (bottom left), and FRD (bottom right).

.0262	.0089	.0307	.0201	.0360	.3275
.0265	.1435	.0517	.1589	.0945	.4513
eye		updraft		near-core	
.0329	.0359	.1361	.1288	.0499	2.295
.0113	.1367	.0625	.1996	.1080	.8242
low-level eye		updraft		BL inflow	

is not obvious, especially when the rates are determined by an integration time that lasts longer than a complete period from high to low maximum winds, where the mixing rate value is assigned to the initial time of integration.

The FMR is fit to an exponential decay function, but the curve of the FTLE distribution function does not show a decay for $t-t_0 \leq 10$ minutes, Figure 4.4 (a). After 10 minutes, the FMR can be computed by fitting an exponential decay curve to the remaining data, Figure 4.4 (b). The optimal integration time varies for each box, and for initial times. The mixing functions best fit exponential functions at integration times between 20 and 80 minutes, see Fig. 4.3(c) for the error made in the best fit of the MMR.

In [VTSG03], the MMR has been compared to the FTLE mixing rates for closed domains in time periodic velocity fields, with the FTLE rate being measured at 10 times higher than the measured mixing rate. By allowing initial trajectories to be dispersed into the domain without exiting the domain, the FMR and MMR can be considered as short-time versions of mixing rates within a closed domain. For short time intervals, different initial conditions can lead to significant differences in the mixing rates, as neighboring boxes can show mixing rates differing by a factor of 10. However, rates in the same box are mostly within a factor of 2, and the FMR is not always higher. The differences in the variations of the mixing rates found by [VTSG03] and in our study are likely due to our restriction on integration time and due to the nonclosedness of our domain. The relative dispersion is similar to the FTLE's for an initial box in that it tracks the cumulative separation of trajectories over an integration time. The RD, Figure 4.12 (a), and FRD, Figure 4.12 (b) are fit to both a power law (12) and exponential (13) for integration times of 20 minutes to 120 minutes. For integration times of 20 minutes to 40 minutes, the RMS displacement, in km, most closely fits the power law, as a portion of the initial set is advected into the updraft, while other trajectories become temporarily entrained within finite time hyperbolic manifolds that are in the near-core above the inflow. These trajectories soon mix into the updraft, and the dispersion fits an exponential function more closely at integration times above 40 minutes. The reason for the change between the power law and the exponential regime at 40 minutes is likely that the trajectories in the updraft have reached the upper level outflow jet at this time period.

The differences in mixing rates across different boxes for a variety of integration times indicate that the initial boxes do divide the domain into dynamically distinct regions with different mixing properties. In particular, the eye has relatively small trajectory movements compared to the other regions, and all mixing rates are lower in this region. The time dependent mixing rates can be tested for corrrelation against each of the extrema of the u, v, and w winds. All of the mixing rates give higher values when there is higher averaged trajectory separation over a time interval of integration, but the winds are given instantaneously. High particle velocities and velocity gradients at an initial time would indicate high initial separation, but may not correlate to high Lagrangian rates assigned to the same initial time. The structural differences in the strong and weak composite FTLE fields (Fig. 4.11) indicate that different mixing properties and different structures in the wind fields may coincide with differences in intensity. Correlations of mixing rates to a time lag of maximum winds can indicate the existence of structures which precede or be an effect of higher intensity. Lagrangian structures are an effect of the (u, w)-velocity field from previous

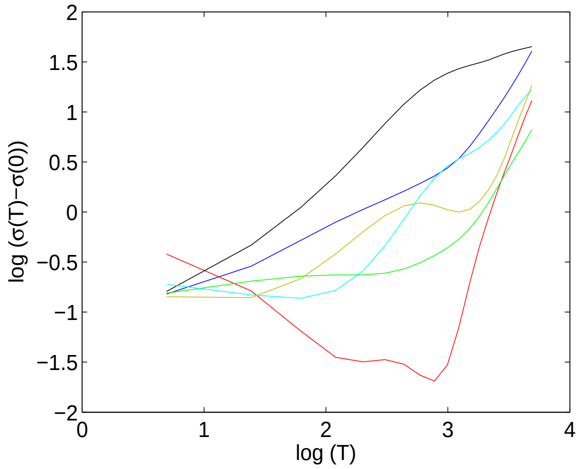

(a)

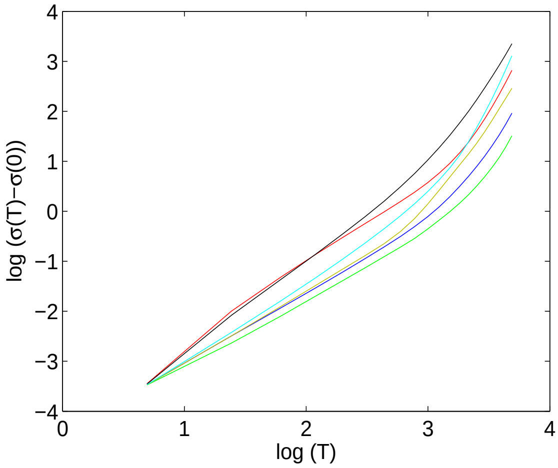

(b)

Figure 4.12: Log-log plots of the RMS displacement versus integration time T for RD (a), and FRD (b).

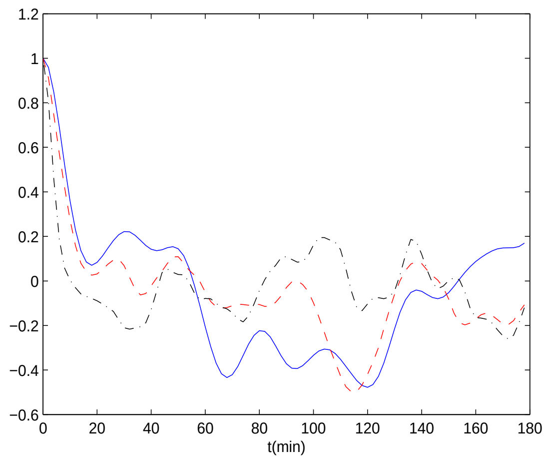

Figure 4.13: Autocorrelations of maximal tangential winds (blue), maximal outflow winds (red), and maximal updraft winds (black).

times in a backward time integration, or future times in a forward time integration. High or low instantaneous winds cannot be seen as neccessarily showing the structures that exist from the maximal and minimal averaged autonomous fields, due to the unsteady nature of the velocity fields. The instantaneous winds may be related to the effect of Lagrangian structures appearing over a series of initial times.

Correlation of mixing rates to maximum tangential winds

The maximum tangential winds are taken here as the main indicator of intensity. The azimuthal velocity component is not used for computing trajectories, but is coupled to the radial and vertical velocity component through a system of PDE's. The tangential wind is not periodic, but oscillates between relatively high and relatively low values.

Autocorrelation values of maximal tangential winds for time lags above 6 minutes, computed within the quasi-steady time window, are always below .5 (Fig. 4.13), showing little predictability within the velocity fields during this time window. Correlations of maximal wind values of the separate velocity components to each other are even less than .2.

The correlations of mixing rates to maximum tangential winds (some correlations above .7) is far greater than to the extrema of radial (correlations below .5) or vertical (correlations below .4) winds.

The oscillations of the maximum tangential winds occur over time intervals of between 20 and 40 minutes. A 40 minutes integration time is below the period of two oscillations, and is the maximum integration time that yields significant correlation of mixing rates to maximum tangential winds. The rates converge to an exponential or power law after a short time interval, and begin to show correlation after an integration time of 10 minutes. The best fit to the power law for relative dispersion occurs for integration times of 18 to 40 minutes, long enough to resolve structures but less than the period of 2 oscillations.

The mixing rates are functions of initial time for each of the six boxes. The different initial boxes give very different mixing rates, with higher mixing rates occuring in the boxes that have the highest velocities. The boundary layer inflow and eyewall updraft boxes show the highest correlations to maximum tangential winds (Figs. 4.14,4.15), for both forward and backward integration time.

Trajectories can be integrated forward or backward in time, giving Lagrangian fields (i.e. MMR, FMR, RD, FRD) that show attracting structures (forward integration), or repelling structures (backward integration). For correlating a Lagrangian quantity to intensity, the forward time integration gives Lagrangian fields that result from future velocities, while backward time integration gives fields that result from past velocities. The wind field at an initial time is predicted by the backward time field at that time, and predicts the forward time field at that initial time. Backward time integration showed higher correlation with the wind fields than forward time integration for most boxes with high correlation.

Correlating the Lagrangian fields to a time lag (Lagrangian fields trailing velocities) or lead (velocities trailing Lagrangian fields) of the velocity field shows how the Lagrangian structures and maximum winds are predictive of each other (Figs. 4.14,4.15). Predicting hurricane intensity (on admittedly very short time scales) by mixing rates can be accomplished by showing a correlation between a backward time integration lag, since a function of previous information would correlate to future information.

RD and FRD show similar high correlation to maximum tangential winds, suggesting that both quantities are similar for predictability. The correlation for both measures is higher for a backward time integration and for the Lagrangian field lagged against the maximum wind, which suggests that the Lagrangian measures are predictive of the maximum winds. Higher separation and mixing rates backward in time from the eyewall updraft are caused from a larger source of material that enters the updraft forward in time. The structures that are repelling backward in time are attracting forward in time, thus the higher mixing rates are likely also due to the presence of a stronger updraft jet. The autonomous field from the highest averaged velocities shows a very strong updraft jet, while the low velocities show a weaker updraft jet that is not as efficient in advecting all entering trajectories into the outflow.

Though RD and the FRD produce similar correlations to maximal tangential winds, especially for backward time integrations from the eyewall updraft, the RD gives slightly stronger results. This shows that total separation is important, and using the separation in the direction of maximal exapnsion does not give any additional advantage. Though the relative dispersion has higher correlation to maximal winds, the FTLE fields still have the advantage of studying the entrainment of trajectories, and viewing LCS's. Both measures show a higher correlation at 20 minutes and the correlation begins to diminish at an integration time of 40 minutes. The RD is useful for both forward and backward time integration (Figs. 4.14,4.16), while the FRD is useful only for backward time integration (Figs. 4.14,4.15). The MMR does not show correlation as high as the other rates, but shows some correlation for the shortest integration time of 20 minutes (Fig. 4.15). The MMR is dependent on the final position of trajectories, and not only on the separation of trajectories. Over longer integration times, this could make the MMR more sensitive to movement caused by gravity waves.

The FRD shows negative correlation of -.6684 to maximal inflow winds for the boundary layer inflow box with a forward time integration of 20 minutes and a 4 minutes time lag, which shows that enhanced mixing is correlated with the enhancement of the BL inflow (a negative of the extreme minimum of the u field). The boundary layer inflow has more hyperbolic mixing characteristics than the other regions, which may make FTLE's better suited as a mixing measure in this region. This is the only region where the FRD shows higher correlation than the RD. The eyewall updraft box also shows negative correlation from FTLE's with a forward time integration.

While higher velocities are generally associated with higher mixing rates, the presence of hyperbolic structures may allow or inhibit transport, which may precede or trail higher intensities. A lead or lag of mixing rates to velocities is then appropriate to capture the hyperbolic effects. In many cases, the correlation improved when the Lagrangian rates were lagged against the maximum winds. The Lagrangian structures are then predictive of maximum tangential winds. Correlation of 0.6 or higher is present for a lag of up to 10 minutes, which is about half of a period of oscillation of the maximum tangential winds.

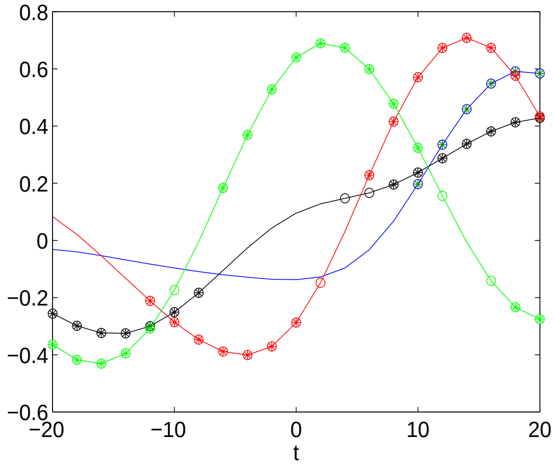

(a)

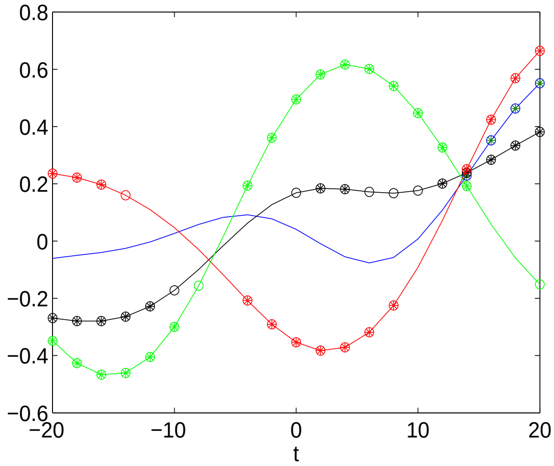

(b)

Figure 4.14: Correlations of mixing rates for the BL inflow box lagged by t to maximal tangential winds with (a) 20 min. and (b) 30 min. integration time for FMR (red), FRD (black), MMR (blue), and RD (green). Filled circles indicate correlation above a 99% confidence threshold, while open circles indicate correlations above 95% but below 99% confidence.

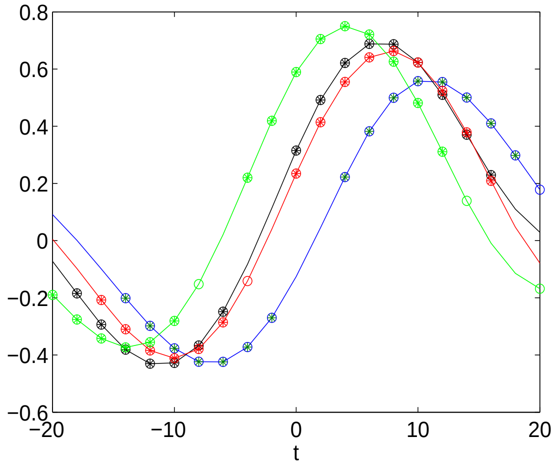

(a)

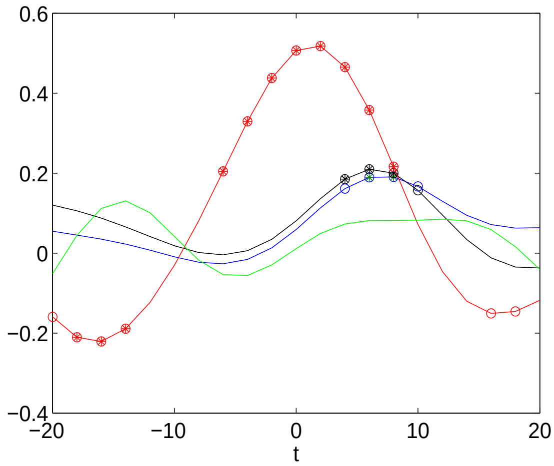

(b)

Figure 4.15: Correlations of mixing rates for the BL inflow box (a) and eyewall updraft box (b) lagged by t to maximal tangential winds with 20 min. backward integration time for FMR (red), FRD (black), MMR (blue), and RD (green). Filled circles indicate correlation above a 99% confidence threshold, while open circles indicate correlations above 95% but below 99% confidence.

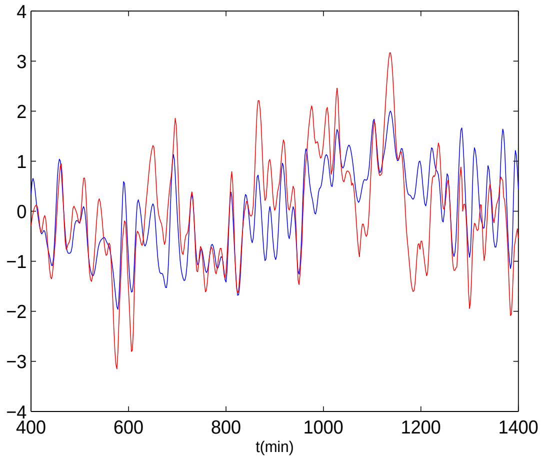

(a)

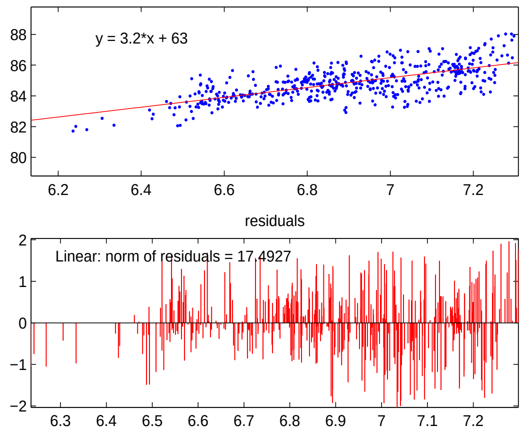

(b)

Figure 4.16: (a) Normalized relative dispersion for 20 minutes backward integration (blue), and maximum tangential winds delayed 4 minutes (red). (b) Relative dispersion for 20 minutes backward integration time against maximum tangential winds, with linear best fit and norm of residuals.

The highest correlations occur for 2 to 6 minutes lags, which means that the initial time of integration for the Lagrangian fields is at a time where the maximum tangential winds are increasing, but before the local maximum occurs.

4.10 Concluding remarks

Lagrangian mixing for the complex velocity fields of the axisymmetric hurricane model of [RE87] has been studied. The inner core region was shown to have Lagrangian structures that vary over time, and play a prominent role for mixing in the region, which is related to hurricane intensity. We have produced mixing rates that correlate to maximum winds, and can be used for a short time prediction of the maximum winds. The mixing rates computed in our study are an extension of mixing rates of [AJFOGL96] and [HMG01] established for closed regions or time-periodic velocity fields. In particular, our rates depend on initial time, integration time, time lag, and two spatial coordinates. Various measures of maximal Eularian intensity have been extracted from the u, w, and v wind fields, and compared to the time-dependent mixing rates. A correlation analysis showed that the rates have highest correlation to the maximum tangential winds. The conclusions drawn are that episodes of enhanced mixing between the low-level eye and eyewall preceed short-time enhancements of intensity, and thus favor the interpretation that new local generation of buoyancy at the eyewall lead to enhanced thermodynamic cycling of the hurricane heat engine. In principle, the mixing could have been responsive of short-term fluctuations of intensity in response to enhanced flow gradients, or mixing could have directly spun down tangential winds through angular momentum mixing, but since mixing precedes such episodes, neither of these explanations can be favored by the present results. Further work will use a canonical correlation analysis to find correlations between the mixing rates as well as the maximal winds. The methods presented here will also be extended to a three-dimensional hurricane model.

Chapter 5

Advective mixing in a nondivergent barotropic hurricane model

5.1 Summary

This chapter studies Lagrangian mixing in a two-dimensional barotropic model for hurricane-like vortices. Since such flows show high shearing in the radial direction, particle separation across shear-lines is diagnosed through a Lagrangian field, referred to as R-field, that measures trajectory separation orthogonal to the Lagrangian velocity. The shear-lines are identified with the level-contours of another Lagrangian field, referred to as S-field, that measures the average shear-strength along a trajectory. Other fields used for model diagnostics are the Lagrangian field of finite-time Lyapunov exponents (FTLE-field), the Eulerian Q-field, and the angular velocity field. Because of the high shearing, the FTLE-field is not a suitable indicator for advective mixing, and in particular does not exhibit ridges marking the location of finite-time stable and unstable manifolds. The FTLE-field is similar in structure to the radial derivative of the angular velocity. In contrast, persisting ridges and valleys can be clearly recognized in the R-field, and their propagation speed indicates that transport across shear-lines is caused by Rossby waves. A radial mixing rate derived from the R-field gives a time-dependent measure of flux across the shear-lines. On the other hand, a measured mixing rate across the shear-lines, which counts trajectory crossings, confirms the results from the R-field mixing rate, and shows high mixing in the eyewall region after the formation of a polygonal eyewall, which continues until the vortex breaks down. The location of the R-field ridges elucidates the role of radial mixing for the interaction and

breakdown of the mesovortices shown by the model.

5.2 Background and overview

Several recent studies [FR99, FR01, MBAB06, HS09] are devoted to the mixing of fluid from different regions of a hurricane, which is considered as a fundamental mechanism that is intimately related to hurricane intensity. A complete understanding of these mixing processes, in particular the eye-eyewall mixing [CPMB07, MBAB06, Wil01], is expected to significantly enhance our understanding of the physical mechanisms sustaining the hurricane. Since mixing is based on particle motion, the Lagrangian frame of reference provides the most natural framework in which it can be diagnosed. Much progress has been made in recent years in the study of Lagrangian mixing in two-dimensional incompressible flows [HP97, HY00, Hal01b, SH08, Hal02, SLM05], resulting in a number of different, though related diagnostics, most of which are based on concepts from dynamical systems theory. For applications of Lagrangian techniques to atmospheric models, see [JL01] and [HMG01].

Much insight into specific aspects of mixing in hurricanes can be gained from the study of simplified two-dimensional models. Basically there are two classes of such models: Axisymmetric models, most notably the model of [RE87], and planar models such as the model of [KS01] and [SMT$^+$99]. In this chapter we apply Lagrangian techniques to analyze mixing in the planar, nondivergent barotropic model of [KS01]. Our analysis confirms a study of [KE01] which illustrates that significant eye-eyewall mixing occurs during polygonal eyewall transitions. Lagrangian mixing in the axisymmetric model introduced in [RE87] is investigated in Chapter 4. For another discussion of axisymmetric mixing, see [WD06].

The model studied in this chapter provides a two-dimensional representation of a hurricane that initiates with an annular ring of enhanced vorticity, and then undergoes a vortex breakdown resulting in a monopolar end state. During the breakdown, a polygonal eyewall occurs, which forms four elliptical pools of high vorticity. Mixing of potential vorticity, which in this model is proportional to relative vorticity, can be visualized using Eulerian diagnostic measures of instantaneous particle separation. A commonly used Eulerian diagnostic is the so called Q-field, derived from the Jacobian of the Eulerian velocity field. According to the Okubo-Weiss criterion [SMT$^+$99], positive values of this field indicate instantaneous particle separation, whereas negative values indicate contraction. For our model, the Q field shows that regions of high relative vorticity gradient are also places where high trajectory separation and mixing occurs.

While Eulerian measures of mixing can only diagnose instantaneous particle separation, Lagrangian techniques utilize a moving frame approach along trajectories and compute measures for the average separation over a finite integration time. This approach is particularly useful in time-dependent velocity fields, where trajectories may cross Eulerian streamlines [DMW09]. Much of the recent work in Lagrangian mixing has extended the ideas of hyperbolicity for steady flows to time dependent velocity fields [Hal01a, HP97, HY00, Hal00, MW98], generalizing the concept of stable and unstable manifolds of an equilibrium to the stable and unstable manifolds of a hyperbolic trajectory. These manifolds are referred to as Lagrangian coherent structures (LCS's). Even in two-dimensional flows, time-dependence can give rise to multiple intersections of these manifolds, leading to a partition of the flow into invariant regions (lobes), and to mixing through the lobe dynamics [MW98, CW00].

Efficient visualization of LCS's is accomplished through the construction of Lagrangian scalar fields, which measure separation of nearby trajectories. Current Lagrangian methods utilize a variety of fields, including finite-time Lyapunov exponents [HP97, HY00, Hal00, Hal04], finite-size Lyapunov exponents [KL02, GRH07], and relative dispersion [HMG01]. Each of these methods defines a scalar field and the LCS's as maximal ridges of that field.

To study Lagrangian mixing in our model, we compute particle trajectories from the numerically calculated, time-varying velocity field. The Lagrangian diagnostic fields are functions of the initial time and position at which the trajectories are seeded. A comparison of these fields with the Okubo-Weiss criterion indicates that high particle separation predicted from the Q-field typically does not coincide with Lagrangian hyperbolic structures, however the Lagrangian Q-field, formed by integrating Q-values along particle trajectories, shows a greater relation to other Lagrangian fields.

An important feature of the particle trajectories calculated from our model is that they show an almost circular motion, combined with high shearing in the radial direction. The problem caused by this high shear is that trajectory separation and mixing occur without the entrainment of trajectories, as the mixing is largely diffusive. A key question that we aim to answer is whether coherent structures that play a role in the systematic transport of trajectories can persist through high shear.

Distinct regions of trajectories with similar properties become more difficult to distinguish through the use of scalar fields which measure only distance, such as the field of finite-time Lyapunov exponents (FTLE-field). In fact, the FTLE-field computed from our model does not show distinguished ridges characteristic of hyperbolic mixing. Instead, the structure of the FTLE-field is very similar to the structure of the radial derivative of the angular velocity, indicating that the FTLE-field is dominated by the shear and not by hyperbolic mixing.

In order to separate shear from hyperbolic mixing we follow the approach used in [HI03], and decompose the separation of trajectories in the directions along and normal to the Lagrangian velocity. This approach allows us to identify two Lagrangian fields: The R-field, which is a diagnostic for hyperbolic mixing normal to the Lagrangian velocity, and the S-field, which is a measure of shearing, and is used to define shear-lines by its level-contours. In contrast to the FTLE-field, the R-field shows distinct ridges and valleys observable as coherent structures. The evolution of these structures provides a mechanism for mixing through the eyewall, and their speed indicates that this mixing is caused by Rossby waves. The structures are particularly distinct after polygonal eyewall formation, and they persist until the vortex breaks down, in regions where the Okubo-Weiss criterion predicts pools of high separation associated with the formation of pools of high vorticity.

We note that another approach to diagnosing mixing in the presence of shear is based on subtracting a mean shear from the flow. This approach was introduced by [AM78] using a generalized Lagrangian mean for nonlinear waves, and was subsequently developed further and refined to a modified Lagrangian mean to quantify and distinguish stirring from irreversible mixing, see [McI80] and [Dun80].

The time-dependence of our velocity field leads to time-dependent shear-lines, and regions of high orthogonal (hyperbolic) separation lead to sets of trajectories that are mixed through the shear-lines. We quantify this mixing by introducing measured (via trajectory counting) and predicted (from the R-field) mixing rates. In addition, we study radial mixing rates defined by angular averages of the FTLE-field, the S-field, and the R-field. The mixing rates defined through the former two fields are characteristic of shearing and give spuriously a false sense of mixing during the initial phase of the model, where "true mixing" occurs after the polygonal eyewall formation.

In previous work on the same model, [HS09] have applied the Lagrangian-Eulerian hybrid method of effective diffusion [Nak96, SH03]. Here diffusive mixing properties are computed based on the increasing lengths of the vorticity contours, with the computations initialized at the initial time of the model. The resulting mixing rate is a function of an effective radius and the integration time, and shows similar structures as our mixing rates.

Our methods depart from those of [HS09] in that we utilize a moving time window, which attributes mixing to short-time advective events. Rather than determining contour lengths, we study transport across contours of the S-field. The resulting mixing rates are completely determined by the given velocity field, that is, they do not depend on a chosen initial profile of the tracer distribution.

The outline of the chapter is as follows. We begin, in Section 5.3, with an overview of the nondivergent barotropic model, and of the numerical methods used to compute the velocity field and the particle trajectories. In Section 5.4 we introduce the scalar fields utilized for diagnosing mixing and shear: The Eulerian Q-field, the Lagrangian Q-field, the angular velocity field, the Lagrangian FTLE-field, the R-field, and the S-field. The latter two fields are extracted from the transformed variational system introduced in [HI03]. The main results of the chapter are presented in Sections 5.5-5.7. In Section 5.5 we study the behavior of the three Lagrangian fields for a fixed initial time of 6 hours, after a polygonal eyewall has formed, and for different integration times. The ridge, valley, and edge structures observed in the R-field are identified with coherent structures and invariant sets relative to the shearing. In Section 5.6 we fix the integration time to 1 hour and study the diagnostic fields for varying initial times. The structures observed in these fields are related to different mixing processes occurring during the three main phases of the model: crystalization in which polygonal eyewall features form and develop filamentation, vortex interaction and merger which destroy the symmertry, and final collapse into a monopole. Section 5.7 is devoted to the mixing rates mentioned before, which are displayed as functions of initial time and either radius or value of S along a shear-line. Concluding remarks and an outlook on future work are given in Section 5.8.

5.3 Model overview

The model used in this chapter is the 2D nondivergent barotropic model for hurricane-like vortices studied by [KS01, KE01, SMT$^+$99]. The velocity field, $\mathbf{u}(\mathbf{x}, t) = (u(\mathbf{x}, t), v(\mathbf{x}, t))^*$ with $\mathbf{x} = (x, y)^* \in \mathbb{R}^2$ (asteriks denote transposed vectors or matrices), is given as the solution on the f-plane of the incompressible Navier Stokes equation,

$$\frac{\partial \mathbf{u}}{\partial t} + (\mathbf{u} \cdot \nabla)\mathbf{u} - f\mathbf{B}\mathbf{u} + \frac{1}{\rho}\nabla p = \nu \nabla^2 \mathbf{u}, \tag{5.1}$$

$$\nabla \cdot \mathbf{u} = 0, \tag{5.2}$$

where

$$\mathbf{B} = \begin{pmatrix} 0 & 1 \\ -1 & 0 \end{pmatrix},$$

p is the pressure, ρ the constant density, f the constant Coriolis parameter, and ν the constant viscosity, chosen to be $100\,\mathrm{m}^2\,\mathrm{s}^{-1}$. In the choice of ν we follow [SMT$^+$99], while [KS01] used $5\,\mathrm{m}^2\,\mathrm{s}^{-1}$. The choice of viscosity may have an effect on long time mixing processes, which could be studied by the methods of [HS09]. Expressing the velocity in terms of a streamfunction $\psi(\mathbf{x}, t)$ as $\mathbf{u} = -\mathbf{B}\nabla\psi$ and eliminating the pressure from (5.1), leads to the equation

$$\frac{\partial \zeta}{\partial t} + \frac{\partial \psi}{\partial x}\frac{\partial \zeta}{\partial y} - \frac{\partial \psi}{\partial y}\frac{\partial \zeta}{\partial x} = \nu \nabla^2 \zeta, \tag{5.3}$$

where $\zeta = \nabla^2\psi$ is the relative vorticity. Following [KS01], we impose periodic boundary conditions on ψ with a fundamental domain of $600\,\mathrm{km} \times 600\,\mathrm{km}$, and choose as initial condition an almost circular symmetric ring of vorticity, $\zeta_0(r, \theta)$, to model a 2D hurricane after an initial eyewall has formed. The defining equation of $\zeta_0(r, \theta)$ is the equation used in [KS01].

Equation (5.3) was solved numerically using a Fourier pseudospectral method with 512×512 collocation points. Dealiasing results in 170×170 Fourier modes. The ODE-system for the Fourier modes was solved via Matlab's ode45 routine, which implements a fourth order Runge-Kutta method with adaptive time steps.

In our numerical calculation of ψ and ζ, we reproduced the behavior observed in [SMT$^+$99]. The annular ring of high vorticity fluid develops a wavenumber 4 asymmetry, which is present in the vorticity fields as early as 2 hours, and develops into a polygonal eyewall, with 4 mesovortices after 6 hours. After 8 hours, the mesovortices begin to break down and merge. The breakdown of the mesovortices is nearly complete after 12 hours, and mixing of high and low vorticity occurs along long filament structures. The relative vorticity fields during these times can be seen in Figs. 5.6–5.11 (a). After 24 hours, diffusive mixing along the filaments leads to a more mixed state. Few pools of high or low vorticity fluid remain, with a pool of low-vorticity fluid from the eye migrating through the eyewall, and high vorticity fluid redistributing in the eye. After 48 hours, a high vorticity eye and a low vorticity environment remain in a monopole endstate. The eyewall is no longer present as there is no longer a strong angular velocity gradient.

In this chapter we study Lagrangian mixing in the model, which is based on following trajectories for varying initial times. The trajectories were calculated with the same spatial and temporal resolution as the model output, using a fourth order Runge-Kutta method with a fixed time step of 7.5 s. Because of time and memory limitations associated with the large number of trajectories needed for quantifying mixing over a sequence of initial times, the trajectories used for computing time-dependent mixing rates were calculated with a time step of 60 s. Comparison of the results for the two time steps for a small random set of initial conditions showed that the use of the coarser time resolution in the mixing calculations is justified.

5.4 Diagnostic fields for mixing and shear

In this section we introduce the scalar fields utilized to diagnose the particle flow resulting from the numerically calculated velocity field. A main characteristic feature of the model is an almost circular motion, the trajectories encircle the origin in the counterclockwise direction. The model shows a strong variation of the particle speed $|\mathbf{u}|$ in the radial direction. This variation leads to high shearing that dominates the particle separation, but is not the result of hyperbolic trajectory separation. Superimposed on this shear effect is hyperbolic mixing due to trajectory separation in directions orthogonal to the velocity.

In order to diagnose hyperbolicity, we exploit the Lagrangian field introduced in [HI03], in which hyperbolic trajectory splitting is separated from particle separation due to shearing. The more common FTLE-field is also analyzed, however, this field is dominated by the shear and hence not suitable as an indicator for hyperbolic mixing. In order to quantify hyperbolic mixing, we define closed shear lines as contour lines of a suitably defined shear field, and measure and predict transport across these lines (Section 5.7). Further indicators used in our study are two Eulerian fields: The Hessean determinant of the streamfunction (Q-field), and the radial gradient of the instantaneous angular velocity.

5.4.1 Eulerian fields

Q-field

Eulerian trajectory separation occurs when the linearized velocity shows local expansion of area. The local variation of area can be inferred from the Jacobian of the velocity field, that is, from the Hessian determinant of the streamfunction, which is referred to as the Q-field,

$$Q(\mathbf{x}, t) = \psi_{xy}^2(\mathbf{x}, t) - \psi_{xx}(\mathbf{x}, t)\psi_{yy}(\mathbf{x}, t). \tag{5.4}$$

According to the Okubo-Weiss criterion [SMT$^+$99], regions with $Q > 0$ show local trajectory repulsion, whereas regions with $Q < 0$ show local attraction. The Q-field allows diagnosis of instantaneous separation, which typically differs from Lagrangian measures of separation.

Angular velocity

The strong rotation and near symmetry of the flow suggests that polar coordinates (r, θ) provide a useful coordinate system for displaying fields calculated from the velocity field. In particular, the quasi-circular behavior of trajectories suggests that the angular velocity, $\omega = r^{-1}\mathbf{u} \cdot (-\sin\theta, \cos\theta)^*$, is an approximate measure of the particle speed, and the derivative $\partial\omega/\partial r$ is an approximate measure of shearing.

For any scalar field $\varphi(\mathbf{x}, t)$, a measure for the radial variation is provided by the angular average, indicated by an over-bar,

$$\overline{\varphi}(r, t) = \frac{1}{2\pi}\int_0^{2\pi} \varphi(r, \theta, t)\, d\theta.$$

Contours of $\frac{\partial\omega}{\partial r}$ are shown in Figs. 5.6–5.11 (d-f) showing the relationship of maxima (maximum normal propogating shear), and minima (maximum counter propogating shear) of $\frac{\partial\omega}{\partial r}$ to features of other scalar fields.

5.4.2 Lagrangian fields

Let $\phi_{t_0}^t(\mathbf{x}_0)$ be the flow map associated with the equation

$$\dot{\mathbf{x}} = \mathbf{u}(\mathbf{x}, t) \tag{5.5}$$

for particle trajectories $\mathbf{x}(t)$, that is, the solution of (5.5) with initial condition $\mathbf{x}(t_0) = \mathbf{x}_0$. Small perturbations in the initial condition, $\mathbf{y}_0 = \mathbf{x}_0 + \xi_0$, lead to a perturbed trajectory

$\mathbf{y}(t) = \mathbf{x}(t) + \xi(t)$. For sufficiently small $|\xi_0|$, the perturbation $\xi(t)$ can be approximated through the Jacobian of the flow map as

$$\xi(t) = \nabla\phi_{t_0}^t(\mathbf{x}_0)\xi_0, \tag{5.6}$$

which satisfies the variational equation

$$\dot{\xi} = \nabla\mathbf{u}(\mathbf{x}(t), t)\xi. \tag{5.7}$$

For our velocity field, the particle separation is dominated by the shearing in the radial direction. As a result, the FTLE-values (see Chapter 3.4.1) measure growth of perturbations in approximately angular directions, and high FTLE-values (ridges) occur near extrema of $\partial\omega/\partial r$, whereas low FTLE-values occur near zero contours of $\partial\omega/\partial r$. Generally, FTLE-fields are not suitable as indicators of hyperbolic mixing in the presence of high shear.

Integrated Q-field

In addition to the instantaneous Q-field, equation (5.4), we consider the integrated Q-field, formed by integrating Q along trajectories

$$\widehat{Q}(\mathbf{x}, t) = \int_{t_0}^{t_0+T} Q(\mathbf{x_0}(t), t)dt. \tag{5.8}$$

Lagrangian fields for hyperbolic mixing and shear

Following [HI03], in order to separate mixing and shear in the variational system (5.7), a moving frame of reference is introduced by setting

$$\xi = M(\mathbf{x}(t), t)\eta, \tag{5.9}$$

where the component vectors of the matrix M,

$$M(\mathbf{x}, t) = \frac{1}{|\mathbf{u}(\mathbf{x}, t)|}(\mathbf{u}(\mathbf{x}, t), \mathbf{u}^{\perp}(\mathbf{x}, t)), \;\; \mathbf{u}^{\perp} = (-v, u)^*,$$

are the normalized fluid velocity $\mathbf{u}/|\mathbf{u}|$, and the unit vector orthogonal to $\mathbf{u}$. This transformation is motivated by the fact that for autonomous velocity fields, $\mathbf{u} = \mathbf{u}(\mathbf{x})$, $\mathbf{u}(\mathbf{x}(t))$ is a solution of (5.7). Although our numerically computed fluid velocity is non-autonomous, its time variation is slow, so that $\mathbf{u}(\mathbf{x}(t), t)$ is still close to a solution of (5.7) for finite times. The transformed system for η can be written in the form [HI03],

$$\dot{\eta} = \big[A(t) + b(t)B\big]\eta, \tag{5.10}$$

where

$$A(t) = \begin{pmatrix} -r(\mathbf{x}(t),t) & a(\mathbf{x}(t),t) \\ 0 & r(\mathbf{x}(t),t) \end{pmatrix},$$

$$b(t) = \frac{1}{|\mathbf{u}|^2}\mathbf{u}^{\perp} \cdot \mathbf{u}_t \,|_{\mathbf{x}=\mathbf{x}(t)}\,,$$

$$\begin{aligned} r(\mathbf{x},t) &= \frac{1}{|\mathbf{u}|^2}(\mathbf{u}^{\perp})^*(\nabla\mathbf{u})\mathbf{u}^{\perp} \\ &= \frac{1}{|\mathbf{u}|^2}\big(u^2 v_y - uv(u_y + v_x) + v^2 u_x\big), \end{aligned}$$

and the non-diagonal entry a is composed of two parts,

$$a(\mathbf{x},t) = s(\mathbf{x},t) + d(\mathbf{x},t),$$

where

$$\begin{aligned} s(\mathbf{x},t) &= \frac{1}{|\mathbf{u}|^2}\mathbf{u}^*(\nabla\mathbf{u})\mathbf{u}^{\perp} \\ &= \frac{1}{|\mathbf{u}|^2}\big(u^2 u_y + uv(v_y - u_x) - v^2 v_x\big), \\ d(\mathbf{x},t) &= \frac{1}{|\mathbf{u}|^2}(\mathbf{u}^{\perp})^*(\nabla\mathbf{u})\mathbf{u} \\ &= \frac{1}{|\mathbf{u}|^2}\big(u^2 v_x + uv(v_y - u_x) - v^2 u_y\big). \end{aligned}$$

The terms in the transformed linearized system (5.10) motivate the definition of Lagrangian fields as diagnostics for hyperbolic mixing and shear. Since our velocity field is slowly varying in time, the terms associated with $b(t)$ in (5.10) are neglected in these definitions.

5.4.3 R-field

As a consequence of incompressibility, the matrix $A(t)$ has the eigenvalues $\pm r(\mathbf{x}(t),t)$. Fixing an integration time T, the integrated field R,

$$R(\mathbf{x}_0,t_0) = \int_{t_0}^{t_0+T} r(\phi_{t_0}^{t_0+\tau}(\mathbf{x}_0),\tau)\,d\tau, \tag{5.11}$$

describes the growth of a perturbation in the direction orthogonal to the Lagrangian velocity, and the ratio $R/|T|$ plays the role of a finite-time Lyapunov exponent in this direction. Thus R is a measure of attraction ($R < 0$) or repulsion ($R > 0$) of nearby trajectories towards $\mathbf{x}(t)$ over the integration interval $[t_0, t_0+T]$. Due to incompressibility, expansion orthogonal to $\mathbf{u}$ is combined with contraction in the direction of $\mathbf{u}$ and vice versa.

We note that in the limit $T \to \infty$, R reduces to the mixing efficiency proposed by [Ott89], when this efficiency is evaluated in the direction orthogonal to $\mathbf{u}$. In our study, R

will be used as the main diagnostic field for hyperbolicity, and in addition as a means to predict mixing rates across the shear-lines defined below.

5.4.4 S-field

The term $s(\mathbf{x}, t)$ can be written in the form

$$s(\mathbf{x}, t) = \big(\nabla|\mathbf{u}(\mathbf{x}, t)|\big) \cdot \mathbf{u}^{\perp}(\mathbf{x}, t), \tag{5.12}$$

and hence characterizes the rate of change of the particle speed in the direction orthogonal to the velocity. Thus s is a local, Eulerian measure of shear in the fluid flow. We define the S-field by integrating s along trajectories,

$$S(\mathbf{x}_0, t_0) = \int_{t_0}^{t_0+T} s(\phi_{t_0}^{t_0+\tau}(\mathbf{x}_0), \tau)\, d\tau, \tag{5.13}$$

and use S as a Lagrangian diagnostic field for shearing.

We note that an alternative Lagrangian measure of shear has been defined in [HI03] using the non-diagonal entry of the fundamental matrix of $\dot{\eta} = A(t)\eta$. However, this field involves a double time-integral and is computationally more expensive. The S-field has a straightforward interpretation as shear-diagnostic due to (5.12), and requires less computational effort.

As in the case of the FTLE-field, we distinguish forward ($T > 0$) and backward ($T < 0$) fields for both R and S.

5.4.5 Shear-lines

For a given integration time T, we define the shear-line of strength C at initial time t_0 as the level contour of S, i.e.,

$$S_C = \{\mathbf{x}_0 \,|\, S(\mathbf{x}_0, t_0) = C\}.$$

High values of $|C|$ correspond to lines with high shear. For our model, the shear lines are all closed curves around the origin (distorted circles). Positive and negative values of S indicate that the Lagrangian speed increases when moving radially outwards and inwards, respectively. We refer to the first case as “normal propagating shear” and to the second case as “counter-propagating shear.” Hyperbolic mixing measured by R is associated with transport across the shear-lines. This will be used in Section 5.7 to define mixing rates.

5.5 Lagrangian fields and coherent structures

In Figures 5.1, 5.2, and 5.3 we show forward and backward FTLE-, S-, and R-fields, respectively, at the initial time $t_0 = 6\,\mathrm{hrs}$, after the polygonal eyewall has formed, and for integration times $T = \pm 15\,\mathrm{min}$, $T = \pm 30\,\mathrm{min}$, and $T = \pm 120\,\mathrm{min}$. For $T = \pm 15\,\mathrm{min}$, the FTLE-field (Figure 5.1a,b) reveals coherent structures near the polygonal eyewall, since the effect of the shear is not so pronounced over this short time range. For increasing $|T|$ the shear becomes dominant, and the FTLE-level contours evolve into distorted circles (Figure 5.1c–f). Comparison of the azimuthally averaged fields (Section 5.6) shows that high FTLE-values occur near extreme values of $\overline{\partial\omega/\partial r}$. While high FTLE-values correspond to high trajectory separation, they do not give clear LCS's (ridges) for longer integration times. LCS's can be seen only at very short integration times (Figure 5.1a,b), and in regions that are predicted by the Q-field. As integration time is increased (Figure 5.1c–f), the LCS's do lengthen as expected, but they also become broader. In particular, the LCS's for $T = \pm 15\,\mathrm{min}$ that are located near the corners of the eyewall, converge into a single broad ring that represents an annulus of high shear.

The S-field (Figure 5.2) is a shear-indicator, and its level contours (the shear-lines) are distorted circles for all integration times. The FTLE-field shows similar structures as the S-field for longer integration times, confirming that trajectory separation is mainly due to shear.

The R-field (Figure 5.3) shows structures of high and low R-values that persist over a series of integration times, making them coherent. These structures lengthen and become more resolved (narrower) when the integration time increases. Initial points on ridges and valleys have $R > 0$ and $R < 0$, indicating strong separation and contraction in the (approximately radial) direction orthogonal to the Lagrangian velocity, respectively. The structures exist in both the forward and backward time fields, and some of the forward and backward time structures have intersection points. Since the R-field is radially continuous, high values of the R-field lead to trajectories that show high net movement orthogonal to the Lagrangian velocity, and hence are more likely to cross shear-lines. Since the structures span across the shear-lines, they are not Lagrangian, as trajectories with high angular velocity pass trajectories with lower angular velocity.

A prominent feature of the forward R-field at $t_0 = 6\,\mathrm{hours}$ (and later) are the filaments observable in Figure 5.3a,c,e, which are a consequence of the polygonal eyewall. At $t_0 = 2\,\mathrm{hrs}$

(Figure 5.4a) no filaments are observed. The filamentation concerns the ridges and valleys, as well as the edges between them.

5.5.1 An advective mixing mechanism

Initial conditions $\mathbf{x}_0$ that satisfy $R(\mathbf{x}_0, t_0) = 0$ are invariant in the sense that there is no net movement of neighboring trajectories relative to the Lagrangian velocity. As can be seen in Figures 5.3 and 5.4a, ridges and valleys of R come in nearby pairs, and the ridge and valley of a pair are separated by a segment of a zero contour which forms (approximately) an edge of the R-field. The edge is neutrally stable, that is, it attracts from one side (from the ridge) and repels from the other side (towards the valley). The situation is illustrated in Figure 5.4a,c,d for $t_0 = 2\,\text{hrs}$. At this initial time the motion is almost circular (Figure 5.4b), but motion across shear-lines can be observed already.

Let $\mathcal{R}$ be a structure (ridge or valley) of R at initial time t_0. The structure is coherent in the sense that it evolves continuously, for varying initial time, into a structure $\mathcal{R}'$ seen as a ridge or valley of R at initial time $t_0 + \tau$. It is, however, not Lagrangian because it is not advected with the flow, that is, the image of $\mathcal{R}$ under the flow map, $\mathcal{R}_\tau = \phi_{t_0}^{t_0+\tau}(\mathcal{R})$, has advanced farther from $\mathcal{R}$ than $\mathcal{R}'$, and is not a structure of R at $t_0 + \tau$. (Figure 5.5a). Generally we observe that the coherent structures move at a slower rotational speed than that of the mean flow, which can be attributed to the effect of Rossby waves [ML97].

A coherent structure $\mathcal{R}$ has a leading and a lagging end relative to counterclockwise rotation. Concerning the evolution of $\mathcal{R}$ under the flow map, two cases can occur for structures computed in a forward time integration:

(a) If the leading end is at higher angular velocity than the lagging end, then the image $\mathcal{R}_T$ of $\mathcal{R}$ under $\phi_{t_0}^{t_0+T}$ is lengthened over the integration and tends to align with a contour of the S-field (Figure 5.5b).

(b) If the leading end is at lower angular velocity than the lagging end, then the flow map rotates $\mathcal{R}$, and for sufficiently large T the image $\mathcal{R}_T$ tends to align with a contour of the S-field in the opposite direction (Figure 5.5c).

For a nearby pair of a ridge and a valley, the relative position of their flow map images is preserved in case (a), whereas in case (b) they switch position. This rotation and position switching are a mechanism for the advective mixing during the polygonal eyewall stage. The

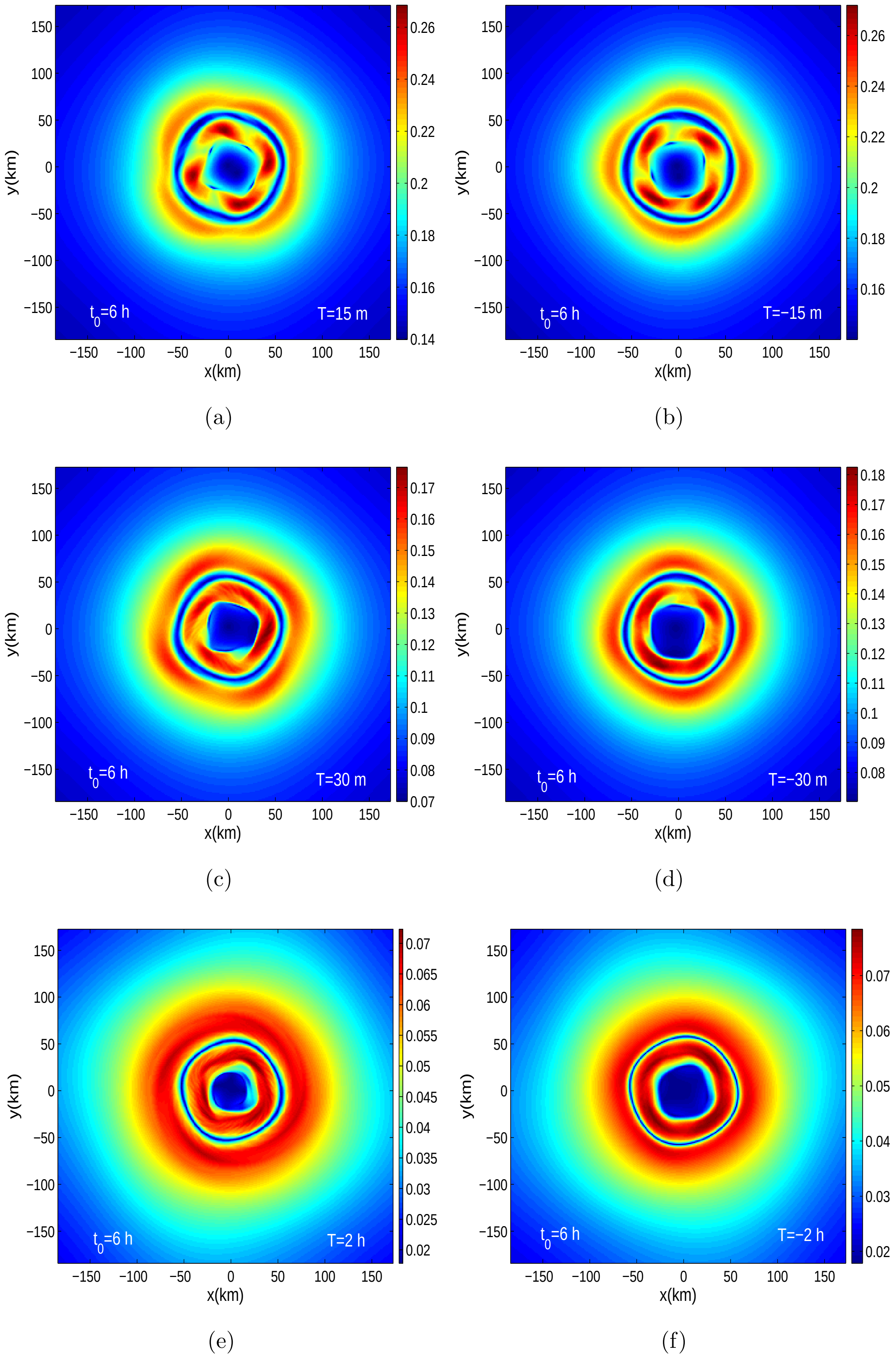

Figure 5.1: Forward and backward FTLE-fields at the initial time $t_0 = 6$ hours integrated (a) 15 min, (b) −15 min, (c) 30 min, (d) −30 min, (e) 120 min, and (f) −120 min.

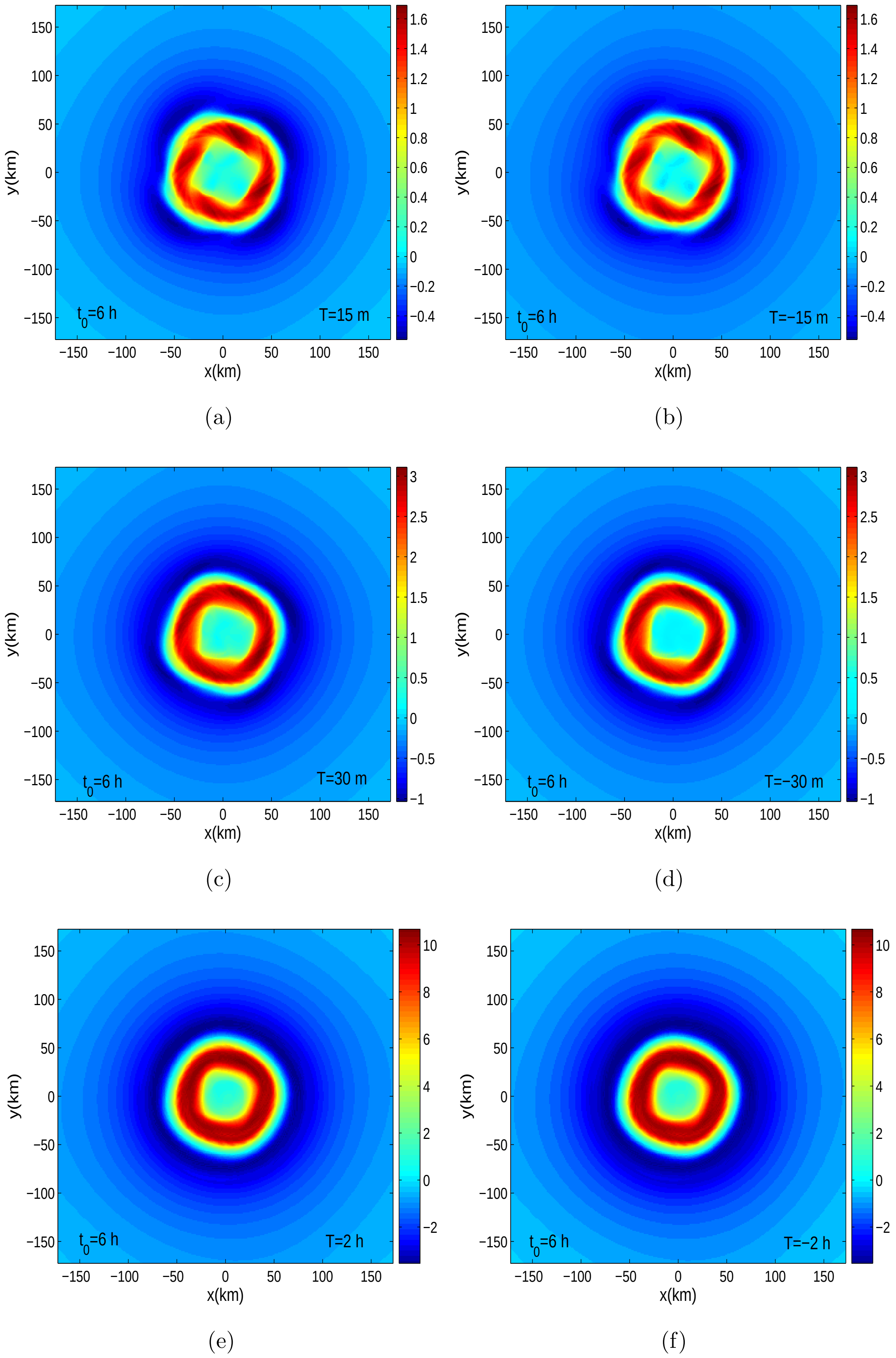

Figure 5.2: Forward and backward S-fields at the initial time $t_0 = 6$ hours integrated (a) 15 min, (b) −15 min, (c) 30 min, (d) −30 min, (e) 120 min, and (f) −120 min.

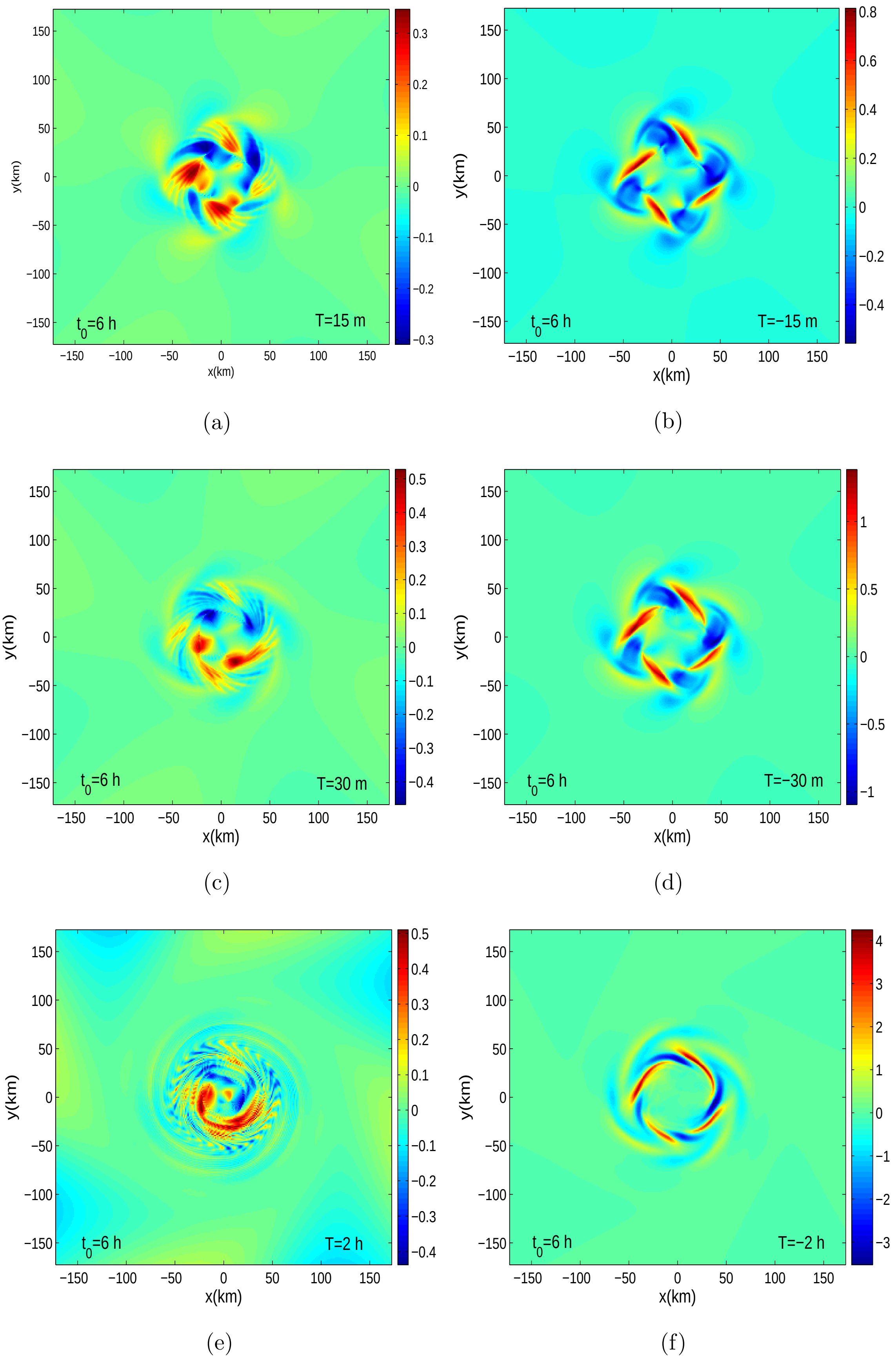

Figure 5.3: Forward and backward R-fields at the initial time $t_0 = 6$ hours integrated (a) 15 min, (b) −15 min, (c) 30 min, (d) −30 min, (e) 120 min, and (f) −120 min.

square eyewall gives four valleys and ridges aligned in a way that four sets of trajectories pass from outside to inside and four from inside to outside of an S-contour. The combination of ridge-edge-valley sets of R, aligned with the leading ends at lower angular velocity, can be seen as an indicator of fluid regions that will roll into mesovortices over the forward integration time. Thus the strength and size of the surrounding ridges and valleys are an indicator of the potential flux in and out of the mesovortex.

5.6 Field diagnostics for varying initial time

In Figures 5.6–5.11 we show in (a) the relative vorticity, in (b) the Q-field, and in (c) the R-field with overlayed vorticity contours chosen to illustrate the relation between R-field structures, and vorticity structures. We show the S-field, integrated Q-field, and FTLE field in (d), (e), and (f) respectively, together with contours (from inside to outside) of the maximum normal propogating shear, the maximum tangential velocity, and the maximum counterpropogating shear. The initial times in these figures are $t_0 = 2\,\text{hrs}$, $4\,\text{hrs}$, $6\,\text{hrs}$, $8\,\text{hrs}$, $10\,\text{hrs}$, and $12\,\text{hrs}$, and the integration time is $T = 1\,\text{hr}$.

Since the shear-lines are distorted circles, we can interpret the average $\overline{\sigma}(r_0, t_0)$ ($r_0 = |\mathbf{x}_0|$) as radial mixing rate. In all Figures 5.6–5.11 (d-f) we observe that extreme $\widehat{Q}$, S, and FTLE-values occur at extrema of $\overline{\partial\omega/\partial r}$, demonstrating that the $\widehat{Q}$, S, and FTLE-fields are dominated by the shear. A similar interpretation as radial mixing rates can be attributed to the averages $\overline{S}(r_0, t_0)$ and $\overline{R}(r_0, t_0)$. Plots of $\overline{S}$ and $\overline{\sigma}$reveal these two averages are very similar in structure, as both measure shear. The quantity $\overline{R}$ can be interpreted as a measure of hyperbolic mixing, which is important for transport through the eyewall.

5.6.1 2–4 hours: Initial state

At the initial time of 2 hours (Figure 5.6), the model is still close to the initial state and shows a broad ring of high vorticity fluid. While the vorticity, Q, S, and FTLE-fields are almost circular-symmetric, the R-field shows distinct lines of high radial mixing, demostrating that coherent structures can persist through dominant shear. The wavenumber four asymmetry begins to show in the R-field, particularly in the forward time integration, atthough the initial vorticity profile is nearly preserved, with any asymmetries barely noticible. The rotation of the R-ridges and valleys in this stage allows the crystallization that is neccessary for mesovortex formation.

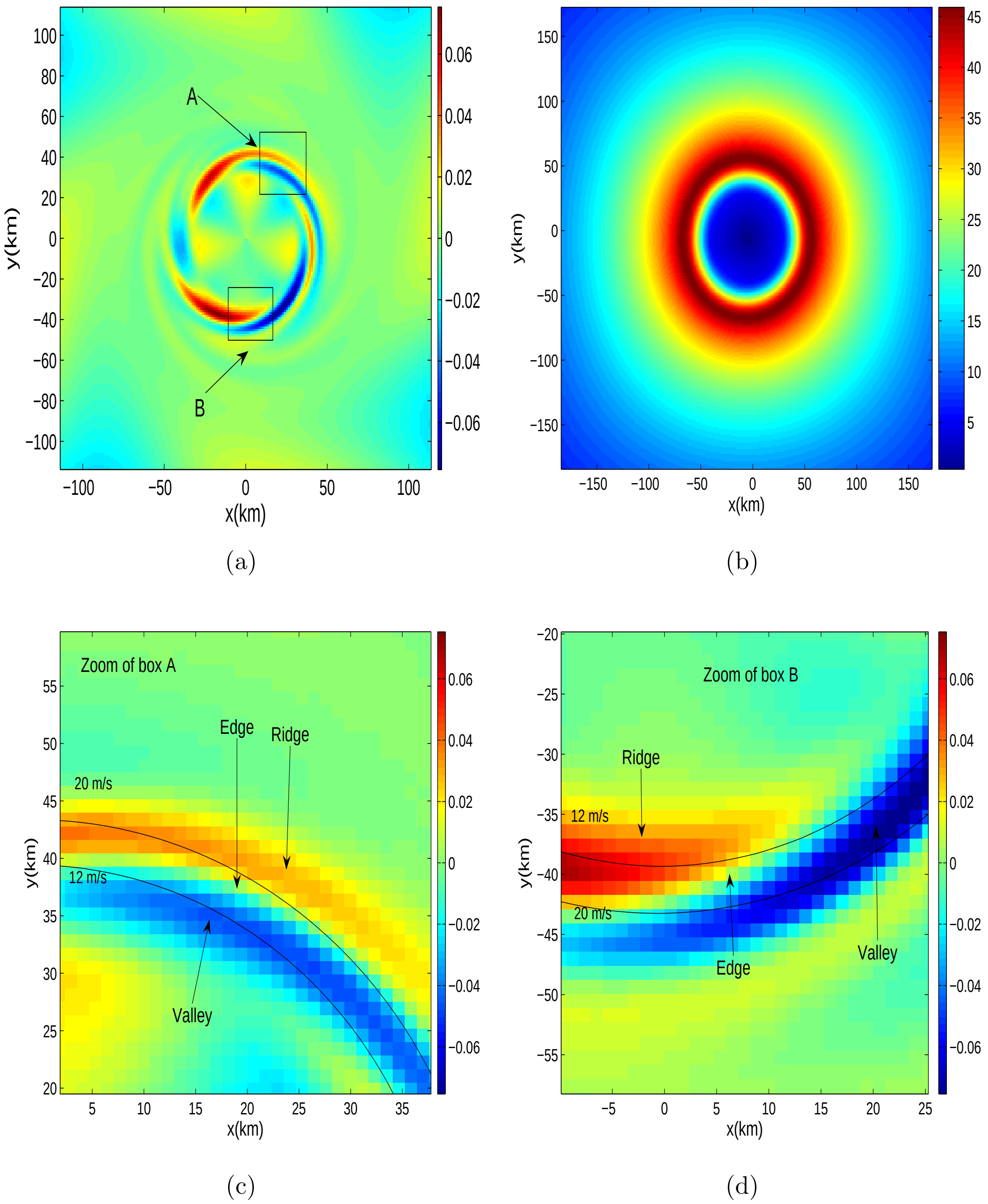

Figure 5.4: (a) R-field with ridges and valleys and (b) Lagrangian speed at $t_0 = 2\,\text{hrs}$. (c) Zoom of box A from R-field showing repelling edge, and (d) zoom of box B showing attracting edge. Integration time is $T = 60\,\text{min}$. Black lines show the azimuthal velocity at the initial time.

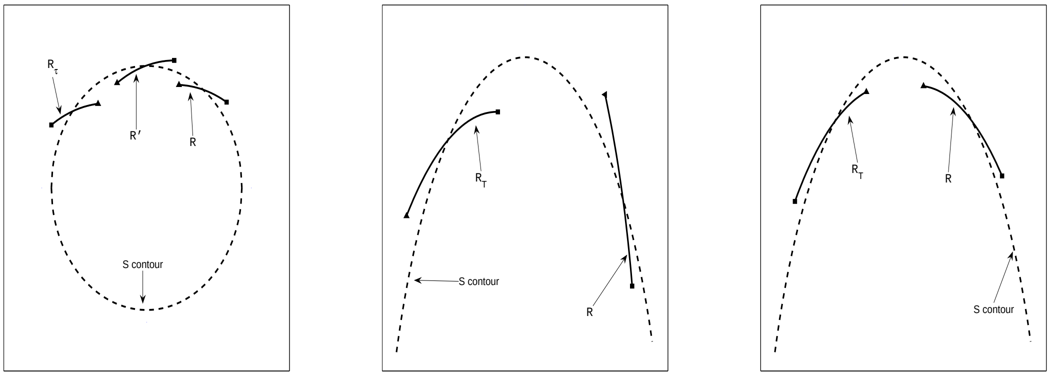

(a) (b) (c)

Figure 5.5: (a) Sketch of a structure $\mathcal{R}$ of R at initial time t_0, the associated structure $\mathcal{R}'$ of R at initial time $t_0 + \tau$, and the flow map image $\mathcal{R}_\tau = \phi_{t_0}^{t_0+\tau}(\mathcal{R})$, illustrating the non-Lagrangian nature of the coherent structures. (b) Structure $\mathcal{R}$ crossing an S contour with speed above the contour higher than the speed below, and flow map image $\mathcal{R}_T$ after an integration time. Leading and lagging ends of $\mathcal{R}$ and their images on $\mathcal{R}_T$ are marked by a triangle and a square, respectively. (c) Same as (b) with opposite orientation of $\mathcal{R}$ relative to the contour, leading to a rotation of $\mathcal{R}_T$.

At 4 hours (Figure 5.7), much of the symmetry of the initial state still remains. A forward time integration begins to display asymmetries in the Q, FTLE- and S-fields, whereas the R-field retains the structures that were present at 2 hours. At 4 hours the backward time integration of R (not shown) also shows regions of high orthogonal separation.

5.6.2 6–8 hours: Polygonal eyewall

At 6 hours (Figure 5.8), the vorticity field shows a polygonal eyewall structure, where the flow resembles a nonlinear critical layer for dry barotropic instability. A square inner eyewall structure forms, with pools of low vorticity fluid organized into the corners of the eye. The fluid is largely unmixed, with low vorticity fluid organized in the mesovortices, where it is largely protected from the outer flow. Since vorticity is materially conserved, low vorticity fluid from the eye and environment must replace the fluid that left the eyewall. The fluid that is mixed across the boundaries is consistent with the ridges and valleys of the R-field. The filamentation that develops from the stretching of high vorticity fluid that exits from the vorticity ring to the environment, can be seen in the form of spiral bands in the vorticity field.

The Q-field shows that, instantaneously, high trajectory separation occurs along the square boundary of the inner eyewall. The pools of low vorticity show instantaneous contraction. The outer vorticity ring shows high trajectory separation. Even when the FTLE-fields are calculated for the small integration time of $T = 3$ minutes, there is a noticible difference between the separation points of the Q-field and the FTLE-field. The square eyewall formation corresponds to four structures of high FTLE-values in both the forward and backward time fields for short integration times. As integration time is increased, the structures lengthen and are no longer distinguishable.

The R field shows a series of ridges and valleys that originated as coherent structures from the earlier times, but are not as refined as previous structures. There are also structures emanating outward from the ring of high vorticity that may play the role of protecting the ring from interaction with the outer flow [DMW09]. If our model was a true representation of a wave critical layer, the structures would correspond to dividing streamlines, but the high shear prohibits this. The maximal R-regions are located at the same places that show high FTLE-values, but with much greater resolution than the FTLE-fields, which are blurred by the shear.

At 8 hours (Figure 5.9), the polygonal eyewall structure that is present at 6 hours is still clearly visible. The R-field has similar properties as the R-field at 6 hours (Figure 5.8), with the coherent structures begining to merge, showing intense mixing.

5.6.3 Later state: mixing into a monopole

The period after $t_0 = 8$ hours until $t_0 = 12$ hours exhibits intense mixing that leads to a collapse into a monopole end state.

For $t_0 = 10$ hours (Figure 5.10), the Q-field is less square, and the R-field shows high mixing in two distinct regions, one with expansion and one with contraction. The region of expansion is inside the ring of high vorticity, while the region of contraction has become organized in the dominant mesovortex, which is the "winner" and survives to become the primary vortex during the collapse into the monopole end state, Note that the merging of LCS's into a single LCS is a bifurcation, and cannot happen if they represent true stable and unstable manifolds, however the coherent structures here are not entirely Lagrangian, yet their interactions and bifurcations play an important role in the systematic mixing during mesovortex interaction. As more advection (stirring) in and out of the eyewall occurs, there is filamentation of the initial vorticity-contours with diffusive mixing occurring along the lengthening contour boundaries, leading to an "averaging" of vorticity values through diffusion.

For $t_0 = 12$ hours (Figure 5.11), the inner ring of vorticity has broken down. The FTLE- and S-fields show the outer rings converged as a thick ring, and the model is entering the monopole state. The R-field coherent structures now show the dominant mesovortex migrating to the center and the other mesovortices are disappearing due to their annihilation by the dominant mesovortex. Regions of high R-values are pushed outward, indicationg mixing with the outer flow. At this stage, there is a single remaining protecting R-ridge, on the outside of the remaining high vorticity ring, which has served the role of protecting the mesovortex that eventually becomes the "winner".

Beyond 12 hours, the initial regions of vorticity are not recognizable, and high (although not as high as the initial state) vorticity fluid begins to organize into the eye. The low vorticity fluid from the eye becomes well mixed, and the eyewall and environment become filled with relatively low vorticity fluid. The angular velocity gradient decreases, and the S field shows no eyewall.

Although the fluid that is mixed beyond 12 hours is not distinguishable based on its initial vorticity, the R-field still gives regions of advective mixing, showing that the moving frame of initial conditions still shows regions of fluid that are transported.

5.7 Mixing rates

The radial mixing rates $\overline{\sigma}(r_0, t_0)$ and $\overline{S}(r_0, t_0)$ quantify mixing due to shear, whereas $\overline{R}(r_0, t_0)$ quantifies hyperbolic mixing. In these mixing rates, the lines along and across which mixing is quantified are circles. Hyperbolic mixing rates that are more closely related to the shearing structures are mixing rates which quantify transport across shear-lines (level contours S_C of S, see Section 5.4.2).

5.7.1 Measured mixing rate

Given a level-contour S_C of the S-field and an integration time T, we define the mixing rate $R_m(C, t_0)$ as the area of initial conditions whose trajectories cross S_C during $[t_0, t_0 + T]$, divided by the length of the contour. This mixing rate is computed ("measured") by seeding a grid of initial conditions and counting trajectories which cross S_C.

5.7.2 Predicted mixing rate

We define a predicted mixing rate through the R-field as follows. Let r_C be the average radius along S_C. If $R(\mathbf{x}_0, t_0) > 0$ and $\mathbf{x}_0 = r_0(\cos\theta_0, \sin\theta_0)^*$ with $r_0 < r_C$, $\mathbf{x}_0$ is inside the circle with radius r_C, and the trajectory $\phi_{t_0}^t(\mathbf{x}_0)$ is repelling. Thus trajectories seeded on the ray with angle θ_0 and radial values slightly above r_0 move outwards, towards the circle with radius r_C. This suggests to define a boundary point $(r_C - \delta(\theta_0), \theta_0)$ through the condition

$$e^{R(r_0,\theta_0,t_0)}\delta(\theta_0) + r_0 = r_C. \tag{5.14}$$

Points on the θ_0-ray above this boundary point and below r_C can be expected to cross the r_C-circle. If $r_0 > r_C$ and $R(\mathbf{x}_0, t_0) > 0$, trajectories on the ray θ_0 with radial values slightly below r_0 move inwards, towards the circle with radius r_C again, which leads to the same boundary point (5.14), now with $\delta(\theta_0) < 0$. If $R(\mathbf{x}_0, t_0) < 0$, the trajectory is attracting, and initial conditions on the opposite side of the r_C-circle move towards this circle, provided $\mathbf{x}_0$ is sufficiently close to that circle. The corresponding boundary point is then defined by

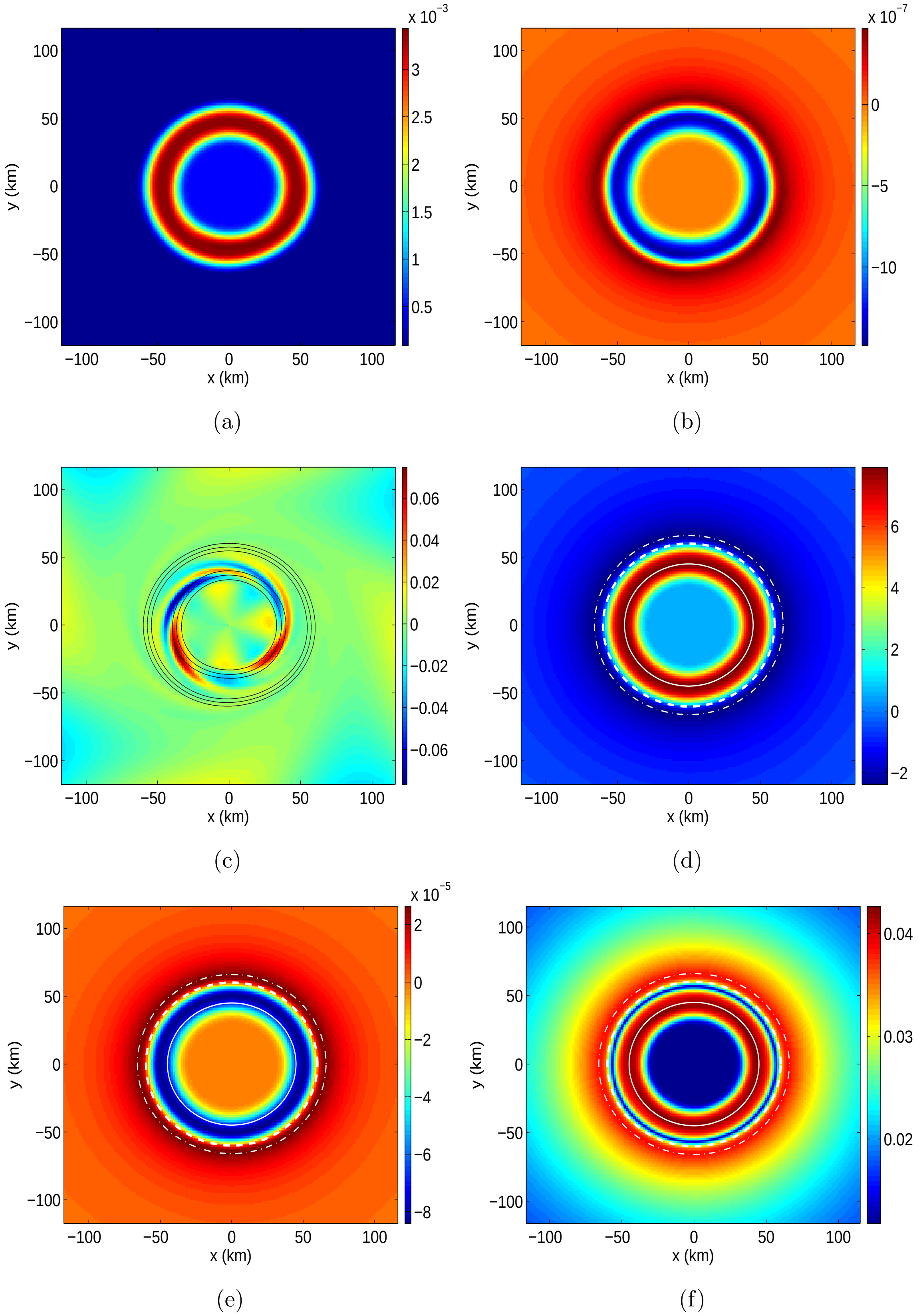

Figure 5.6: (a) Relative vorticity field, (b) Q-field, (c) R-field with vorticity contours overlayed to relate structures, (d) S-field, (e) integrated Q-field $\widehat{Q}$, and (f) $FTLE$-field for initial time of $t_0 = 2\,\text{hrs}$ with integration time $T = 1\,\text{hr}$. The white contours in (d)-(f) mark the radius of maximum $\frac{\partial \omega}{\partial r}$ (inner, solid), the radius of maximum tangential wind (middle, dashed), and the radius of maximum counterpropogating $\frac{\partial \omega}{\partial r}$ (outer, dash-dot).

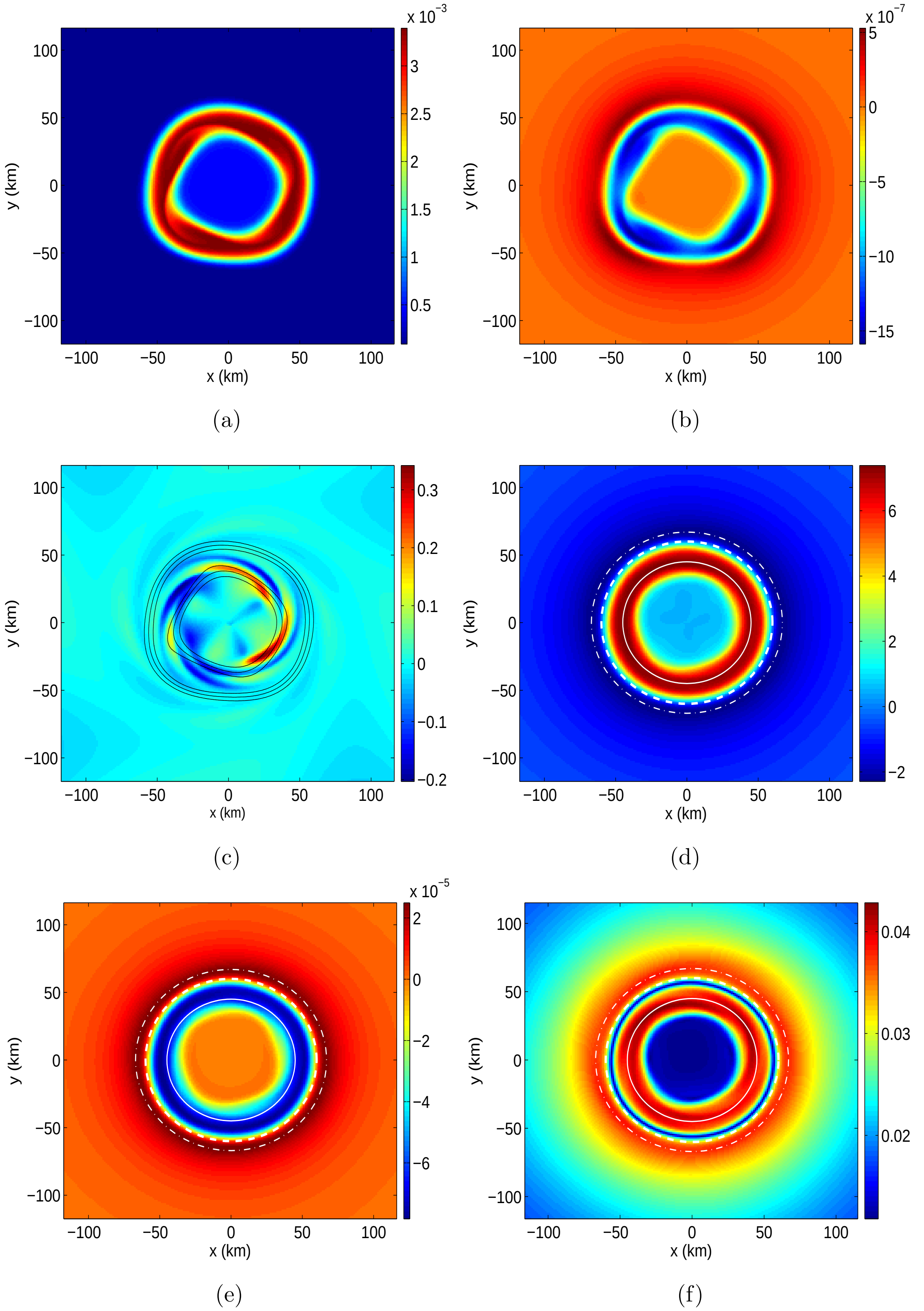

Figure 5.7: (a) Relative vorticity field, (b) Q-field, (c) R-field with vorticity contours overlayed to relate structures, (d) S-field, (e) integrated Q-field $\widehat{Q}$, and (f) $FTLE$-field for initial time of $t_0 = 4\,\text{hrs}$ with integration time $T = 1\,\text{hr}$. The white contours in (d)-(f) mark the radius of maximum $\frac{\partial \omega}{\partial r}$ (inner, solid), the radius of maximum tangential wind (middle, dashed), and the radius of maximum counterpropogating $\frac{\partial \omega}{\partial r}$ (outer, dash-dot).

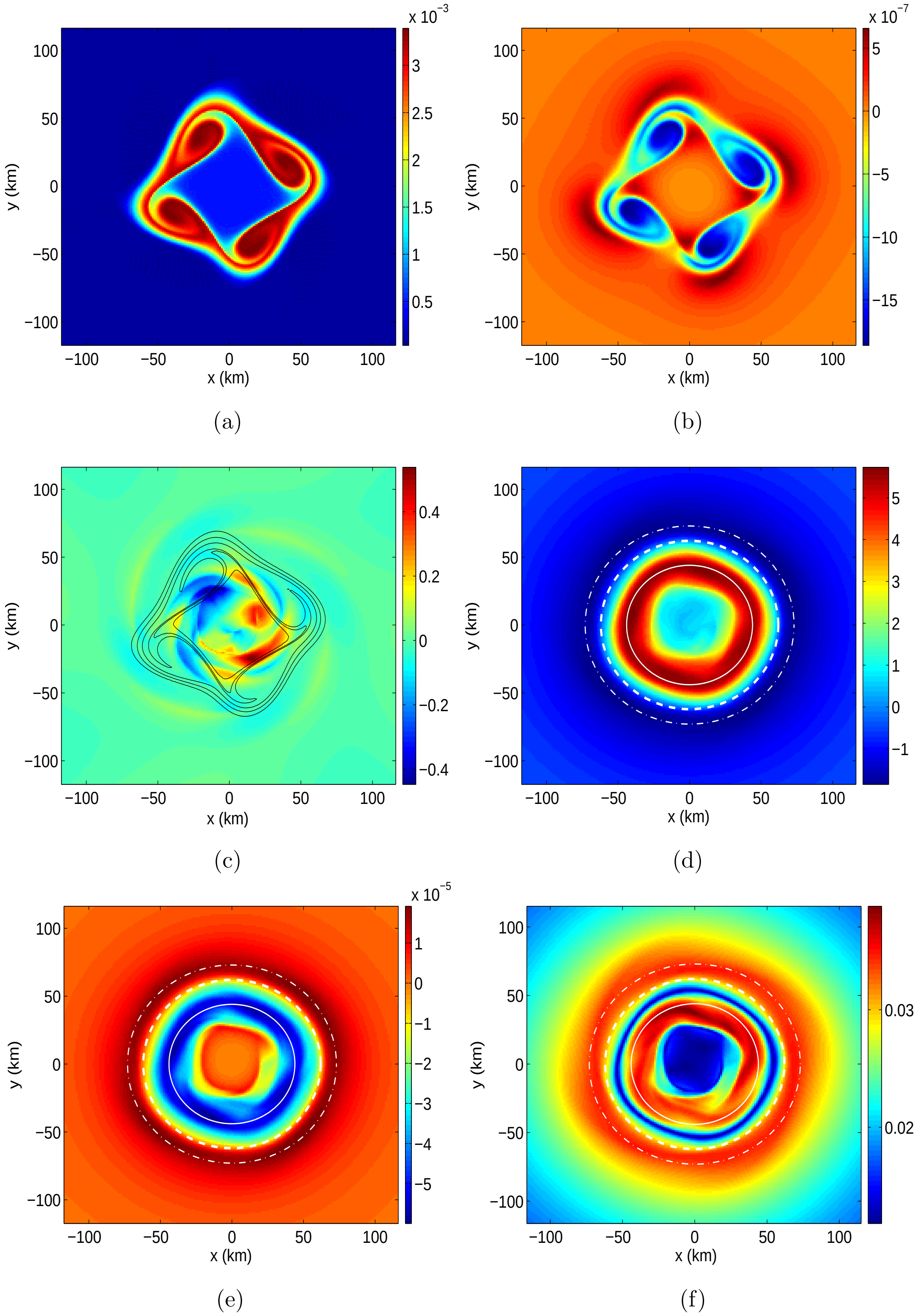

Figure 5.8: (a) Relative vorticity field, (b) Q-field, (c) R-field with vorticity contours overlayed to relate structures, (d) S-field, (e) integrated Q-field $\widehat{Q}$, and (f) $FTLE$-field for initial time of $t_0 = 6$ hrs with integration time $T = 1$ hr. The white contours in (d)-(f) mark the radius of maximum $\frac{\partial \omega}{\partial r}$ (inner, solid), the radius of maximum tangential wind (middle, dashed), and the radius of maximum counterpropogating $\frac{\partial \omega}{\partial r}$ (outer, dash-dot).

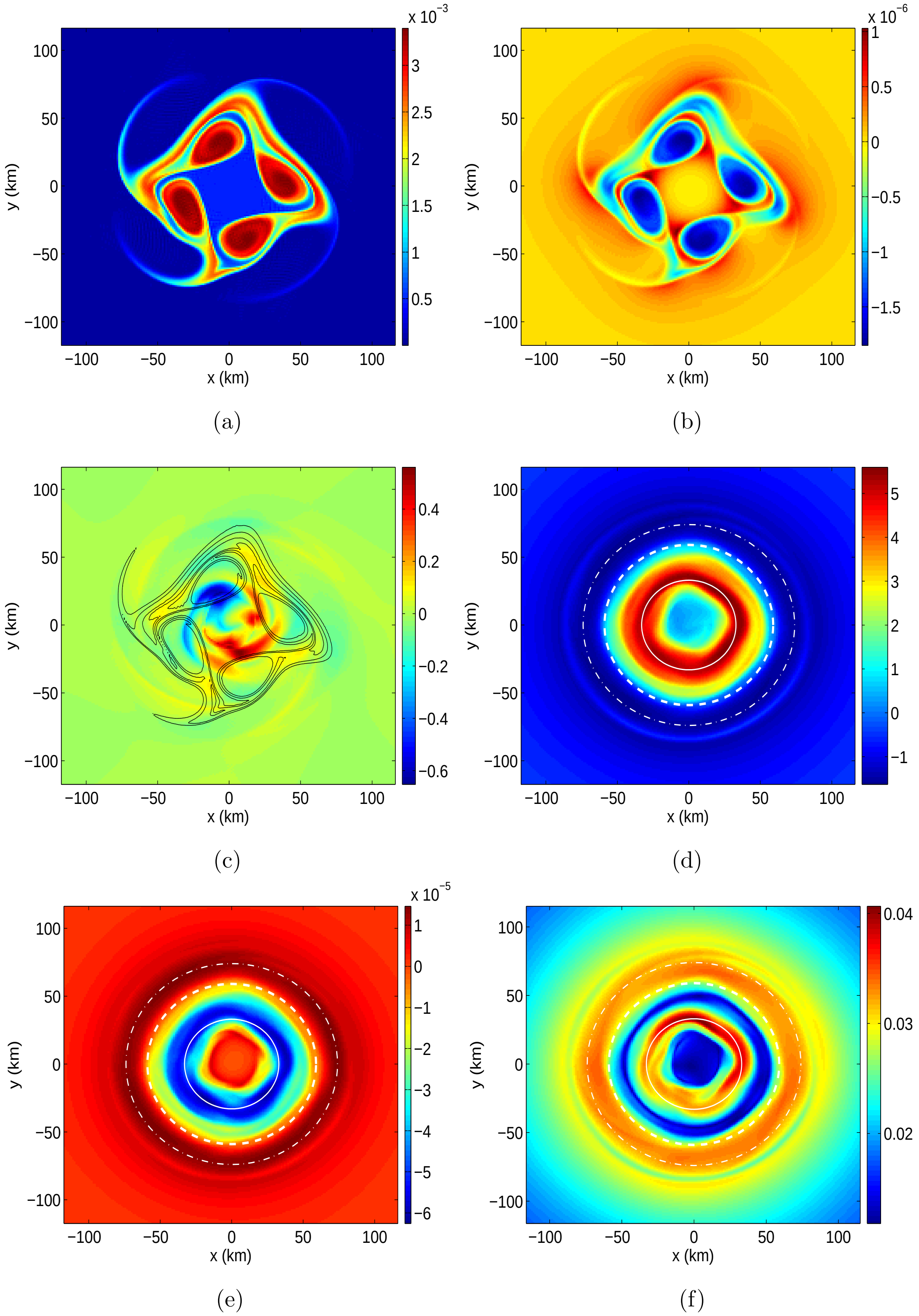

Figure 5.9: (a) Relative vorticity field, (b) Q-field, (c) R-field with vorticity contours overlayed to relate structures, (d) S-field, (e) integrated Q-field $\widehat{Q}$, and (f) $FTLE$-field for initial time of $t_0 = 8\,\text{hrs}$ with integration time $T = 1\,\text{hr}$. The white contours in (d)-(f) mark the radius of maximum $\frac{\partial \omega}{\partial r}$ (inner, solid), the radius of maximum tangential wind (middle, dashed), and the radius of maximum counterpropogating $\frac{\partial \omega}{\partial r}$ (outer, dash-dot).

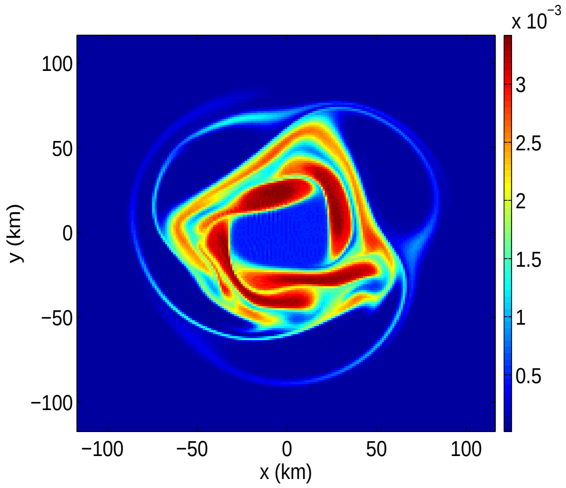

(a)

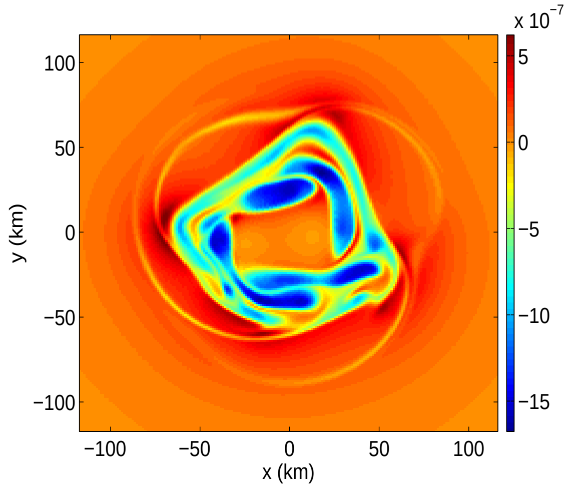

(b)

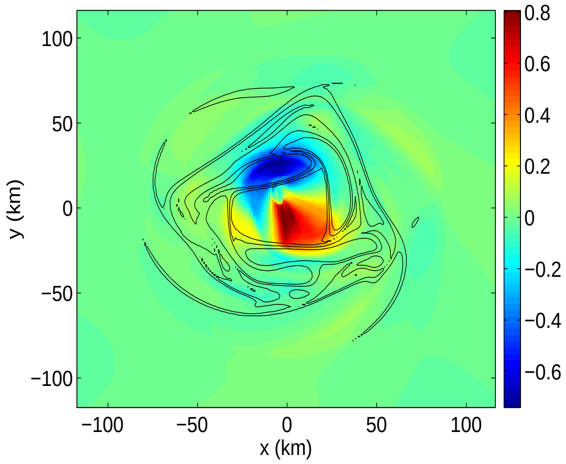

(c)

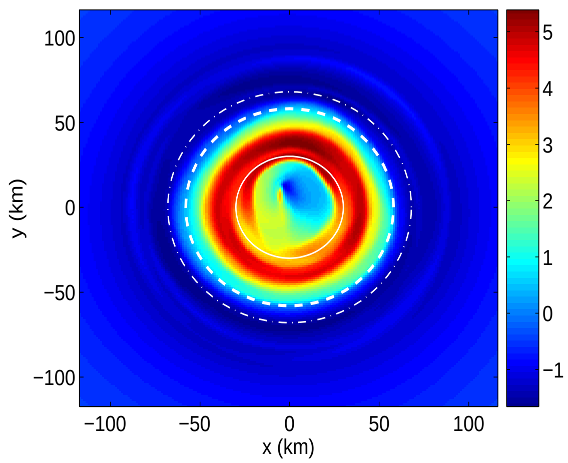

(d)

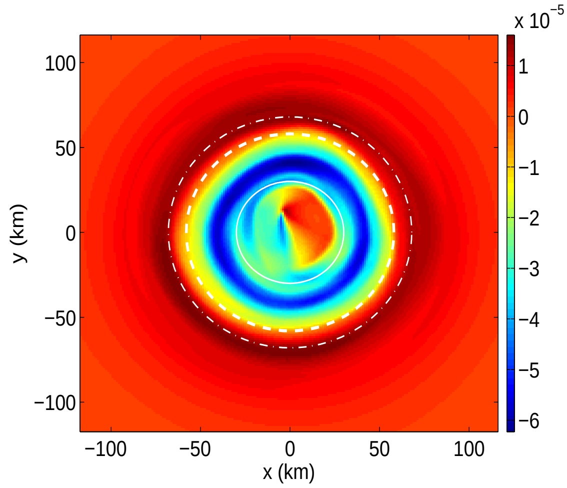

(e)

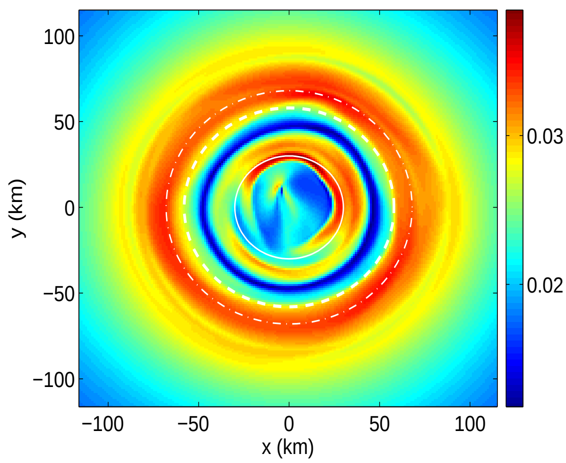

(f)

Figure 5.10: (a) Relative vorticity field, (b) Q-field, (c) R-field with vorticity contours overlayed to relate structures, (d) S-field, (e) integrated Q-field $\widehat{Q}$, and (f) $FTLE$-field for initial time of $t_0 = 10\,\text{hrs}$ with integration time $T = 1\,\text{hr}$. The white contours in (d)-(f) mark the radius of maximum $\frac{\partial \omega}{\partial r}$ (inner, solid), the radius of maximum tangential wind (middle, dashed), and the radius of maximum counterpropogating $\frac{\partial \omega}{\partial r}$ (outer, dash-dot).

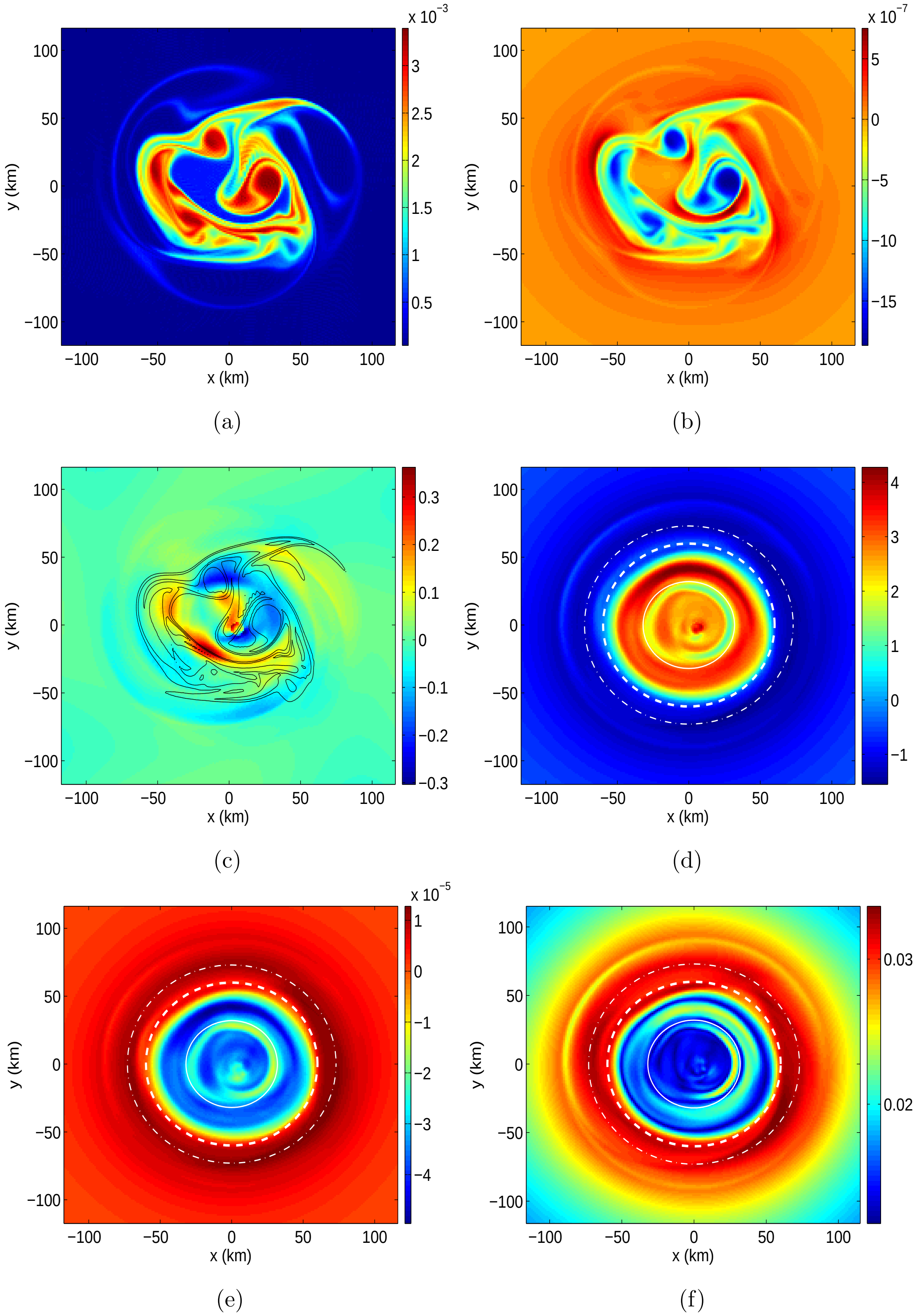

Figure 5.11: (a) Relative vorticity field, (b) Q-field, (c) R-field with vorticity contours overlayed to relate structures, (d) S-field, (e) integrated Q-field $\widehat{Q}$, and (f) $FTLE$-field for initial time of $t_0 = 2\,\text{hrs}$ with integration time $T = 1\,\text{hr}$. The white contours in (d)-(f) mark the radius of maximum $\frac{\partial \omega}{\partial r}$ (inner, solid), the radius of maximum tangential wind (middle, dashed), and the radius of maximum counterpropogating $\frac{\partial \omega}{\partial r}$ (outer, dash-dot).

$(r_C + \delta(\theta_0), \theta_0)$, where δ satisfies

$$e^{R(r_C,\theta_0,t_0)}\delta(\theta_0) + r_C = r_0. \tag{5.15}$$

By varying θ_0, the conditions (5.14) for $R > 0$ and (5.15) for $R < 0$ define an annulus of initial conditions around the r_C-circle, whose area we use to define the predicted mixing rate $R_p(C, t_0)$. This mixing rate is an approximation of the measured mixing rate. Of course, several approximations and simplifying assumptions are involved in this definition, but the results obtained make sense and the structure of R_p is similar to the structure of R_m.

Color-coded plots of the mixing rates $\overline{\sigma}(r_0, t_0)$, $\overline{S}(r_0, t_0)$, $\overline{R}(r_0, t_0)$, $R_m(C, t_0)$, and $R_p(C, t_0)$ are displayed in Figures 5.13, 5.14, 5.15, 5.16, and 5.17, respectively, for integration times $T = 30\,\text{min}$ and $T = 1\,\text{hr}$. The rates $\overline{\sigma}$ and $\overline{S}$ should be compared to the average angular velocity $\overline{\omega}$ and its radial derivative $\overline{\partial\omega/\partial r}$ shown in Figure 5.12. These rates are measures of shear and show the highest shear during the initial 6 hours, with the amount of shear dissipating as hyperbolic mixing begins to occur during the polygonal eyewall stage.

The hyperbolic mixing is captured by $\overline{R}(r_0, t_0)$, $R_m(C, t_0)$, and $R_p(C, t_0)$. All of these rates show that high hyperbolic mixing begins with the polygonal eyewall formation at 6 hours and continues through the transition to a high vorticity eye at 24 hours. In particular, the measured and predicted mixing rates $R_m(C, t_0)$ and $R_p(C, t_0)$ are very similar in structure, and reveal strong mixing near the zero S-contour S_0 (jet).

We note that [HS09] studied mixing for the same barotropic model using the concept of effective diffusivity [SH03, Nak96]. This quantity was computed at the initial time $t_0 = 0$, and with an integration time $t \equiv T$ (flow map ϕ_0^t) varying over the full duration of the model run of 48 hours. The effective diffusivity yields a mixing rate that depends on r and t. Our mixing rates have a similar dependence on t_0 as the mixing rate of [HS09] had on t, due to our moving frame approach. The mixing rate of [HS09] shows two radial regions, at approximately $r = 30$ km and $r = 50$ km, where high mixing occurs during $t = 6$ and $t = 32$ hours. The similar time and spatial regions associated with the same high mixing in our study occur for $\overline{\sigma}$ and $\overline{S}$ during $t_0 = 6$ and $t_0 = 24$ hours, when the band of low FTLE-values (the jet) is less prominent and more hyperbolic mixing occurs. The mixing rates $R_m(C, t_0)$ and $R_p(C, t_0)$ show very similar times of high mixing as the mixing rate of [HS09], and the S-contours for which these high rates occur are located approximately at the same radial values noted above.

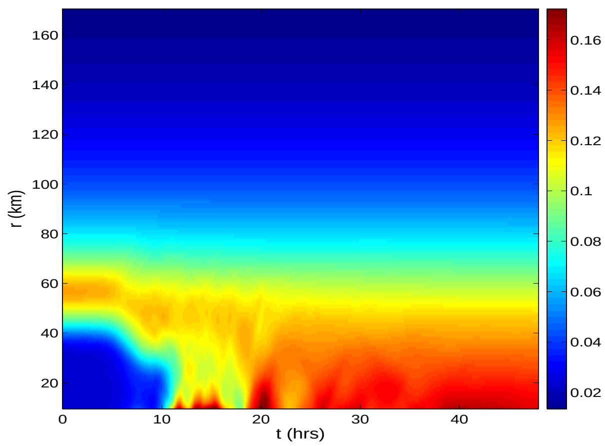

(a)

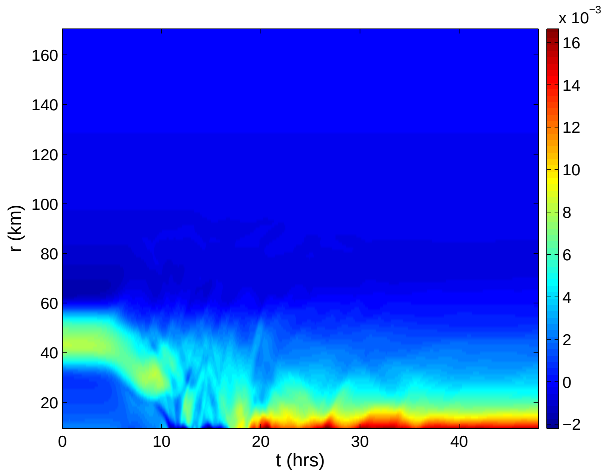

(b)

Figure 5.12: (a) Averaged angular velocity $\overline{\omega}(r,t)$, and (b) averaged radial derivative $\overline{\partial\omega/\partial r}$ for $t = 0 - 48\,\text{hrs}$.

High R-values determine sets of trajectories that show growth orthogonal to the Lagrangian velocity, and result in filamentation that enables turbulent diffusion to occur. The R-field gives an advective measure that converges on very short time scales, yet still yields similar mixing rates as the effective diffusivity obtained by integration over the full model time.

5.8 Concluding remarks

We have characterized Lagrangian mixing in a two-dimensional, nondivergent barotropic model for hurricane-like vortices through several diagnostic techniques. For this model, the

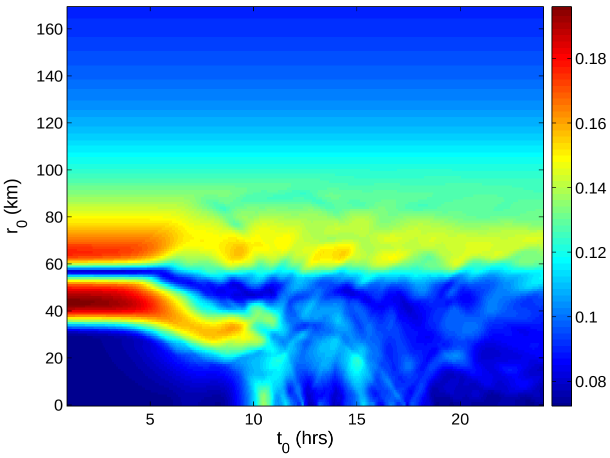

(a)

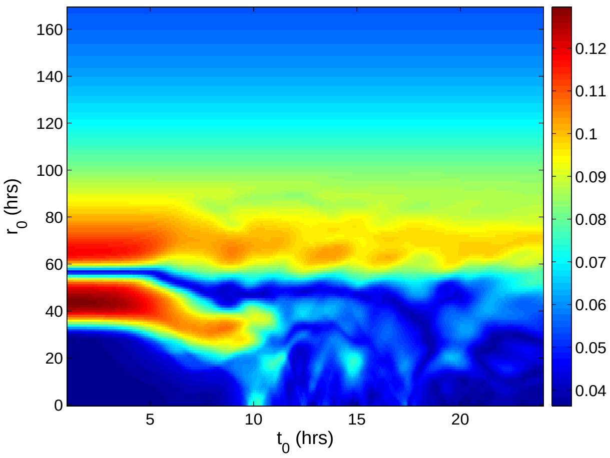

(b)

Figure 5.13: Radial FTLE-values $\overline{\sigma}(r_0, t_0)$ for integration times (a) 30 min and (b) 1 hr.

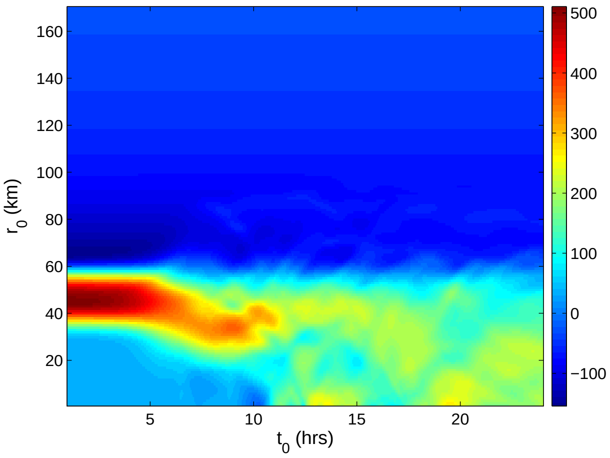

(a)

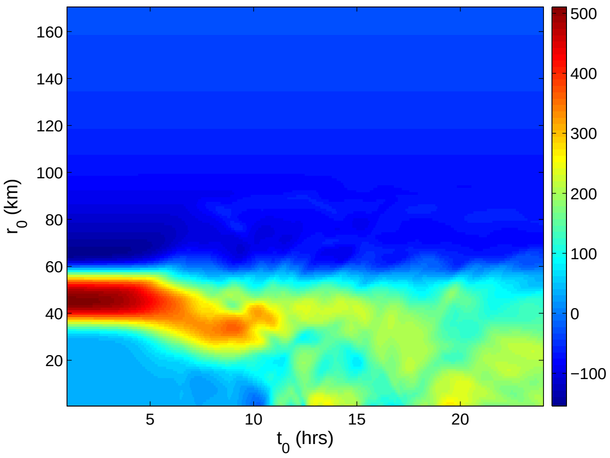

(b)

Figure 5.14: Radial S-values $\overline{S}(r_0, t_0)$ for integration times (a) 30 min minutes and (b) 1 hr.

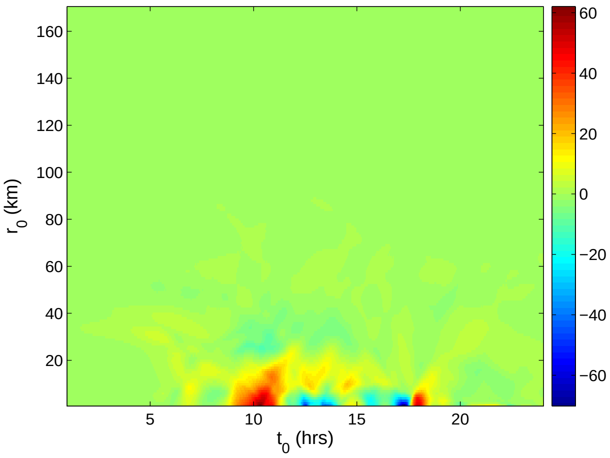

(a)

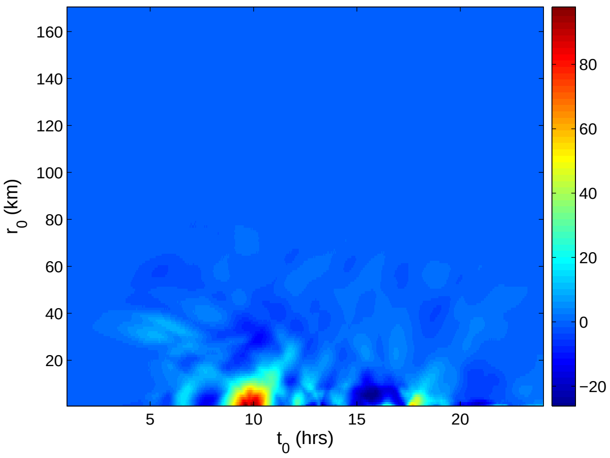

(b)

Figure 5.15: Radial R-values $\overline{R}(r_0, t_0)$ for integration times (a) 30 min minutes and (b) 1 hr.

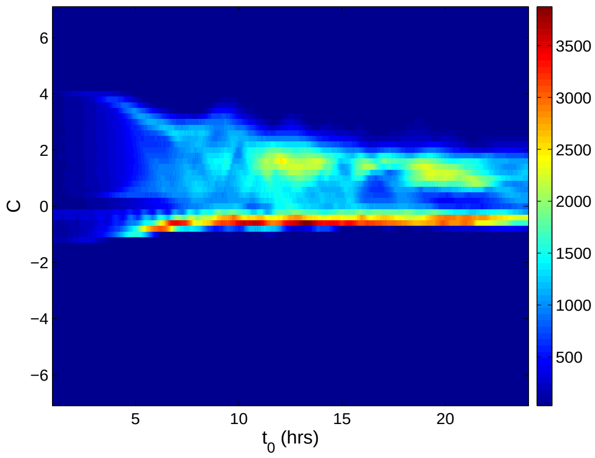

(a)

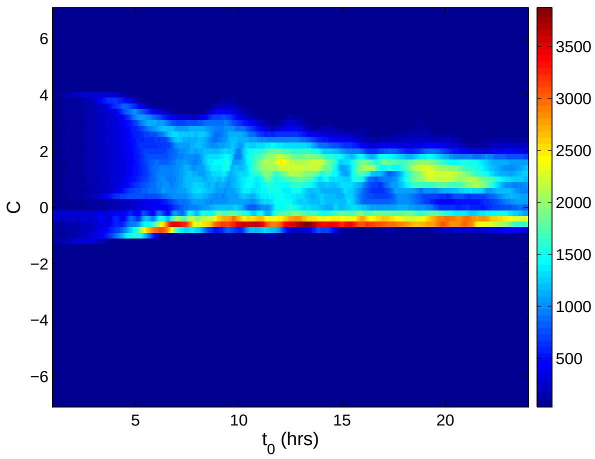

(b)

Figure 5.16: Measured mixing rate versus $R_m(C, t_0)$ across shear-lines S_C for integration times (a) 30 min minutes and (b) 1 hr.

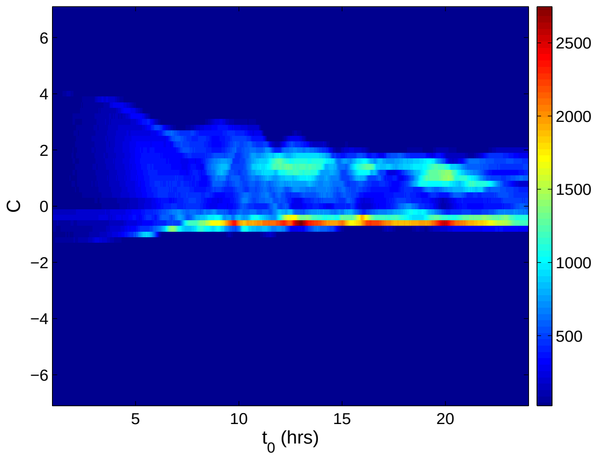

(a)

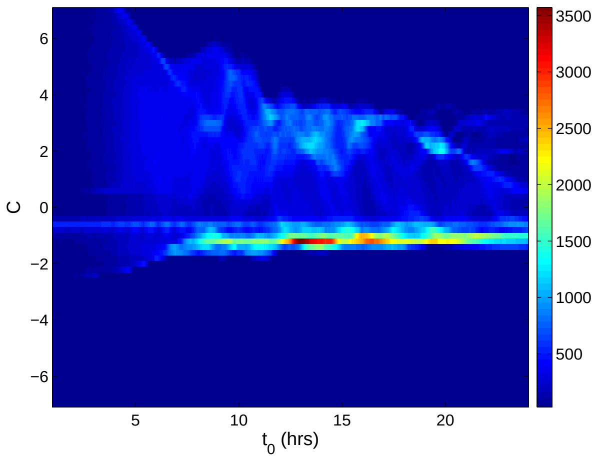

(b)

Figure 5.17: Predicted mixing rate $R_p(C, t_0)$ across shear-lines S_C for integration times (a) 30 min minutes and (b) 1 hr.

field of finite-time Lyapunov exponents provided a measure of total particle separation, but it did not separate the effects of hyperbolicity and shear, and did not show distinct coherent structures. In order to separate the effects of the high shearing occurring in the model from hyperbolic mixing, the trajectory separation was decomposed in directions along and normal to the Lagrangian velocity. This decomposition gave rise to two Lagrangian fields, the R-field and the S-field, which quantified the relative contributions of hyperbolicity and shear to the mixing process, respectively. In this approach, shear-lines and shear-strengths were identified with level-contours and level-values of the S-field.

The R-field showed coherent structures which impacted the mixing and mesovortex interaction, even through high shear. The outer ridges of the R-field were also involved in protecting the mesovortices from environmental flow, and the persistance of the ridges was associated with the dominance of particular mesovortices over others. In contrast to the other Lagrangian methods showed that the R-field was able to distinguish not only regions of high mixing, but also the structures that were involved in the evolution and annihilation of mesovortices. Future work will be devoted to study the impact of coherent structures on mesovortex interaction during tropical cyclogenesis and its role for the evolution of a wave critical layer.

The impact of the coherent structures on the mixing process was quantified in terms of time- and space-dependent mixing rates, with the spatial dependence displayed as a function of shear-strength as well as a function of the (average) radius of shear-lines. Overall, the moving-frame approach used in this chapter provides time-dependent mixing rates that isolate mixing events occurring in particular time windows.

The methods used here led to mixing profiles of similar structure as in [HS09], but with a moving time frame and with fast convergence in Lagrangian fields integrated over short times. The S-field provided a natural choice of contours for varying initial time that allowed to quantify mixing by determining transport across them.

Future work will address the impact of hyperbolicity in the presence of high shear in a three-dimensional setting, where planar shear and movement orthogonal to the shear are separated using suitable extensions of the fields introduced in this chapter. These techniques will be applied to a realistic, three-dimensional hurricane model that has both shearing and hyperbolic components governing the mixing processes. The focus of this work will be rather different from that of a recent chapter by [SH09], who studied mixing in a three-dimensional hurricane model by computing Lagrangian quantities along a slow manifold.

Chapter 6

A 3D Lagrangian hurricane eye-eyewall computation

6.1 Summary

The computation of a hurricane eyewall is necessary for determining mixing between the eyewall and the neighboring eye and environment regions. We define a Lagrangian eyewall region by computing the Lagrangian structures of hyperbolic stability that distinguish the eyewall from surrounding regions. The methods used guarantee the stability and continuity of the eyewall for time-dependent velocity fields. As an added benefit of our methods, fast convergence gives the opportunity to utilize the methods in real-time simulations. Exact location of Lagrangian coherent structures is accomplished through a ridge extraction algorithm, which is efficient for locating the ridges found in this model. A complete construction of 3D coherent structures is accomplished by overlaying horizontally continuous ridge-curves on z-levels.

6.2 Background and overview

A hurricane eye may be defined in terms of a variety of physical quantities. Material residing in the eye has low pressure, high potential temperature, and low relative humidity compared to material travelling through the eyewall. Lower wind speeds relative to the eyewall are also characteristic of the eye. While all of these features differentiate the two regions, properties such as wind speed may not be continuous over space and time. A continuous eye-eyewall definition is necessary for determining transport between the regions.

Transport of fluid within the hurricane core is believed to have significant impact on intensity [**?**, MBAB06], see also Chapter 4. Particularly important is the movement of fluid across the eye-eyewall and eyewall-environment boundaries [SMZ05, Bra02]. Accurately quantifying mixing in these regions requires the definition of boundaries. This study focuses on the definition, extraction, and stability of a Lagrangian eye-eyewall interface (LEEI), as a time-dependent set of manifolds determined from the velocity field.

Defining boundaries from Eulerian quantities is useful for visualization of instantaneous structures within a hurricane. However, time-dependence of a velocity field makes it possible that particle trajectories diverge from instantaneous structures and cross Eulerian boundaries. In contrast, Lagrangian methods are based on following trajectories, and reveal structures which are impenetrable to trajectories over short to intermediate integration times. The frame independence of these methods makes them applicable to rotational flows [Hal05].

In Lagrangian methods, invariant structures are computed based on the separation of trajectories, and regions of high separation are established as invariant manifolds. Finite-time Lyapunov exponents (FTLE's) have been the basis for many recent Lagrangian studies in fluid mixing, see e.g. [HY00, Hal00, HP97, Hal02]. For divergent atmospheric flows, finite-size Lyapunov exponents (FSLE's) have some advantages over FTLE's [JL01, KL02], however, neither of these methods accounts for separation due to shear, although hyperbolic stability of trajectories can be established through eigenvalues of the strain tensor. Because they are measures of total separation, FTLE's and FSLE's hold no relation to Eulerian features in the flow. An orthogonal version of FTLE's in the 2D nondivergent setting, which differentiates hyperbolic separation from shear and accounts for Eulerian features, has been introduced in [HI03], and was used in Chapter 5 to diagnose hyperbolicity superimposed on shear in a 2D nondivergent barotropic hurricane model. In Chapter 5 it was also demonstrated that calculations based on this method show faster convergence than calculations based on FTLE's. In this study, we establish and apply the 3D extension of the orthogonal FTLE-method, and describe the resulting stability types arising from the 3D transformed variational system. Finding vertically continuous hyperbolic structures over a variety of initial times leads to a definition of the eye-eyewall interface that is consistent with the actual trajectory movement. In addition, we adapt a gradient climbing ridge extraction method to extract 3D surfaces from the Lagrangian scalar fields.

Lagrangian methods have only recently been applied in atmospheric studies. Joseph and Legras [JL01] have defined Lagrangian boundaries on the antarctic polar vortex, and Huber et al. [HMG01] studied relative dispersion in the troposphere. Recent studies have also applied Lagrangian techniques to hurricanes. Cram et al. [CPMB07] studied mixing in a 3D hurricane simulation through a trajectory analysis. Haller and Sapsis [SH09] computed a slow manifold to study attracting properties of inertial particles.

The chapter is organized as follows. In Section 6.3 we provide the solution to the 3D variational system, as well as a choice of coordinate frames for defining Lagrangian fields. A new ridge extraction algorithm, along with a method for extracting 3D maximal surfaces is outlined in Section 6.4. In Section 6.5 we present results obtained by applying the methods from Sections 6.3 and 6.4 to the 3D MM5 hurricane model. Conclusions and an outlook on future work are given in Section 6.6.

6.3 Model overview

The simulation used for this study is an adaptation of the fifth generation Penn State/NCAR mesoscale model (MM5) [Dud93, GDS95] used in the study of [NSM08]. An initially weak tropical storm strength axisymmetric vortex develops into a 3D asymmetric flow. Later, these asymetries disappear, and a mature tropical cyclone vortex emerges. The model physics used is a bulk-aerodynamic boundary-layer scheme, with a simple moisture scheme. Output wind fields are given on a triply-nested mesh, with data on the innermost mesh given on an equidistant xy grid with $dx = dy = 5\,\mathrm{km}$, and the z grid given in pressure coordinates. The temporal spacing is $dt = 15\,\mathrm{min}$.

Trajectories are computed using a fourth order Runge-Kutta scheme, with intermediate time steps of 1 min, and with no absolute integration tolerance.

The computations presented here were done during a mature cyclone phase near a model time of 62 hours.

For construction of a Lagrangian eyewall, we examine the solutions of the 3D variational system. The solutions show the interaction between separate subspaces, and differentiate types of particle separation, as well as the directions of separation. Since the solutions are computed along trajectories, the fields have a relationship with local flow features that the trajectories encounter. A result of incorporating the local features into a Lagrangian scalar field is faster convergence of the method than methods which only measure total separation.

6.4 Variational system and TNB coordinate frame

The Lagrangian velocity in 3D is defined in the same manner as in the 2D case, see [HI03] and Chapter 5. Given a velocity field

$$\mathbf{u}(\mathbf{x},t) = \begin{pmatrix} u(\mathbf{x},t) \\ v(\mathbf{x},t) \\ w(\mathbf{x},t) \end{pmatrix}, \quad \mathbf{x} \in \mathbb{R}^3, \tag{6.1}$$

and a trajectory $\mathbf{x}(t)$ satisfying

$$\dot{\mathbf{x}} = \mathbf{u}(\mathbf{x},t), \tag{6.2}$$

small perturbations $\boldsymbol{\xi}(t)$ of the trajectory are solutions of the variational system

$$\dot{\boldsymbol{\xi}} = \nabla\mathbf{u}(\mathbf{x}(t),t)\boldsymbol{\xi}. \tag{6.3}$$

The Lagrangian velocity direction is given by the unit tangent vector

$$\mathbf{t} = \frac{\mathbf{u}}{|\mathbf{u}|}, \tag{6.4}$$

evaluated along trajectories. The separation of trajectories orthogonal to the Lagrangian velocity is measured by the rate of separation in directions in the normal plane of $\mathbf{t}$. If $\mathbf{n}$ is a unit vector normal to the Lagrangian velocity, that is, $|\mathbf{n}| = 1$ and $\mathbf{t}^*\mathbf{n} = 0$ (we use an asterik to denote a transposed vector or matrix), an orthonormal basis in the normal plane is provided by $\mathbf{n}$ and

$$\mathbf{b} = \mathbf{t} \times \mathbf{n}. \tag{6.5}$$

This includes the special case where $\mathbf{n}$ is chosen as principal normal pointing in the direction of the curvature center.

In our transformation of the variational system (6.3), we first assume a given $(\mathbf{t},\mathbf{n},\mathbf{b})$ (TNB) coordinate frame in which $\mathbf{n}(\mathbf{x},t)$ varies differentiably with $(\mathbf{x},t)$, but is not specified otherwise. We refer to $\mathbf{n}$ as normal vector and to $\mathbf{b}$ as binormal vector. Two special choices for $\mathbf{n}$ will be discussed in some detail in Section 6.7.

6.5 Transformation of the variational system

Given a TNB-frame as described in Section 6.4, a moving frame of reference for (6.3) is introduced along a trajectory by setting

$$\boldsymbol{\xi} = T(\mathbf{x}(t),t)\boldsymbol{\eta}, \tag{6.6}$$

where the columns of T are the unit vectors $\mathbf{t}, \mathbf{n}, \mathbf{b}$,

$$T(\mathbf{x}, t) = [\mathbf{t}(\mathbf{x}, t), \mathbf{n}(\mathbf{x}, t), \mathbf{b}(\mathbf{x}, t)]. \tag{6.7}$$

Since T has orthonormal columns, $T^{-1} = T^*$, and the rows of T^{-1} are the unit row vectors $\mathbf{t}^*, \mathbf{n}^*, \mathbf{b}^*$. The transformed system for $\boldsymbol{\eta}$ has the form

$$\dot{\boldsymbol{\eta}} = [A(\mathbf{x}(t), t) + B(\mathbf{x}(t), t)]\boldsymbol{\eta}, \tag{6.8}$$

where $A(\mathbf{x}, t) = T^*(\nabla \mathbf{u})T - T^*(T_{\mathbf{x}}\dot{\mathbf{x}})$ with

$$T_{\mathbf{x}}\dot{\mathbf{x}} = \big[(\nabla \mathbf{u})\mathbf{t} - [\mathbf{t}^*(\nabla \mathbf{u})\mathbf{t}]\mathbf{t}, (\nabla \mathbf{n})\mathbf{u}, (\nabla \mathbf{b})\mathbf{u}\big],$$

and $B(\mathbf{x}, t) = -[\mathbf{b}_1, T^*\mathbf{n}_t, T^*\mathbf{b}_t]$ with $\mathbf{b}_1 = (1/|\mathbf{u}|)\,[0, \mathbf{n}^*\mathbf{u}_t, \mathbf{b}^*\mathbf{u}_t]^*$ contains all terms of the transformed matrix that depend on the time derivatives of $\mathbf{u}, \mathbf{n}, \mathbf{b}$ (indicated by the subscript t), thus B vanishes in the case of autonomous velocity fields. Combining the two terms of which A is composed yields $A = [\mathbf{a}_1, T^*\mathbf{a}_2, T^*\mathbf{a}_3]$, where

$$\begin{aligned}
\mathbf{a}_1 &= [\mathbf{t}^*(\nabla \mathbf{u})\mathbf{t}, 0, 0]^*, \\
\mathbf{a}_2 &= (\nabla \mathbf{u})\mathbf{n} - (\nabla \mathbf{n})\mathbf{u}, \\
\mathbf{a}_3 &= (\nabla \mathbf{u})\mathbf{b} - (\nabla \mathbf{b})\mathbf{u}.
\end{aligned}$$

As in the 2D case, the $(1, 1)$-component of A is the parallel strain rate, $A_{11} = S_p = \mathbf{t}^*(\nabla \mathbf{u})_s\mathbf{t}$. Here, for any square matrix M, the symmetric part is denoted by M_s and the antisymmetric part by M_a, $M_s = (M + M^*)/2$ and $M_a = (M - M^*)/2$. In Cartesian coordinates, the parallel strain rate is given by

$$\begin{aligned}
S_p = \frac{1}{|\mathbf{u}|^2}\Big(&u^2u_x + v^2v_y + w^2w_y + uv(u_y + v_x) \\
&+ uw(u_z + w_x) + vw(v_z + w_y)\Big).
\end{aligned} \tag{6.9}$$

The terms in A and B can be simplified using the orthonormality of the TNB-frame. For example, $|\mathbf{n}| = 1$ gives $\mathbf{n}^*(\nabla \mathbf{n}) = \mathbf{0}$ and $\mathbf{n}^*\mathbf{n}_t = 0$, and $\mathbf{n}^*\mathbf{u} = 0$ implies $\mathbf{n}^*(\nabla \mathbf{u}) + \mathbf{u}^*(\nabla \mathbf{n}) = \mathbf{0}$ and $\mathbf{n}^*\mathbf{u}_t + \mathbf{u}^*\mathbf{n}_t = 0$. Exploiting these and analogous relations shows that B is antisymmetric,

$$B\boldsymbol{\eta} = \boldsymbol{\Omega} \times \boldsymbol{\eta}, \tag{6.10}$$

with

$$\boldsymbol{\Omega} = [\mathbf{b}^*\mathbf{n}_t, -\mathbf{t}^*\mathbf{b}_t, \mathbf{t}^*\mathbf{n}_t]^*. \tag{6.11}$$

Similarly, the terms in A can be simplified to

$$A(\mathbf{x},t) = \begin{pmatrix} S_p & 2\mathbf{t}^*(\nabla\mathbf{u})_s\mathbf{n} & 2\mathbf{t}^*(\nabla\mathbf{u})_s\mathbf{b} \\ 0 & S_n & -|\mathbf{u}|\mathbf{n}^*(\nabla\times\mathbf{n}) \\ 0 & |\mathbf{u}|\mathbf{b}^*(\nabla\times\mathbf{b}) & S_b \end{pmatrix}, \tag{6.12}$$

where $S_n = \mathbf{n}^*(\nabla\mathbf{u})_s\mathbf{n}$ and $S_b = \mathbf{b}^*(\nabla\mathbf{u})_s\mathbf{b}$ are the strain rates in the directions of $\mathbf{n}$ and $\mathbf{b}$, respectively.

As in our study of the 2D case in Chapter 5, we assume that the time derivatives are small and can be neglected. Thus we use the following approximation of the transformed variational system,

$$\dot{\boldsymbol{\eta}} = A(\mathbf{x}(t),t)\boldsymbol{\eta}. \tag{6.13}$$

6.6 Transformation to upper triangular form

In contrast to the 2D case, the matrix A is not upper triangular. To obtain upper triangular form we apply a time-dependent orthogonal transformation in the normal plane. The normal plane component, $\boldsymbol{\eta}^\perp = (\eta_2,\eta_3)^*$, satisfies $\dot{\boldsymbol{\eta}}^\perp = A^\perp\boldsymbol{\eta}$ with

$$A^\perp = \begin{pmatrix} A_{22} & A_{23} \\ A_{32} & A_{33} \end{pmatrix}. \tag{6.14}$$

Let $\phi(t)$ be a solution to the differential equation

$$\dot{\phi} = \frac{1}{2}(A_{33}-A_{22})\sin 2\phi + A_{23}\sin^2\phi - A_{32}\cos^2\phi, \tag{6.15}$$

and $R(\phi)$ the rotation matrix

$$R(\phi) = \begin{pmatrix} \cos\phi & \sin\phi \\ -\sin\phi & \cos\phi \end{pmatrix}. \tag{6.16}$$

The transformation $\boldsymbol{\eta}^\perp = R(\phi(t))\widetilde{\boldsymbol{\eta}}^\perp$ transforms the normal plane system to

$$\dot{\widetilde{\boldsymbol{\eta}}}^\perp = \widetilde{A}^\perp\widetilde{\boldsymbol{\eta}}^\perp, \tag{6.17}$$

where

$$\begin{aligned}
\widetilde{A}_{22} &= A_{22}\cos^2\phi + A_{33}\sin^2\phi \\
&\quad -\tfrac{1}{2}(A_{23}+A_{32})\sin 2\phi, \\
\widetilde{A}_{33} &= A_{22}\sin^2\phi + A_{33}\cos^2\phi \\
&\quad +\tfrac{1}{2}(A_{23}+A_{32})\sin 2\phi, \\
\widetilde{A}_{23} &= (A_{22}-A_{33})\sin 2\phi + (A_{23}+A_{32})\cos 2\phi, \\
\widetilde{A}_{32} &= 0,
\end{aligned} \tag{6.18}$$

Thus, dropping the tilde, we may assume that A in (6.13) has the form

$$A(\mathbf{x}(t),t) = \begin{pmatrix} A_{11} & A_{12} & A_{13} \\ 0 & A_{22} & A_{23} \\ 0 & 0 & A_{33} \end{pmatrix}, \tag{6.19}$$

and the transformed variational system can be solved by direct integration.

For any TNB-frame, the normal plane components (η_2, η_3) are decoupled from the tangential component η_1, indicating that hyperbolic separation can be determined from the growth of perturbations aligned with the η_2 and η_3 subspaces. The additional decoupling in the normal plane means that there is a distinguished normal direction such that deformations in the associated binormal direction, measured by $\eta_3(t)$, are decoupled from deformations in the normal direction, measured by $\eta_2(t)$.

The fundamental matrix for the system (6.13) with A given by (6.19) is found by direct integration as

$$\Psi(t,t_0) = \begin{pmatrix} \Psi_{11}(t,t_0) & \Psi_{12}(t,t_0) & \Psi_{13}(t,t_0) \\ 0 & \Psi_{22}(t,t_0) & \Psi_{23}(t,t_0) \\ 0 & 0 & \Psi_{33}(t,t_0) \end{pmatrix}, \tag{6.20}$$

where the diagonal elements can be written as

$$\Psi_{ii}(t,t_0) = \exp\big(\int_{t_0}^{t} A_{ii}(\tau)\,d\tau\big),$$

and the off-diagonal elements as

$$\begin{aligned}
\Psi_{12} &= \textstyle\int_{t_0}^{t} \exp\left(\int_s^t A_{11}(\tau)\,d\tau\right) \\
&\quad \exp\left(\int_{t_0}^{s} A_{22}(\tau)\,d\tau\right) A_{12}(s)\,ds, \\
\Psi_{23} &= \textstyle\int_{t_0}^{t} \exp\left(\int_s^t A_{22}(\tau)\,d\tau\right) \\
&\quad \exp\left(\int_{t_0}^{s} A_{33}(\tau)\,d\tau\right) A_{23}(s)\,ds, \\
\Psi_{13} &= \textstyle\int_{t_0}^{t} \exp\left(\int_s^t A_{11}(\tau)\,d\tau\right) \Big[\Psi_{23}(s,t_0)A_{12}(s) \\
&\qquad + \exp\left(\int_{t_0}^{s} A_{33}(\tau)\,d\tau\right) A_{13}(s)\Big]\,ds.
\end{aligned} \tag{6.21}$$

6.7 Special choices for the TNB frame

The equation (6.12) for $A(\mathbf{x}, t)$ holds for any choice of the unit vector $\mathbf{n}(\mathbf{x}, t)$ in the normal plane. We discuss here two special cases in some detail: The case where $\mathbf{n}$ is chosen as principal normal, and the case where $\mathbf{n}$ is located in the (x, y)-plane. In our numerical calculation for the MM5-data we used the second choice.

Principal normal

Here we consider a local trajectory $\mathbf{y}(\tau, \mathbf{x}, t)$ passing at $\tau = 0$ through the point $(\mathbf{x}, t)$, that is, $\mathbf{y}_\tau = \mathbf{u}(\mathbf{y}, \tau)$ and $\mathbf{y}(0, \mathbf{x}, t) = \mathbf{x}$. The principal normal is found from the quadratic expansion of $\mathbf{y}$ with respect to τ,

$$\mathbf{y} = \mathbf{x} + \tau\mathbf{u} + \frac{1}{2}\tau^2\mathbf{w} + O(\tau^3),$$

where $\mathbf{w} = (\nabla\mathbf{u})\mathbf{u} + \mathbf{u}_t$, and $\mathbf{u}$ and derivatives of $\mathbf{u}$ are evaluated at $(\mathbf{x}, t)$. Converting this to arclength, $ds = |\mathbf{y}_\tau|\, d\tau$, gives

$$\mathbf{y} = \mathbf{x} + s\mathbf{t} + \frac{1}{2}s^2\big(\mathbf{w} - [\mathbf{t}^*\mathbf{w}]\mathbf{t}\big)/|\mathbf{u}|^2 + O(s^3).$$

The principal normal, which we denote here also by $\mathbf{n}(\mathbf{x}, t)$, is the unit vector in the direction of the coefficient vector of $s^2/2$, and the square of the curvature, κ, at $\tau = 0$ is the squared length of this vector. In terms of $\mathbf{u}$, these quantities and the associated binormal $\mathbf{b}(\mathbf{x}, t)$ are given by

$$\begin{aligned}
\kappa^2 &= \frac{1}{|\mathbf{u}|^6}\,|\mathbf{u} \times \mathbf{w}|^2, \\
\mathbf{n} &= \frac{1}{\kappa|\mathbf{u}|^4}\,\mathbf{u} \times (\mathbf{w} \times \mathbf{u}), \\
\mathbf{b} &= \frac{1}{\kappa|\mathbf{u}|^3}\,\mathbf{u} \times \mathbf{w}.
\end{aligned} \tag{6.22}$$

With time-derivatives again neglected, these terms can be expressed through $\nabla\mathbf{u}$ and $\mathbf{t} = \mathbf{u}/|\mathbf{u}|$ as

$$\kappa^2 = \frac{1}{|\mathbf{u}|^2}\big(|(\nabla\mathbf{u})\mathbf{t}|^2 - [\mathbf{t}^*(\nabla\mathbf{u})\mathbf{t}]^2\big),$$

$$\mathbf{n} = \frac{1}{\kappa|\mathbf{u}|}\big((\nabla\mathbf{u})\mathbf{t} - [\mathbf{t}^*(\nabla\mathbf{u})\mathbf{t}]\mathbf{t}\big), \tag{6.23}$$

$$\mathbf{b} = \frac{1}{\kappa|\mathbf{u}|}\,\mathbf{t} \times (\nabla\mathbf{u})\mathbf{t}. \tag{6.24}$$

For a 3D hurricane, the motion in the eyewall can be described as helical, with rotational and vertical components. In Figure 6.1 we show the z-component of the binormal on trajectories integrated for 1 hour and seeded on (x, y)-grids at two different z-levels. As is apparent from this figure, the binormal direction is generally aligned vertically upward, which means that the principal normal is (approximately) aligned in the (x, y)-plane.

In Figure 6.2(a) an updraft trajectory and an environment trajectory are displayed along with the principal normal and the binormal, demonstrating the approximately vertical orientation of the binormal direction. The counterclockwise rotation implies that the principal normal direction is generally oriented inward, as is apparent from Figure 6.2(b), where the (x, y)-projections of the tangent and the principal normal along the trajectories shown in Figure 6.2(a) are depicted.

Using (6.23), the components A_{12}, A_{13}, A_{22}, and A_{33} in (6.12) can be written in terms of $\nabla\mathbf{u}$ and $\mathbf{t}$ in the form,

$$
\begin{aligned}
A_{12} &= \frac{1}{\kappa|\mathbf{u}|}\left(|(\nabla\mathbf{u})\mathbf{t}|^2 + \mathbf{t}^*(\nabla\mathbf{u})^2\mathbf{t} - 2[\mathbf{t}^*(\nabla\mathbf{u})\mathbf{t}]^2\right),\\
A_{13} &= \frac{1}{\kappa^2|\mathbf{u}|}\det[\mathbf{t}, (\nabla\mathbf{u})\mathbf{t}, (\nabla\mathbf{u})^*\mathbf{t}],\\
A_{22} &= \frac{1}{\kappa^2|\mathbf{u}|^2}\Big(\mathbf{t}^*(\nabla\mathbf{u})^*(\nabla\mathbf{u})_s(\nabla\mathbf{u})\mathbf{t} + [\mathbf{t}^*(\nabla\mathbf{u})\mathbf{t}]^3\\
&\qquad - [\mathbf{t}^*(\nabla\mathbf{u})\mathbf{t}][\mathbf{t}^*(\nabla\mathbf{u})^2\mathbf{t} + |(\nabla\mathbf{u})\mathbf{t}|^2]\Big),\\
A_{33} &= \frac{1}{\kappa^2|\mathbf{u}|^2}[\mathbf{t}\times(\nabla\mathbf{u})\mathbf{t}]^*(\nabla\mathbf{u})_s[\mathbf{t}\times(\nabla\mathbf{u})\mathbf{t}].
\end{aligned}
$$

The components A_{23} and A_{32} involve second derivatives of $\mathbf{u}$. For A_{32} we obtain

$$
A_{32} = \frac{|\mathbf{u}|\det[\mathbf{t}, (\mathbf{t}^*\nabla)\mathbf{u}, \mathcal{D}\mathbf{u}]}{[\mathbf{t}^*(\nabla\mathbf{u})\mathbf{t}]^2 - |(\mathbf{t}^*\nabla)\mathbf{u}|^2},
$$

where $\mathcal{D}$ is the second order differential operator,

$$
\begin{aligned}
\mathcal{D} = \frac{1}{|\mathbf{u}|^2}\Big(&u^2\partial_x^2 + 2uv\partial_x\partial_y + 2uw\partial_x\partial_z + v^2\partial_y^2\\
&+ 2vw\partial_y\partial_z + w^2\partial_z^2\Big).
\end{aligned}
$$

The component A_{23} can be written compactly in the form

$$
A_{23} = -\frac{|\mathbf{u}|}{|\mathbf{N}|^2}\mathbf{N}^*(\nabla\times\mathbf{N}),
$$

where $\mathbf{N} = (\nabla\mathbf{u})\mathbf{u} - A_{11}\mathbf{u}$. When written out explicitly, A_{23} becomes a complicated expression involving projections and derivatives of the vorticity.

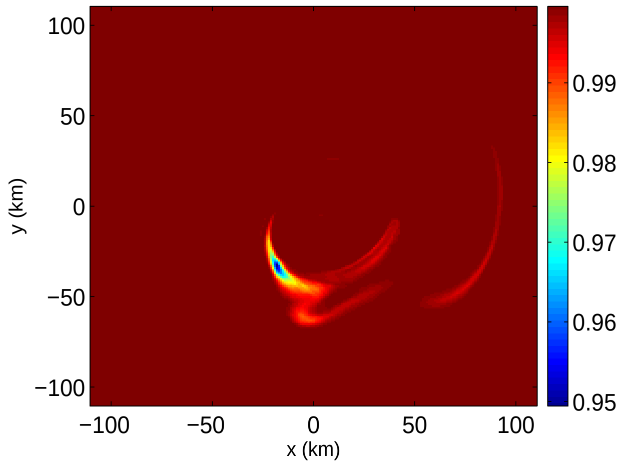

(a)

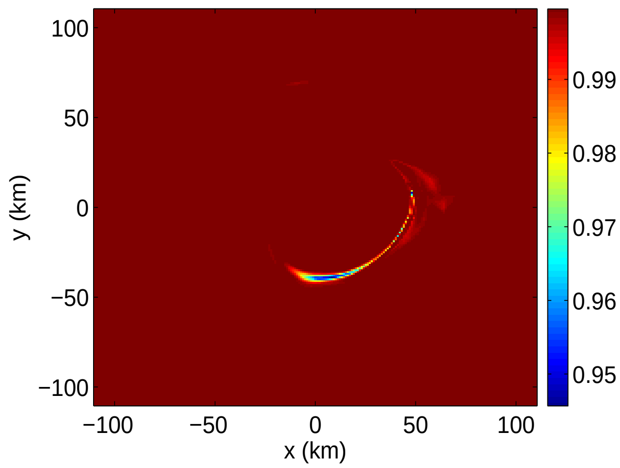

(b)

Figure 6.1: Binormal z-component on trajectories integrated 1 hr and seeded on (x, y)-grids at z-levels 500 m (a) and 3 km (b). Values near 1 show that the coordinate system is oriented with the binormal direction vertically upward.

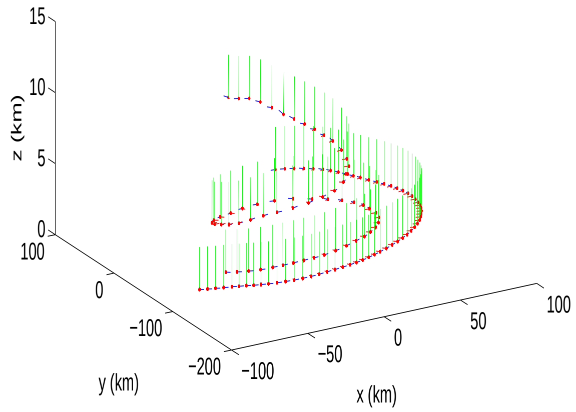

(a)

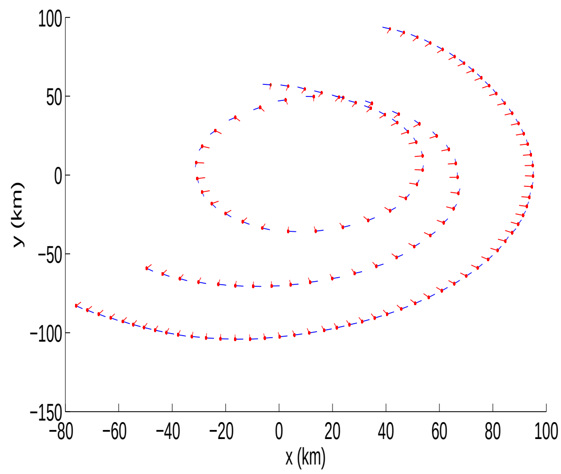

(b)

Figure 6.2: (a) Updraft and environment trajectories along with principal normal (oriented horizontally inward) and binormal (oriented vertically upwards). (b) (x, y)-projections of tangent and principal normal along the trajectories of (a).

6.7.1 Horizontally aligned normal vector

Another choice for the unit normal $\mathbf{n}$, which we used in our calculations for the MM5-model, is provided by

$$\mathbf{n} = \mathbf{u}_h^{\perp}/|\mathbf{u}_h|, \tag{6.25}$$

where $\mathbf{u}_h = (u, v, 0)^*$ is the horizontal component of the velocity, and $\mathbf{u}_h^{\perp} = (-v, u, 0)^*$. In this case the binormal is given by

$$\mathbf{b} = \frac{1}{|\mathbf{u}||\mathbf{u}_h|}\left(-uw, -vw, |\mathbf{u}_h|^2\right)^*, \tag{6.26}$$

and the entries A_{ij} with $i > 1$ in (6.12) become

$$\begin{aligned}
A_{12} &= \frac{1}{|\mathbf{u}||\mathbf{u}_h|}\Big\{(u^2 - v^2)(u_y + v_x) + 2uv(v_y - u_x) \\
&\qquad\qquad + uw(v_z + w_y) - vw(u_z + w_x)\Big\}, \\
A_{13} &= \frac{1}{|\mathbf{u}|^2|\mathbf{u}_h|}\Big\{(|\mathbf{u}_h|^2 - w^2)\big(v(v_z + w_y) \\
&\quad +u(u_z + w_x)\big) - 2w(u^2u_x + v^2v_y) \\
&\quad -2uvw(u_y + v_x)\Big\}, \\
A_{22} &= \frac{1}{|\mathbf{u}_h|^2}\Big\{u^2v_y + v^2u_x - uv(u_y + v_x)\Big\}, \\
A_{23} &= \frac{|\mathbf{u}|\left(uv_z - vu_z\right)}{|\mathbf{u}_h|^2}, \\
A_{32} &= \frac{1}{|\mathbf{u}||\mathbf{u}_h|^2}\Big\{2w\big(v^2v_x - u^2u_y + \\
&\quad uv(u_x - v_y)\big) + w^2(vu_z - uv_z) \\
&\quad +|\mathbf{u}_h|^2\big(uw_y - vw_x + w(u_y - v_x)\big)\Big\}, \\
A_{33} &= \frac{1}{|\mathbf{u}|^2|\mathbf{u}_h|^2}\Big\{w^2\big(u^2u_x + v^2v_y + uv(u_y + v_x)\big) \\
&\quad -|\mathbf{u}_h|^2w\big(u(u_z + w_x) + v(v_z + w_y)\big) \\
&\quad +|\mathbf{u}_h|^4w_z\Big\}.
\end{aligned}$$

6.8 3D Lagrangian measures

6.8.1 3D Shear

Shear in the 3D setting can be characterized by studying alignment of the subspaces along trajectories. The 3D variational system has three coupled solutions, all of which can be attributed to a type of shear. Following the 2D characterization of Haller [HI03], we look at the alignment of the η_2 and η_3 subspaces to the Lagrangian velocity. The angles between these subspaces to the η_1 subspace are the angles ϕ_2 and ϕ_3, defined by

$$\cot\phi_i = \frac{\Psi_{ii}}{\Psi_{1i}}, \quad i = 2, 3. \tag{6.27}$$

Shear in the (η_1, η_i) plane is determined by $|\cot\phi_i| \to \infty$. Under short integration times, regions of high shear are characterized by $\cot\phi_i$ being bounded away from zero. An orthogonal shear can be determined by the alignment of the binormal direction onto the normal plane by

$$\cot\phi^{\perp} = \frac{\Psi_{22}}{\Psi_{23}}, \tag{6.28}$$

which describes rotations of material elements aligned with the η_3 subspace onto the η_2 subspace.

Shearing is an important aspect of 3D hurricanes. The eye-eyewall boundary is an example of a region of vertical wind shear, with the normal vector to the Lagrangian velocity aligning with the Lagrangian velocity. The angle ϕ_2 is representative of this type of shear. The boundary-layer inflow and upper-level outflow are regions of horizontal wind shear, and can be represented by ϕ_3. Strong updrafts near strong rotation define shear for a hurricane as either $\cot\phi_2$ or $\cot\phi_3$ being bounded away from zero.

6.8.2 Hyperbolic manifolds

To interpret the stability of coherent structures from the hyperbolic fields, we look at the combinations of all hyperbolic and shear trajectory separation. If the model has a hyperbolic manifold, it must exist in a region with little shear, meaning material lines initially oriented with the η_2 and η_3 axes do not rotate onto the η_1 axis. A hyperbolic trajectory has stable and unstable manifolds, with one being 2D and the other 1D. Since the time-dependent manifold forms a set of solutions to the velocity field, we can assume that the η_1 subspace is contained in the manifold, and shows little expansion or contraction along trajectories. In general the manifold need not be oriented along either η_2 or η_3 axis. Instead the angle ϕ_i shows the amount of rotation of the η_i subspace onto the eigendirection of the manifold.

For the fields that we have computed, the rotation is small in the region where a maximal surface occurs, and the $\boldsymbol{\eta}$ coordinate system is already aligned with the maximal surface such that the surface lies (locally) in the $\eta_1 - \eta_3$ plane. Thus we conclude that the 2D manifold lies in the $\eta_1 - \eta_3$ plane, and the 1D manifold then lies along the η_2 axis. Since the η_3 subspace is contracting, an induced expansion occurs in the directon orthogonal to the 2D manifold. The 2D manifold is unstable, while the 1D manifold in the η_2 direction is stable. Since $\Psi_{11} \approx 1$, a maximal Ψ_{22} value is equivalent to a minimal Ψ_{33} value, due to small divergence along trajectories.

We note that the quantities $\frac{\log \Psi_{22}}{t-t_0}$ and $\frac{\log \Psi_{33}}{t-t_0}$ are the finite-time Lyapunov exponents in the directions of the η_2 and η_3 subspaces respectively. These would compare to the standard FTLE if the perturbation was aligned along the correct subspace, and there was no shear.

6.8.3 Comparison to FTLE's and instability time

The growth rate of line elements initially oriented in the directions of the various $\boldsymbol{\eta}$ subspaces is different from the growth rate obtained from FTLE computations, which measure total separation of neighboring trajectories. The growth captured in the FTLE field is the cumulative growth of perturbations which are initiated at initial conditions. In contrast, while the solutions of the (η_2, η_3)-system do not necessarily describe the total growth of perturbations, but rather the growth of a continuously reinitiated perturbation, they still give a diagnostic of the flow separation, which grow faster, and therefore converge faster, than FTLEs.

For trajectories seeded near a repelling hyperbolic material surface, trajectories nearest to the surface are expected to remain near the surface longer than trajectories initially further away from the surface, which are expected to diverge from the surface more quickly. The Ψ_{22} hyperbolic values for trajectories that remain near the material surface show positive A_{22} values for longer times than those that leave the material surface quickly (Figure 6.3). Trajectories that leave the hyperbolic repelling region do not necessarily maintain hyperbolic repelling stability, but may switch to neutral or hyperbolic attracting stability. For trajectories seeded near a ridge, however, continuous expansion/contraction ensures minimal/maximal hyperbolic values. In fact, trajectories remaining in hyperbolic repelling regions for the longest times do generally correspond to trajectories with the highest Lagrangian Ψ_{22} values (Figure 6.4).

We define the η_2-instability time as the amount of time that a trajectory resides in a region where the η_2 subspace is expanding ($A_{22} > 0$). It should be noted that there are initial conditions that show persistent hyperbolic repelling behavior by the η_2-instability time, yet have neutral (low Ψ_{22}) stability through integration of the variational system. Thus high

Ψ_{22} values are a stronger condition for expansion in the η_2 subspace. It should also be noted that the Ψ_{22} field shows narrower ridges than the η_2-instability time field, which suggests that shorter integration time is required to fully resolve the hyperbolic structures associated with Ψ_{22} than the structures associated with the η_2-instability time.

6.9 Extraction of coherent structures

The manifolds from the 3D variational system must be extracted to show the exact location of Lagrangian coherent structures (LCS's). The vertically oriented cylindrical nature of the manifolds leads to an approach of extracting the manifolds by taking slices on z-levels, and piecing the manifolds together. A main concern when extracting ridges is not only the visualization of surfaces, which has been done in many recent studies, but also the extraction of ridges as sets of ordered points. The extraction algorithm used here is based on the gradient climbing algorithms used by Shadden et al. [SLM05] and Mathur et al. [MHP+07], but starts with a small number of points. The manifolds are then grown through the gradient dynamical system adapting a manifold growing algorithm by Mancho et al. [MSWI03].

The initial ridge segment is chosen by taking a maximal point on a ridge. By choosing the maximum value of the scalar field, the algorithm is automated in the choice of initial conditions.

Gradient climbing Given a 2D scalar field $\sigma(\mathbf{x})$, initial points evolve towards a ridge of σ under the flow of the gradient dynamical system [SLM05],

$$\frac{d\mathbf{x}}{ds} = \nabla\sigma(\mathbf{x}). \tag{6.29}$$

A disadvantage of gradient climbing is that points are eventually attracted to the maximal values of the ridges, or in the case of uneven ridges, the spikes in the ridges. This clustering has been avoided in [MHP+07] by switching to a Hessian system when a point is close enough to a ridge point. For an application of this method to atmospheric data, see [TMH+09]. Our approach is to extend the ridge along the direction of secondary curvature derived from the Hessian matrix.

The ridge points may still extend beyond the actual ridge using this ridge extension. In the event that this occurs, end points from the ridge are removed if the scalar field value

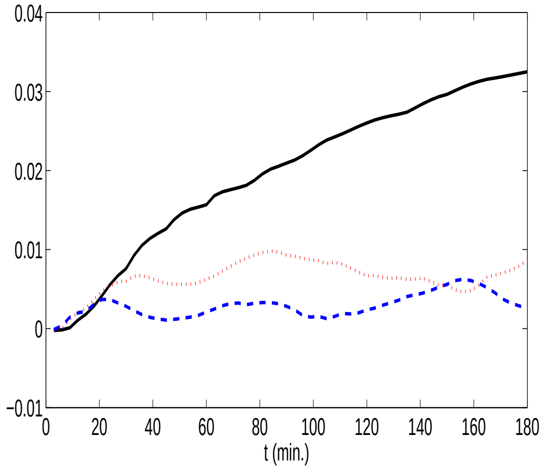

(a)

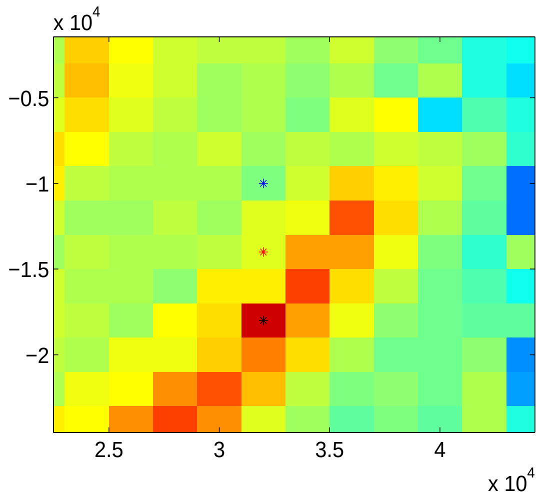

(b)

Figure 6.3: (a) Normal hyperbolic component $\int A_{22}dt$ as function of integration time for three trajectories. (b) Ψ_{22}-field for integration time 1 hr and initial locations of the trajectories depicted in (a), marking their proximity to the Ψ_{22} ridge.

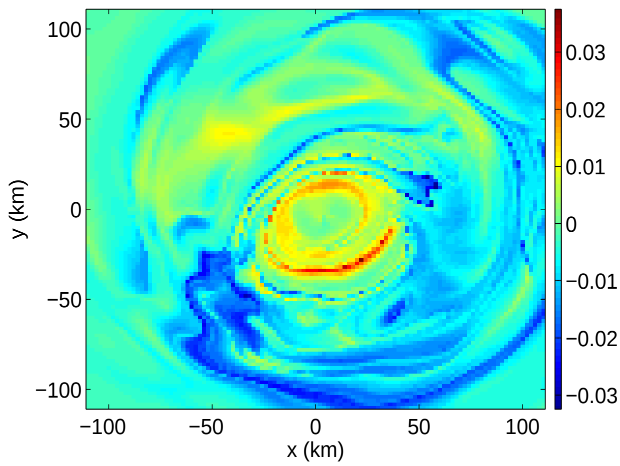

(a)

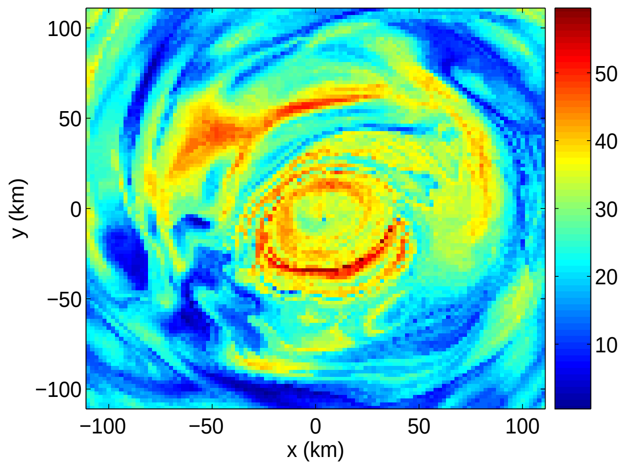

(b)

Figure 6.4: (a) Ψ_{22} and (b) instability time integrated for 3 hrs at initial time 62 hrs. Maxima of Ψ_{22} occur in regions that are persistently hyperbolic.

at the endpoint is greater than a parameter ρ. Gaps in the ridges may develop, making it necessary to insert additional points. For the ridges extracted from the scalar fields for the MM5 model, we use a distance criterion, adding additional points when the distance between two neighboring points becomes larger than a fixed parameter δ. Other criteria are given in [MSWI03], including methods that take into account the curvature of the ridge curve. In our case, the distance criterion was sufficient, although likely not optimal. To avoid the clustering, we use a redistribution of points along the ridge, similar to the manifold computation algorithm of [MSWI03]. We use only a distance parametrization, and do not attempt to introduce a parameter measuring curvature, although for ridges with high curvature, such a parameter may lead to more accurate results.

Our algorithm for the ridge extraction can be summarized as follows:

Algorithm

1. Choose initial condition $\mathbf{x}_0 = [\mathbf{x}^1, \mathbf{x}^2, ..., \mathbf{x}^{n-1}, \mathbf{x}^n]$.

   Continue until $\sum_{i=1}^{n-1} |\nabla\sigma(\mathbf{x}^1)||\mathbf{x}^{i+1} - \mathbf{x}^i| < \epsilon$:

2. Advance ridge segment $\mathbf{x}_0$ by (6.29).
3. Add initial and end points, $\mathbf{x}_0 \leftarrow [\mathbf{x}^{1'}, \mathbf{x}_0, \mathbf{x}^{n'}]$.
4. Advance ridge further using gradient climbing.
5. Remove endpoints $\mathbf{x}^{1'}$, $\mathbf{x}^{n'}$ if $\sigma(\mathbf{x}^{1'}) > \rho$ or $\sigma(\mathbf{x}^{n'}) > \rho$, respectively.
6. Insert point between $\mathbf{x}^i$ and $\mathbf{x}^{i+1}$ if $\|\mathbf{x}^i - \mathbf{x}^{i+1}\| > \delta$.
7. Redistribute points to equal spacing.
8. Make current ridge segment the next initial condition and go to 3.

6.10 Results

The solutions to the transformed variational system (6.13) are easily computed when the principal normal and binormal directions are well defined. Since we are studying the motion in and near a hurricane eyewall, most trajectories take helical paths, and the horizontal alignment described in Section 6.7.1 is a convenient choice for the normal vector $\mathbf{n}$. After computing the orthogonal transformation described in Section 6.6 (using $\phi(t_0) = 0$), the matrix A becomes upper triangular and the components Ψ_{ij} in (6.20)-(6.21) are computed by direct integration.

The fields Ψ_{22} and Ψ_{33} are the hyperbolic components of mixing, and the shear fields are the Ψ_{12} and Ψ_{13} components. In Figure 6.5 we show radial profiles of the Lagrangian fields Ψ_{22} and Ψ_{12} in comparison to radial profiles of the tangential and updraft winds. The eyewall updraft region is visible as the region of high updraft winds from 40-80 km, which is dominant only at certain azimuths. Tangential winds are also high in this region. The hyperbolic Ψ_{22} component shows maxima near 40 and 80 km, with less η_2 hyperbolic behavior in the region of strong updraft. The hyperbolic structures at these radii repel trajectories into the updraft jet, which is close to a minimum of Ψ_{22} at 60 km, just outside the radius of maximum tangential winds. The inner hyperbolic structure also repels trajectories inward to the eye, but these trajectories show only a weak rotational motion. A minimum of Ψ_{33} at the same location shows the contraction of nearby trajectories as they descend in the low pressure eye, or are elevated in the updraft. Maximal shear occurs just inside the outer hyperbolic maxima, and outside of the radius of maximum winds.

We define the Lagrangian eye-eyewall interface (LEEI) as the LCS corresponding to the inner ring of hyperbolic separation determined by the ridge surface of Ψ_{22}. The region has little shear, so the structure is purely hyperbolic, and therefore invariant. Computing the LEEI in the (x, y) plane at a given altitude shows that the structure forms an almost closed ring, allowing transport in or out through the gap in the ring, as shown in Figure 6.6. The gap is marked by minimal Ψ_{22} values, which may indicate a contracting region (jet) transporting material between the eye and eyewall. The break in the LEEI occurs at a similar azimuth as a region of high updraft winds, see Figure 6.10. Vertical coherence of the LEEI can be seen by computing the fields on additional z-levels, shown at higher levels in Figures 6.7, 6.8, and 6.9. In Figures 6.6-6.9, we show $\log \Psi_{22}$ and $\log \Psi_{33}$ where negative values correspond to contraction and positive values to expansion.

A surface of high shear is located just outside of the radius of maximal winds, visible as ridges of ϕ_2, which is the angle of rotation of the η_2 subspace onto the η_1 subspace, see Figures 6.6-6.9 (a). Trajectories in the LEEI show almost no rotation, while trajectories outside the LEEI show rotation of nearly $\pi/2$, so material lines rotate completely onto the η_1 subspace. The shear is mostly in the η_2 subspace, and the ϕ_2 field shows an almost closed

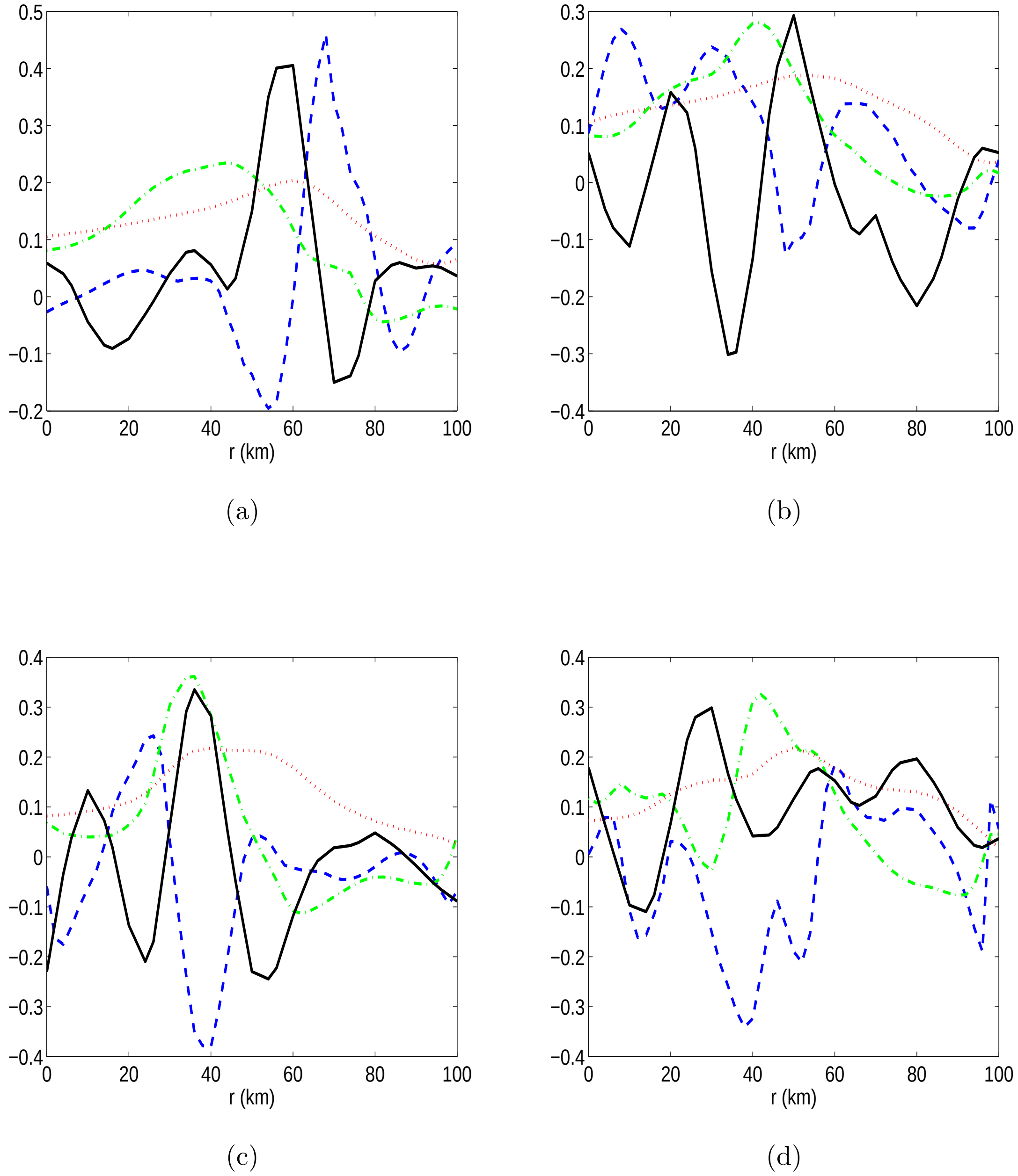

Figure 6.5: Radial profile of normalized fields Ψ_{22} (blue) and Ψ_{12} (green), tangential winds (red), and updraft winds (black) at 1 km (a), 5 km (b), 10 km (c), and 14 km (d) altitude, initial time 250 min, and azimuth angle 0^o. The integration time for the Lagrangian fields is 1 hr.

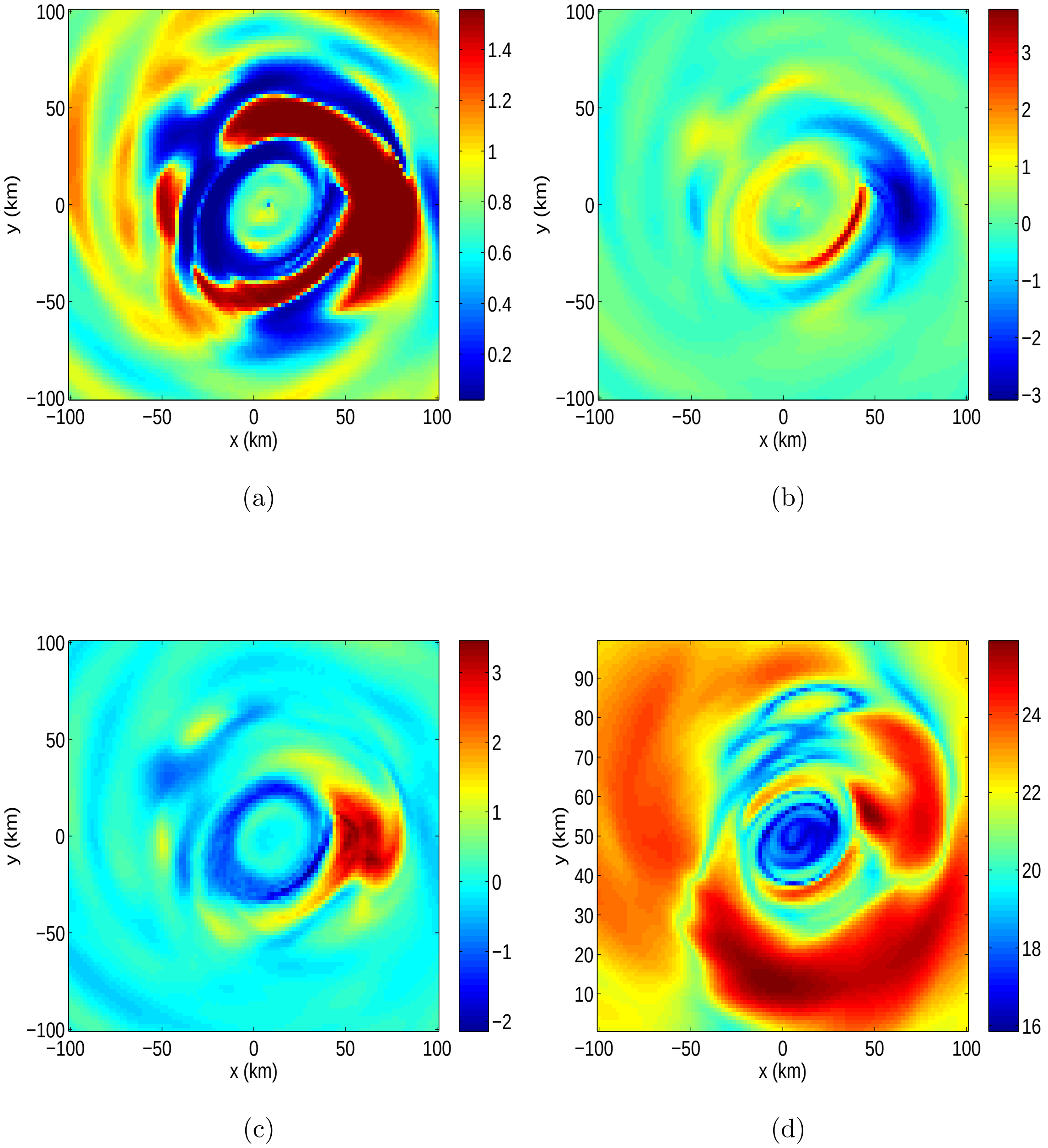

Figure 6.6: ϕ_2 (a), $\log \Psi_{22}$ (b), $\log \Psi_{33}$ (c), and FTLE (d) fields at z-level 1 km, initial time 62.5 hours, and integration time 1 h.

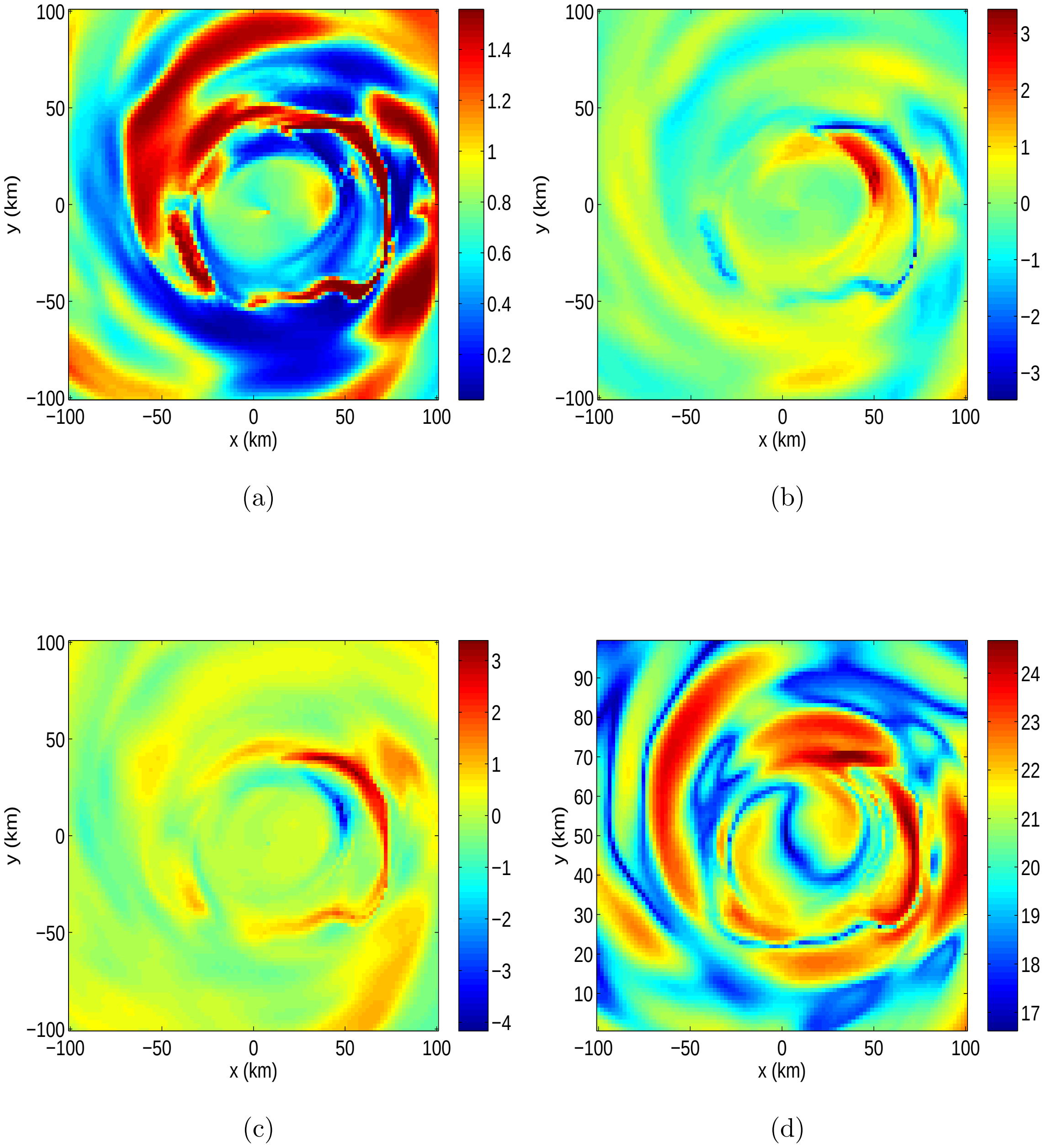

Figure 6.7: ϕ_2 (a), $\log \Psi_{22}$ (b), $\log \Psi_{33}$ (c), and FTLE (d) fields at z-level 5 km, initial time slice 62.5 hours, and integration time 1 h.

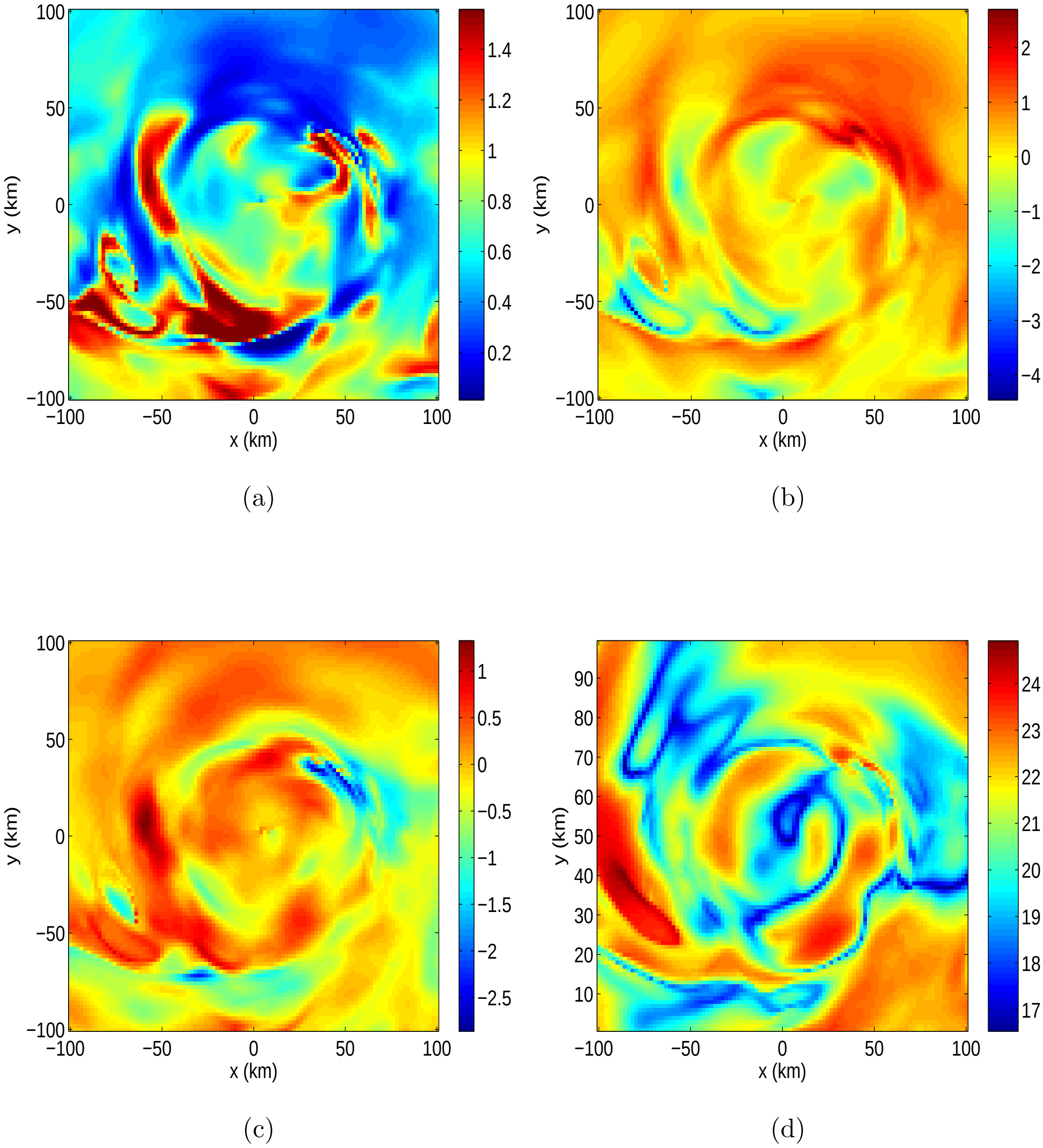

Figure 6.8: ϕ_2 (a), $\log \Psi_{22}$ (b), $\log \Psi_{33}$ (c), and FTLE (d) fields at z-level 10 km, initial time 62.5 hours, and integration time 1 h.

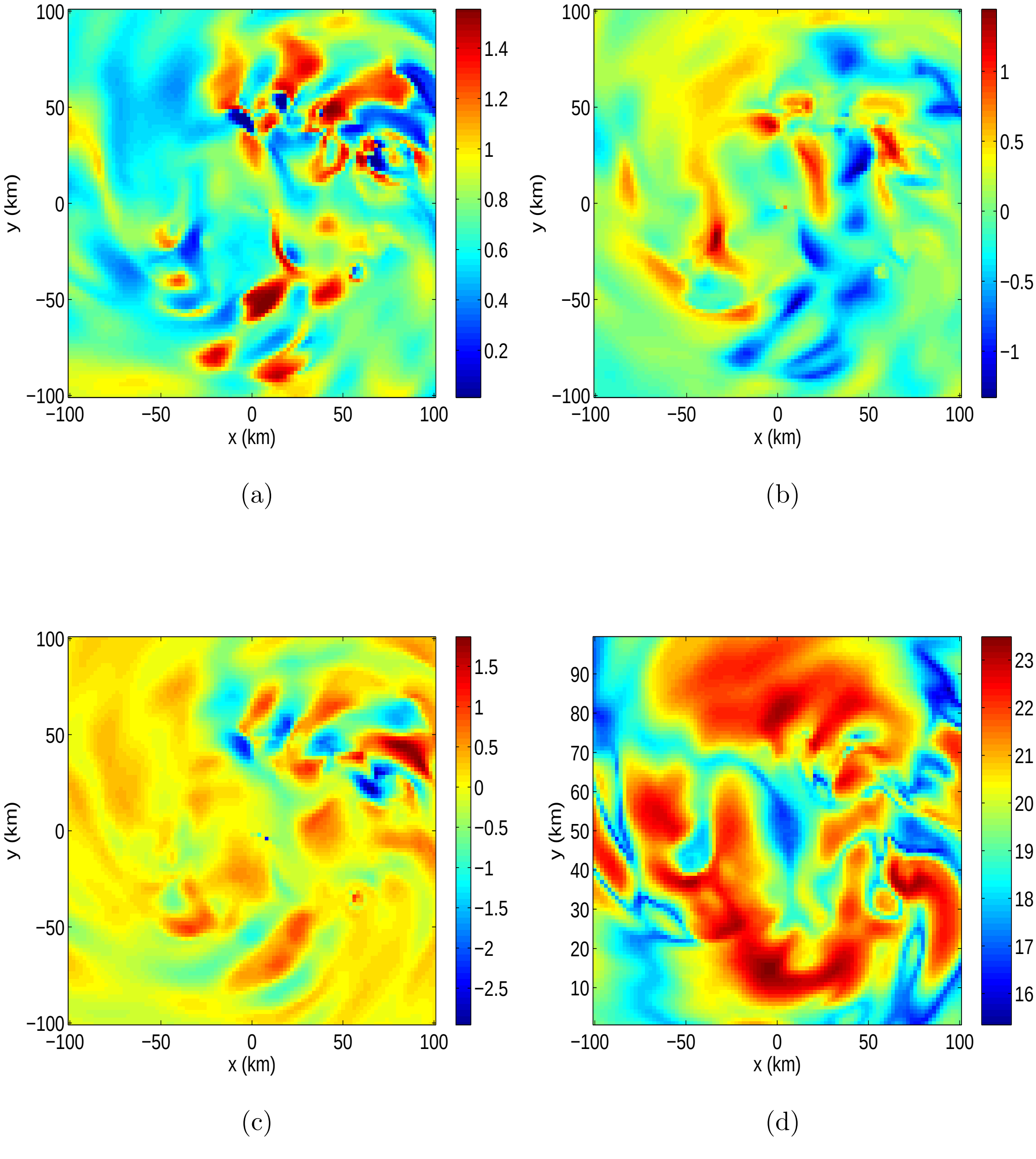

Figure 6.9: ϕ_{12} (a), $\log \Psi_{22}$ (b), $\log \Psi_{33}$ (c), and FTLE (d) fields at z-level 14 km, initial time 62.5 hours, and integration time 1 h.

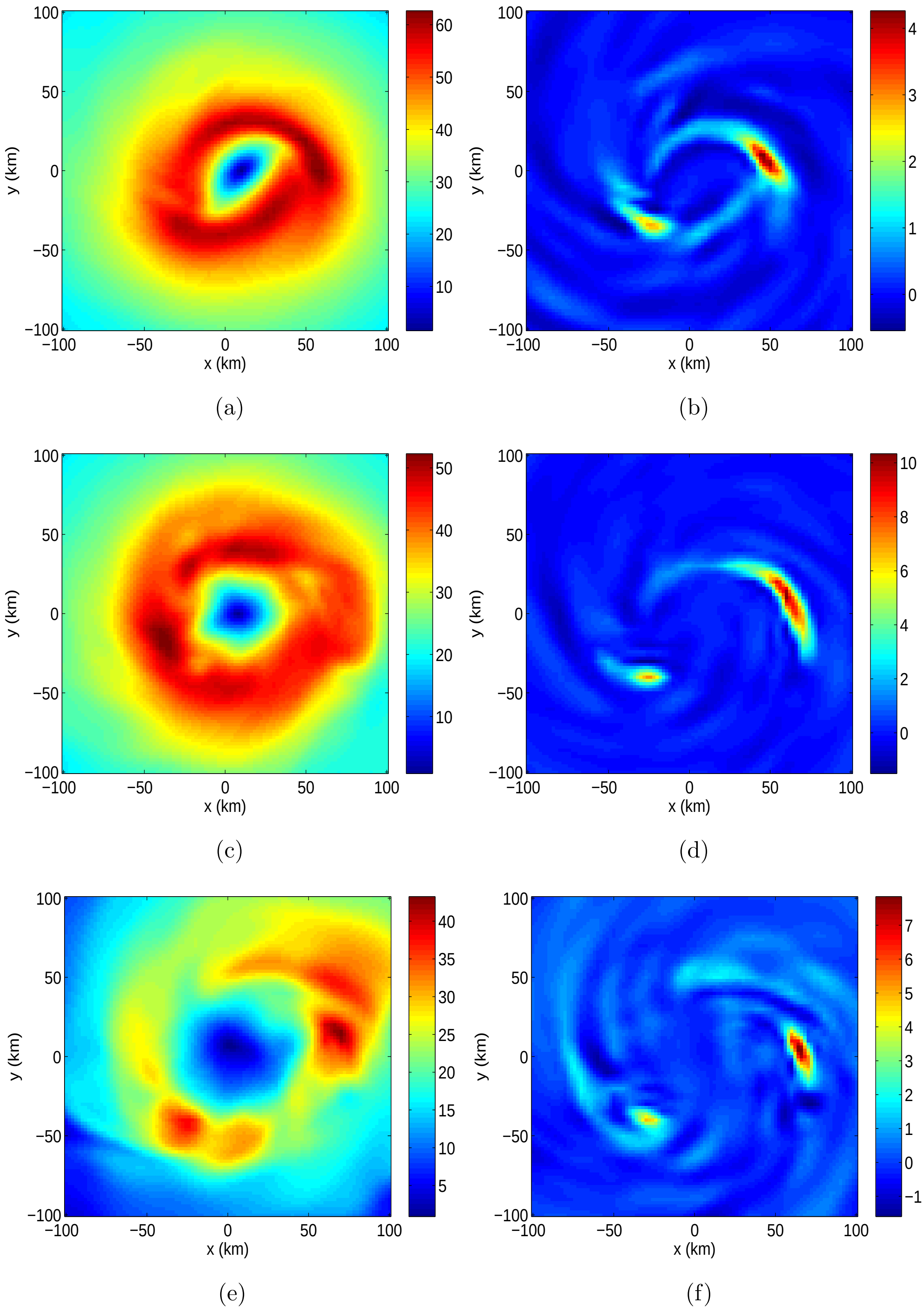

(a) (b) (c) (d) (e) (f)

Figure 6.10: Tangential wind (a,c,e) and updraft wind (b,d,f) at vertical levels of 1 km, 5 km, and 10 km

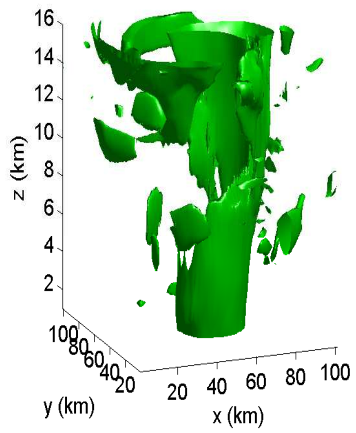

(a)

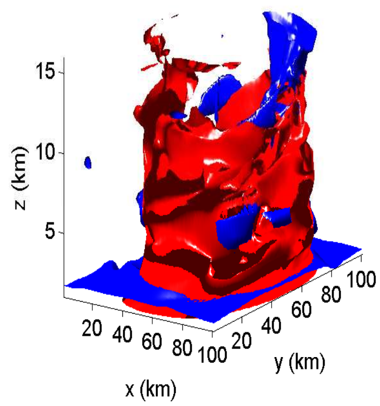

(b)

Figure 6.11: Ψ_{22} (a) and Ψ_{12} (red) and Ψ_{13} (blue) surfaces at initial time 62.5 hours with integration time 1 h.

distorted cylinder of maximal shear (Figure 6.11(a)). The shear in the η_3 subspace (almost vertical) is captured by the ϕ_3 field. Superimposing the ϕ_3 ridge on the ϕ_2 ridge gives a closed cylindrical surface of high shear. The LEEI also forms an almost closed cylindrical surface at lower levels ($z < 5\,\text{km}$), shown in Figure 6.11(b), and is completely enclosed by the shear surface (see Figure 6.12). The break in the LEEI occurs at a region of high updraft winds, as is apparent in Figure 6.10.

Stability and invariance of the LEEI The LEEI surface is repelling along the η_2 subspace, and attracting along the η_3 subspace. The repulsion is mainly in the eyewall region and is oriented approximately radially toward the region of strong circulation. Trajectories within the eye show more neutral stability relative to the LEEI, as is apparent in Figure 6.13, where the evolution of trajectories seeded on two straight lines intersecting the LEEI is depicted. This figure also illustrates that the LEEI is an invariant manifold, as trajectories in the eye and eyewall regions remain in these regions.

In Figure 6.14 we show the trajectories of Figure 6.13 together with the LEEI, which is displayed here in the form of stacked curves at different z-levels. The figure demonstrates again the invariance of the LEEI, since trajectories seeded inside and outside of it do not cross the manifold. Trajectories may, however, leave the eye by ascending or descending

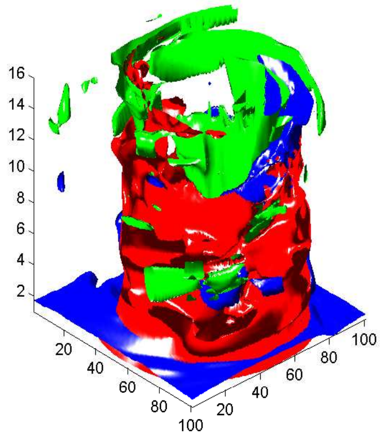

Figure 6.12: Combined hyperbolic (green), Ψ_{12} (red), and Ψ_{13} (blue) at initial time 62.5 hours with integration time 1h.

to escape the cylindrical region. On the one hand, buoyancy-produced upward motion allows some trajectories to escape the eye by passing over the LEEI at high z-levels (see Figure 6.13). On the other hand, a broadening of the LEEI manifold near the sea-surface shows that descending particles in the eye may escape the eye by exiting radially outward at low z-levels. The direct interaction between the two regions occurs at the break in the LEEI. If the LEEI is closed, which is common at low levels, there is no interaction. The rotational motion within a cyclone is strong enough that trajectories are unlikely to experience clockwise motion. The overlap in the ring can show two separate orientatations, which either allow counterclockwise rotation to mix eye trajectories into the eyewall, or visa versa.

6.11 Concluding remarks

We have developed a method for the computation of Lagrangian structures, which enabled us to define the eye-eyewall interface of a 3D hurricane model in terms of ridge surfaces of scalar fields that determine regions of trajectory separation of varying stability types. The advantages of the methods described here are fast convergence, as well as a decomposition of stability along orthogonal subspaces.

We have exactly located hyperbolic structures over varying initial times using a ridge extraction algorithm on vertical levels and constructing a full manifold. The extracted

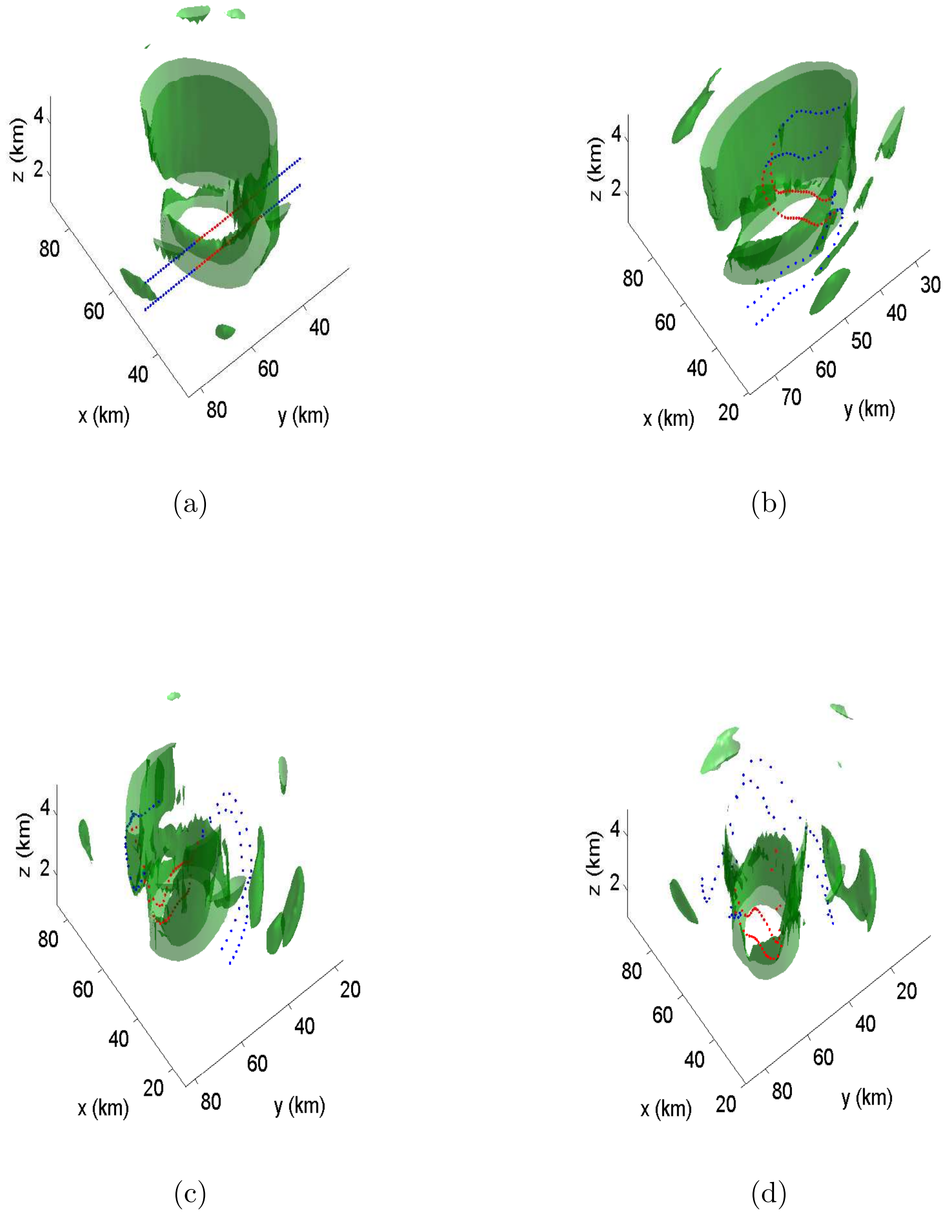

Figure 6.13: (a) Initial locations of trajectories and the LEEI integrated 1 hr, both at initial time 250 min. Trajectories are seeded on two straight lines intersecting the LEEI, with initial points located in the eye and eywall marked red and blue, respectively. The LEEI and the trajectory locations after 15 min, 30 min, and 45 min are shown in (c), (d), and (e), demonstrating the invariance of the LEEI.

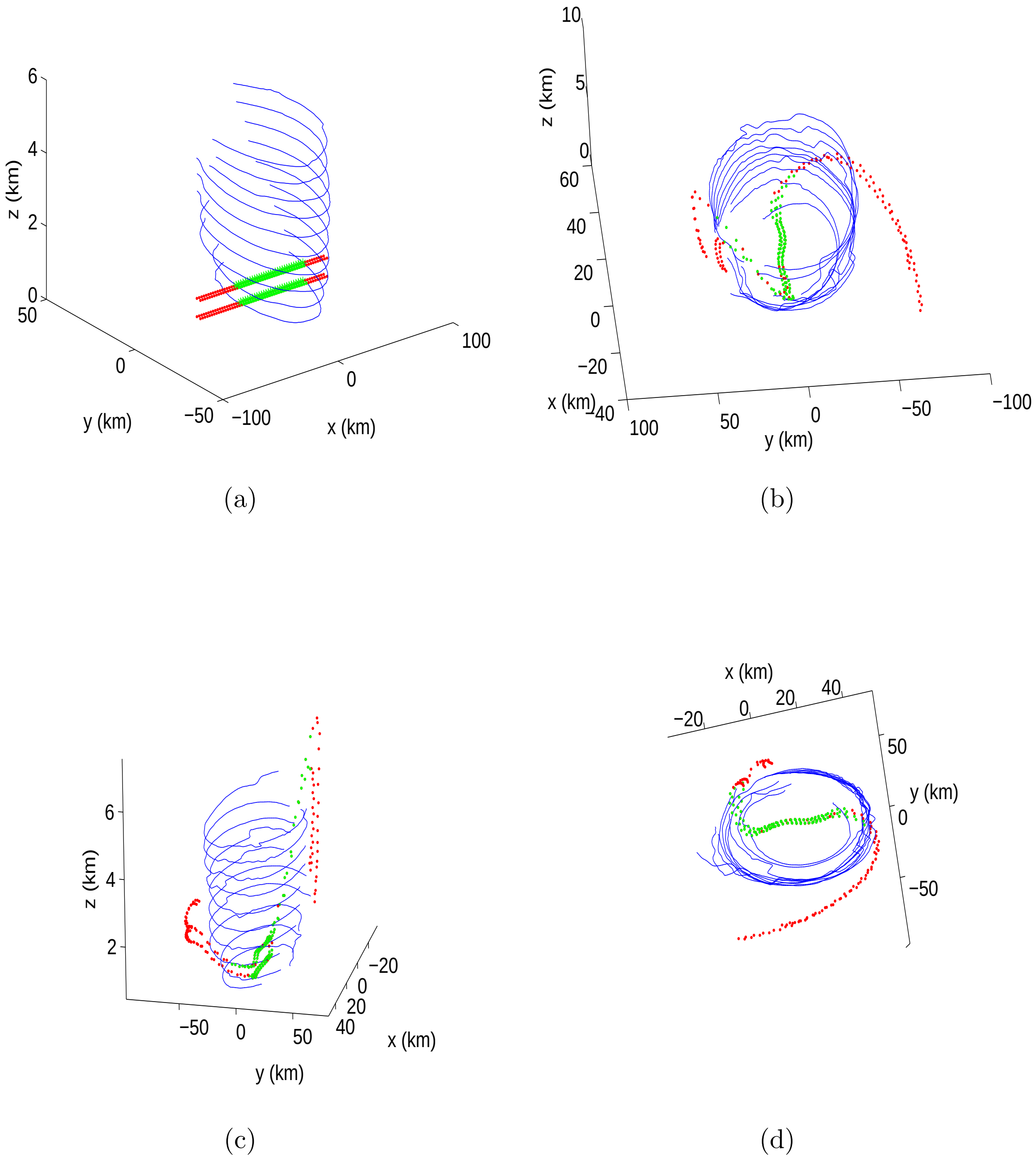

Figure 6.14: Trajectory and LEEI evolution as in Figure 6.13 with the LEEI displayed in the form of stacked curves (blue) at different z-levels. Trajectory points starting inside and outside of the LEEI are marked here green and red, respectively.

manifolds mark an impenetrable boundary between the eye and the eyewall. A stability analysis demonstrated that the boundary is indeed Lagrangian, that is, trajectories do not cross the boundary.

The definition of a Lagrangian eyewall leads to the question of quantifying mixing across the eye-eyewall boundary. Further work will be devoted to the automation of the ridge extraction procedure, which will allow the computation of mixing rates that vary with initial time. In this way results from our previous 2D studies Chapters 4 and 5 will be extended to the 3D case to determine time-dependent mixing rates.

The complete interaction of the subspaces in relation to shear is complex, and is an area of current study. In particular, the role of Lagrangian coherent structures during the intensification phase of a tropical cyclone is being investigated using the fields developed for this study.

Chapter 7

A time-dependent Lagrangian eye-eyewall interface

7.1 Summary

The eyewall of a tropical cyclone is usually defined in terms of Eulerian quantities such as instantaneous vorticity, potential temperature, or pressure. By contrast, a Lagrangian eyewall definition is based on the transport of particles. In this chapter, we continue the analysis of Chapter 6 of the Lagrangian eye-eyewall interface (LEEI), which is defined as a surface that acts as barrier to particle motion. As in Chapter 6, the surface is identified with a maximal ridge of a hyperbolic Lagrangian field, and varies with the initial time at which particles are seeded. The study here extends the study of Chapter 6 as follows. First, the ridge extraction algorithm used is now fully automated over time and z-levels, and smoothed by representing the ridge curves on z-slices in terms of Fourier descriptors. Secondly, the ridge curves for varying z-levels are matched to vertical basis functions leading to a 3D spatially continuous and low-dimensional representation of the LEEI, by truncating the combined azimuthal and vertical expansion. The surface is then analyzed over varying initial time, and structural differences in time and height are described. Specifically, this analysis provides information about the degree of axisymmetry of a mature hurricane.

7.2 Background and Overview

Tropical cyclones (TC's) have been the subject of much recent research [SMT$^+$99, MBAB06], which has led to a significant increase in our understanding of the physical mechanisms sustaining and the dynamics inherent in hurricanes, as well as to improved methods for tracking and predicting them. However, one of the major problems encountered in theoretical studies of TC's is that realistic 3D simulations require huge amounts of computing power and storage to handle large data sets, and the same problem is encountered in the analysis of real data. Although a great deal of research has been conducted on dimensionally reduced models, in particular axisymmetric [RE87] and planar [SMT$^+$99] models, these idealized models are not capable of capturing the essential features of a hurricane, since real data as well as large scale 3D simulations have shown that non-axisymmetric structures and vertical variations are important hurricane characteristics. Representing key dynamical structures of a fully 3D TC as low-dimensional data sets should provide significant gains in efficiency as well as a better understanding of essential properties of hurricane dynamics. The objective of this study is to extract a low-dimensional representation of a Lagrangian eye-eyewall interface from 3D simulation data.

In several recent studies of the structure of the eye and eyewall, see e.g. [KE01, MBAB06], it has been noted that intensification is coincident with the vanishing of higher wavenumber asymmetries, while low wavenumber asymmetries have been observed in real storms and in simplified models dring a mature state. According to the asymmetric balance (AB) theory of [SM93] the decay of higher wavenumber asymmetries is caused by shear. A quantitative study of the process of asymmetrization has been performed by [SIM95]. In this study, which is based on AB theory, time scales for particle separation and related to asymmetry decay in dependence of the aximuthal wavenumber involved have been extracted. In [RMMJG99] it is found that low-wavenumber asymmetries are dominant in model simulations and in the recorded data of Hurricane Olivia (1994), though the degree of asymmetry was sensitive to the location of vortex centers. Similar structures in 3D vortices have been reported in [NM02].

The thermodymics of the eye also plays an important role in intensification [Wil01, ZY02], and mixing between the eye and eyewall plays an important role in the transport of energy. Mixing of angular momentum inward into a ring like structure strengthens an axisymmetric vortex [KE01], while the collapsing of angular momentum into a monotonic profile is present in steady or weakening storms [SMT$^+$99].

Though those studies generally provide similar results regarding the role of asymmetries, there is no agreement on how to define the structure of the inner core. A tropical cyclone eye-eyewall interface is accepted as the region between the fast moving circulation and updrafts of the eyewall, and the region of slower solid body rotation contained within the eye. Common measures of vorticity, shear, as well as thermodynamic properties are often used to describe storm structure. Thermodynamically, the eye and eyewall have very different characteristics. The eye contains air with high potential temperature, low moisture, and low central pressure. The eyewall has a much higher moisture content, and is seen visually as a cylindrical wall of clouds extending from the sea-surface to the upper troposphere. The basic problem with any of these thermodynamic fields is that they are not continuously advected through the storm. In fact, higher wavenumber asymmetries have been shown to cause irreversible diffusion of many of these fields [HS09]. Though the eye and eyewall have very different thermodynamic properties, the mixing of material between the two regions cannot be accurately quantified in terms of these quantities. A definition of the boundary between the two regions that is based on material transport appears more adequate than a definition based on instantaneous thermodynamic properties.

In this chapter, we define the Lagrangian eye-eyewall interface (LEEI) as the surface that acts as a barrier for particle transport between the two regions. The time-varying velocity fields of a TC are well suited to Lagrangian methods, which are based on particle motion. The LEEI is a a cylindrical surface which is rotationally invariant for the axisymmetric model, while for a 3D model it is generally asymmetric, with the degree of asymmetry quantified by the amplitudes of aximuthal modes. The degree of asymmetry within a 3D storm is unclear, but studies [MBAB06] have noted that while many of the early asymmetries of intensification vanish after maturation into a single vortex, the low wavenumber asymetries, specifically wavenumbers 1 and 2, remain. True axisymmetry occurs when all of the asymmetries of the primary vortex vanish during the mature phase. The remaining asymetries can be due to convective bursts, or material transport between the eye and eyewall. In this study, we examine the role of transport in the evolution of asymmetries during a mature TC.

For the time-dependent velocity fields of a hurricane, Lagrangian techniques are required to accurately define the structures associated with particle transport. In several recent studies in Lagrangian dynamics, techniques have been developed for locating and extracting structures from time-dependent velocity fields, see [HP97, HY00]. For an application of these methods to geophysical flows, see [KL02, JL01].

Our study builds upon previous work of Chapter 6 by extending a specific type of Lagrangian hyperbolic structure to a moving frame, which provides a barrier to transport between the eye and eyewall that is continuous in initial time (time at which trajectories are seeded). A benefit of our method is fast convergence of the Lagrangian fields, along with a ridge extraction algorithm that locates the hyperbolic structure exactly. In this paper, we extend the ridge extraction from Chapter 6 to a moving frame, and provide a good approximation to the true maximal hyperbolic surfaces that is continuous, and computed in an automated manner, by using a representation of the surface in terms of Fouries descriptors. Combining the Fourier descriptors with a fit of radial basis functions to capture the dependence on the vertical coordinate yields a smooth representation of the LEEI. A similar procedure is applied to compute a maximal shearing surface. The combined amplitudes of the azimuthal and vertical modes are then analyzed, which results in a dynamical model that captures the temporal evolution of the LEEI, and allows to quantify the asymmetries due to particle transport. By using a shape-based coordinate system, the vortex center is unambiguously defined as the centroid of the LEEI.

Energy considerations show that the LEEI-structure is well approximated by the first 3 Fourier modes and 15 radial basis functions vertically (yielding 90% of the energy). Thus, our approach yields a low-dimensional representation of a dynamically evolving LEEI.

The outline of this chapter is as follows. In Section 7.2, we extend the study of Chapter 6.9 by developing a fully automated (over z-levels and across initial time) ridge extraction algorithm that generates closed maximal ridge-curves on z-slices, which are smoothed by truncating an expansion in terms of Fourier descriptors. The Fourier descriptors provide information about the degree of axisymmetry of a mature hurricane. Matching the variation of the ridge-curves with z-levels to vertical basis functions then leads, in Section 7.3, to a 3D continuous and low-dimensional representation of the LEEI. Concluding remarks and an outlook on future work are given in Section 7.4.

Model

The model from which the velocity data are calculated is the MM5 3D hurricane model, which was used in Chapter 6. The velocity fields are given on staggered grids, with z levels given in pressure coordinates. The initilization used in this study was a nonhydrostatic axisymmetric vortex initilization as in [NSM08]. The model run was a high resolution run with x-y grid spacing of 1.67 km, and a time step output of 2 min.

7.3 Ridge extraction

The Lagrangian fields used in this study are the fields Ψ_{ij} introduced in Chapter 6.2. As in Chapter 6, the LEEI is identified with the maximal surface of Ψ_{22} that encloses the z-axis, and the maximal shear surface is identified with the maximal ridge surface of ϕ_2. In this paper, the ridge extraction algorithm of Chapter 6 is extended in an automated manner across varying initial time, and at each z-level the ridge is smoothed by representing it in terms of a reduced set of Fourier descriptors. Since the data are rather noisy, the smoothing procedure combined with gradient climbing, see Chapter 6, yields a "best fit surface".

At given z-levels, a ridge-curve is computed by evolving an initial guess of an ordered set of points towards the ridge through gradient climbing. A change to our previous calculation is that the points are uniformly azimuthally distributed, and the gradient climbing is restricted to the radial direction. Let $R = (R_x, R_y)$ be the initial guess. The Fourier descriptors of R are defined $F_R = \mathcal{F}(R_x + iR_y)$, where $\mathcal{F}$ denotes the the discrete Fourier transform (computed through the fast Fourier transform algorithm). The curve is smoothed by zeroing higher order Fourier descriptors and mapping back to Cartesian coordinates via the inverse Fourier transform. This yields a new ordereed set of points R', which is again evolved through radial gradient climbing. The algorithm for ridge extraction at a given z-level can be summarized as follows:

Algorithm

1. Choose an ordered set of aximuthally uniformly distributed points as an initial guess.
2. Evolve points through gradient climbing in the radial direction.
3. Apply a fast Fourier transform to the evolved points.
4. Set higher order Fourier descriptors to zero and apply inverse fast Fourier transform.
5. Continue 2-4 until convergence is reached.

In our computation, we have used 70 points and kept 10 Fourier descriptors for Fourier inversion. Examples of the resulting "best fit ridge curves" are shown in Figure 7.1. The advantage of this method is that the ridge points for varying z-levels have identical aximuthal distributions and so are stacked to form a ridge surface that can be represented in a matrix.

This leads to easy visualization, see Figure 7.2, and the possibility to build a continuous dynamical model of the surface. In addition, at a given z-level, the method provides a center given by the zero frequency Fourier descriptor, and higher order Fourier descriptors provide information about the degree of asymmetry.

We note that the algorithm used here is a priori designed to find a closed ridge-curve on each z-level. In our previous computation, without smoothing and gradient climbing restricted to the radial direction, some of the LEEI sections show gaps which allow transport between the eye and eyewall. The presence of these gaps is an effect of convective bursts in the eyewall.

7.3.1 Continuation across z-levels and initial time

The ridge extraction on a fixed z-level described above is extended across varying initial times as follows.

1. For fixed initial time, the ridge curves are advanced from bottom to top by using the converged ridge from the previous computation as initial guess for the computation at the next z-level.

2. The bottom ridge-curve computed at a given initial time is used as initial guess for the computation of the bottom ridge curve at the next initial time.

7.3.2 Areas and volume

The size of the eye is measured by the areas of the LEEI-sections and by the total volume. The area, A, of the eye at a z-slice is computed from the closed ridge-curve using Green's theorem, according to

$$A = \int \left(R_x(s) \frac{d}{ds} R_y(s) - R_y(s) \frac{d}{ds} R_x(s) \right) ds, \tag{7.1}$$

where $R(s)$ is arclength parameterization of the curve $R = (R_x(s), R_y(s))$. Given the areas at all z-levels, the volume of the eye, V, is approximated by

$$V = \Delta z \sum_{n=0}^{N-1} A_n, \tag{7.2}$$

where N is the number of z-levels, and A_n is the eye-area at level $z = n\Delta z$. In our calculation, $N = 40$ and $\Delta z = 250$ meters. Areas and volume as function of initial time varied between 60 and 62.5 hours are depicted in Figure 7.4.

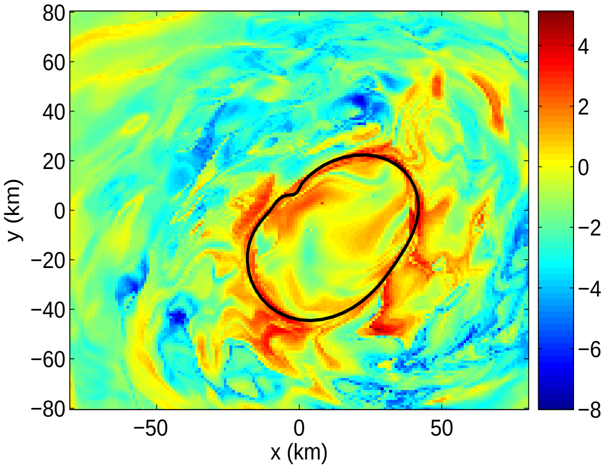

(a)

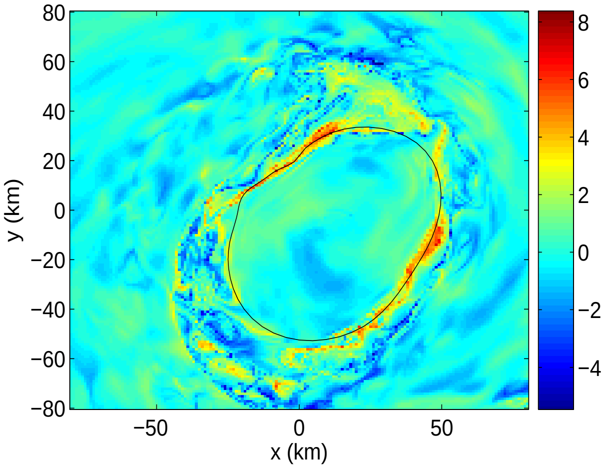

(b)

Figure 7.1: $\log(\Psi_{22})$ and ridge at initial time of 60 hours with 1 hour integration time, at z-levels of 500 m. (a), and 3500 m. (b).

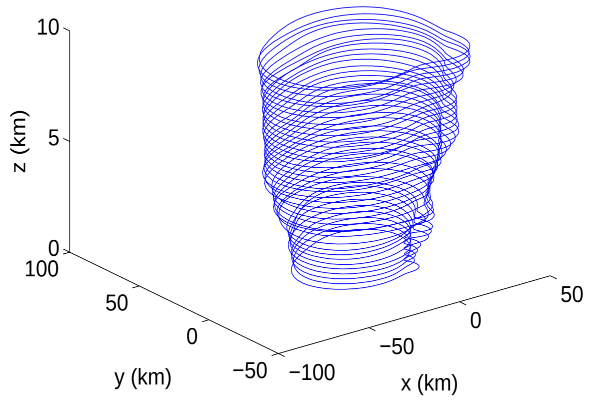

Figure 7.2: $\log(\Psi_{22})$ ridges stacked on z-levels.

7.3.3 Asymmetries

The relative contributions of the individual Fourier descriptors to the total energy provide information about the degree and structure of the asymmetries contained in the LEEI. In Figure 7.5 we show the contributions of the wavenumber 1 and 2 components as functions of initial time and z-level. The figure indicates that these two modes contain almost 90% of the energy. Inspection of contributions from other modes (not shown) shows that the contributions of the low-frequency Fourier descriptors increase as the area decreases. Thus, axisymmetry is a more valid assumption of smaller eyes.

7.4 Dimensionally reduced model

The ridge extraction of Section 3 produces a representation of the LEEI that is continuous in the azimuthal variable ϕ, and discrete in the vertical coordinate z. Setting $c = x + iy$, this representation can be written as

$$c_n(\varphi, t) = \sum_{m=-M}^{M} \mathcal{F}_{R,mn}(t) e^{im\varphi}, \tag{7.3}$$

where $\mathcal{F}_{R,mn}$ is the Fourier descriptor at level z_n, $(0 \leq n \leq N)$ for wavenumber m, amd $M = 35$, $N = 40$ in our calculations. A continuous representation across z is achieved by matching (7.3) to vertical basis functions $B_k(z)$, $0 \leq k \leq N$, as

$$c(\varphi, z, t) = \sum_{k=0}^{N} \sum_{m=-M}^{M} c_{mk}(t) B_k(z) e^{im\varphi}. \tag{7.4}$$

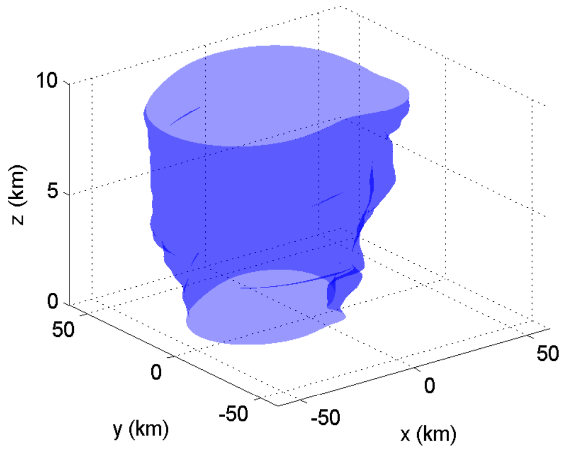

(a)

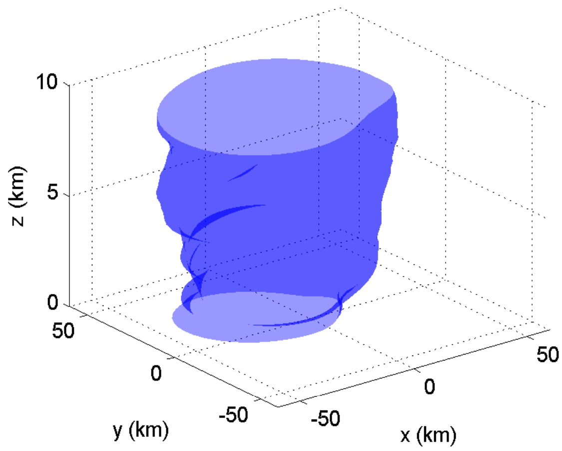

(b)

Figure 7.3: Ψ_{22} maximal surface at initial times 60 hours (a) and 64 hours (b) with 1 hour integration time.

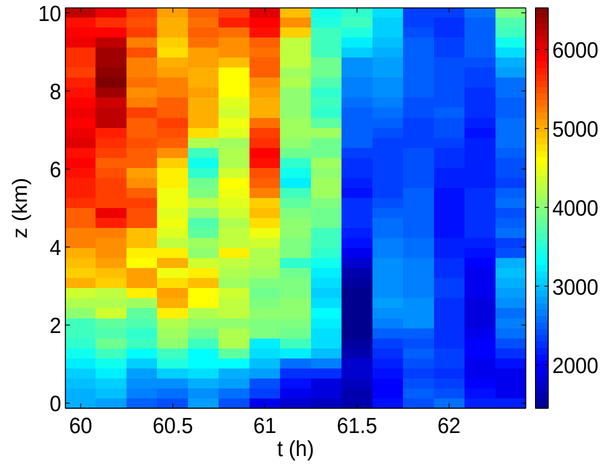

(a)

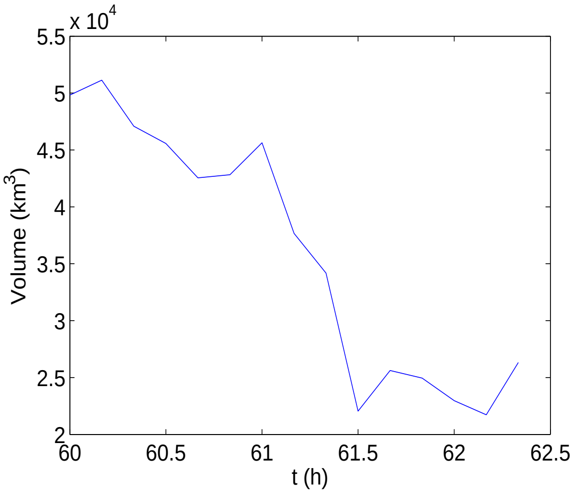

(b)

Figure 7.4: Areas on z-levels (a) and volumes (b) of the LEEI as functions of initial time

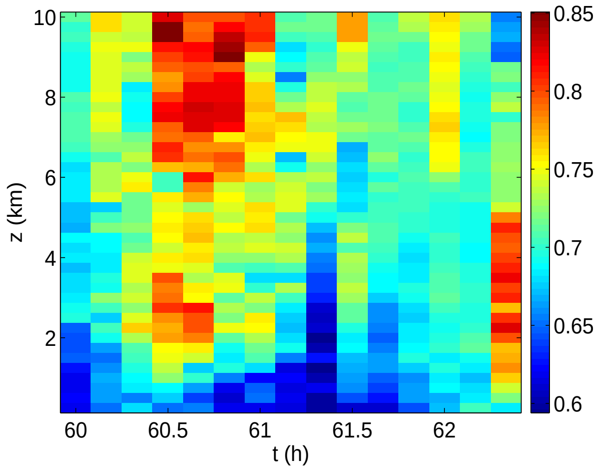

(a)

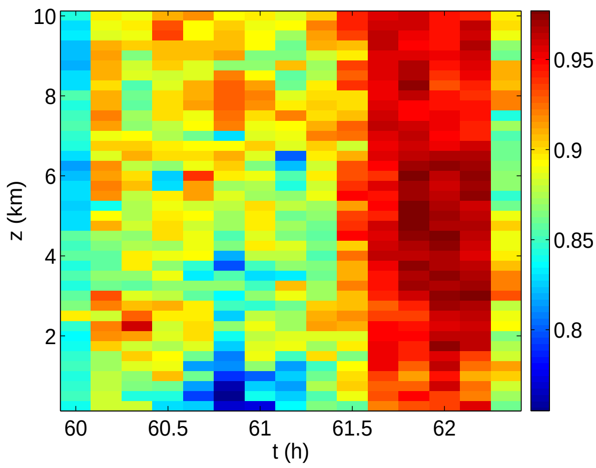

(b)

Figure 7.5: Wavenumber 1 (a) and 2 (b) component of the Fourier descriptor for varying z-levels and initial times for the LEEI.

The condition that (7.4) coincides with (7.3) at $z = z_n$ yields a linear equation for the coefficient vectors $c_m = (c_{m0}, \cdots, c_{mN})$,

$$\sum_{k=0}^{N} c_{mk}(t) B_k(z_n) = \mathcal{F}_{R,mn}(t), \tag{7.5}$$

which has a unique solution for each m and t if the basis functions are linearly independent.

We consider two choices for the vertical basis functions. The first choice is Fourier basis functions,

$$B_k(z) = e^{2\pi i k z / z_N}, \tag{7.6}$$

and the second choice is radial basis functions (RBF's),

$$B_k(z) = \phi(|z - d_k|), \tag{7.7}$$

where ϕ is any RBF and the d_k are uniformly distributed centers in the vertical range. After experimenting with different RBF's, we found that the choice

$$\phi(\xi) = \sqrt{\xi^2 + \beta} \tag{7.8}$$

with $\beta = 20$ works well, although the results are not very sensitive to variations in β.

The approximations of the first 3 Fourier descriptors at a fixed initial time as functions of z-level in terms of 5 and 10 basis functions are shown in Figures 7.6 and 7.7 respectively, along with the relative errors in these approximations. Using 5 and 10 RBF's captures 90% and 95% of the information in the vertical variation. For 10 RBF's this corresponds to a reduction by 80%. The weights $|c_{mk}|^2 + |c_{-mk}|^2$ for 10 RBF's are shown in Figure 7.8 as functions of t for $m = 1$ and $m = 2$. The RBF-representation reproduces the vertical shape of the eyewall and can be used to analyze the vertical tilt of the LEEI in the presence of vertical wind shear. This and a time-series analysis of the coefficient functions is the subject of a forthcoming study. With 10 RBF's and 3 Fourier descriptors, our approach yields a 30-dimensional model for the dynamics of the LEEI.

7.5 Concluding remarks

The dynamics of a 3D Lagrangian eye-eyewall interface were studied by applying Lagrangian methods for its construction, and using methods of data reduction in the extraction and analysis of this structure. The LEEI was defined as a ridge of a Lagrangian field that acts as a barrier for particle transport, and varies with initial time. The construction of a reduced

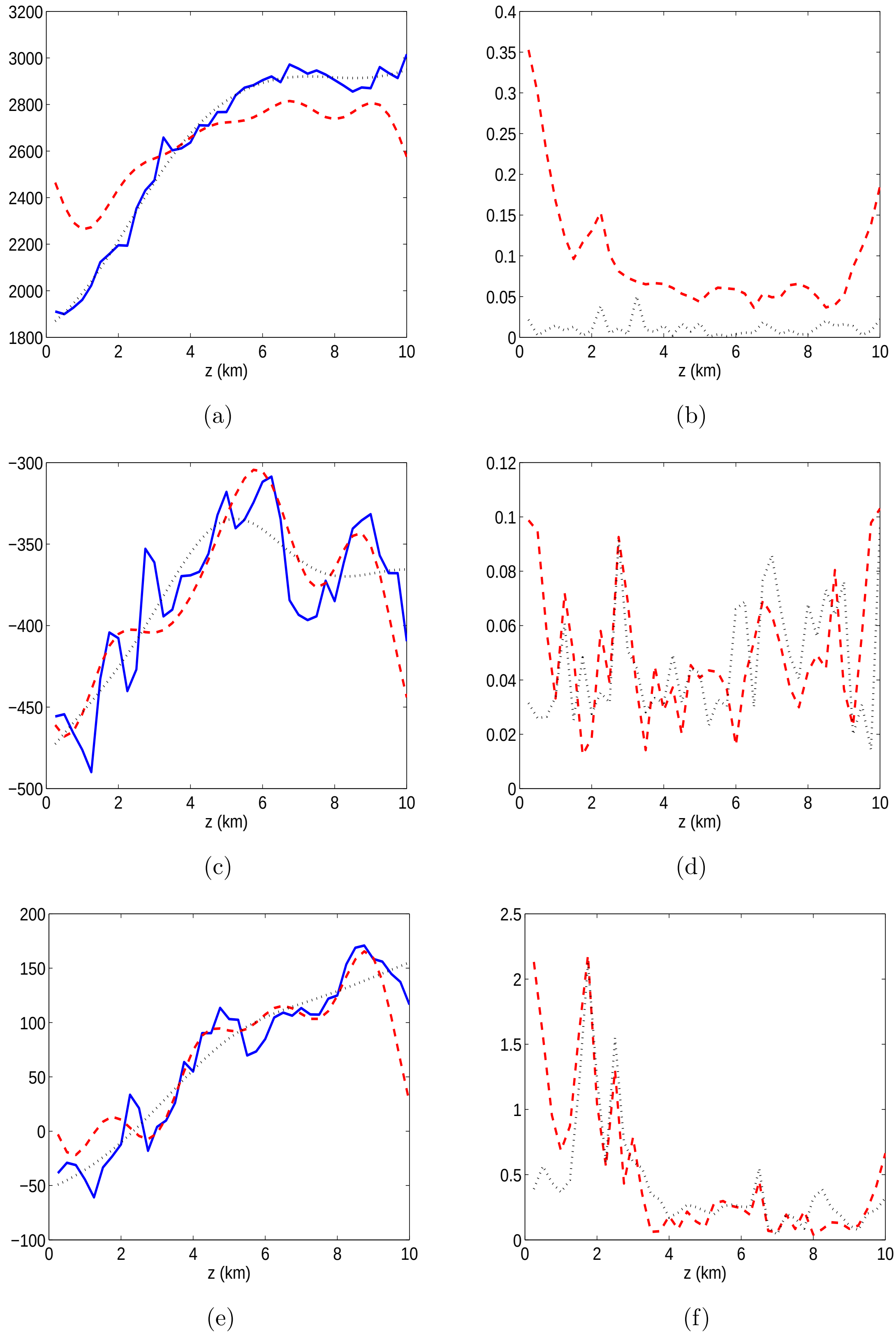

Figure 7.6: Fourier descriptors (blue) for wavenumbers 0 a), 1 (c), and 2 (e) as functions of z-level at t=60 hours, and their approximations using 5 Fourier basis functions (red dashed) and RBF's (red dashed-dotted). The relative errors of the representations in (a), (c), and (e) are depicted in (b), (d), and (f) respectively.

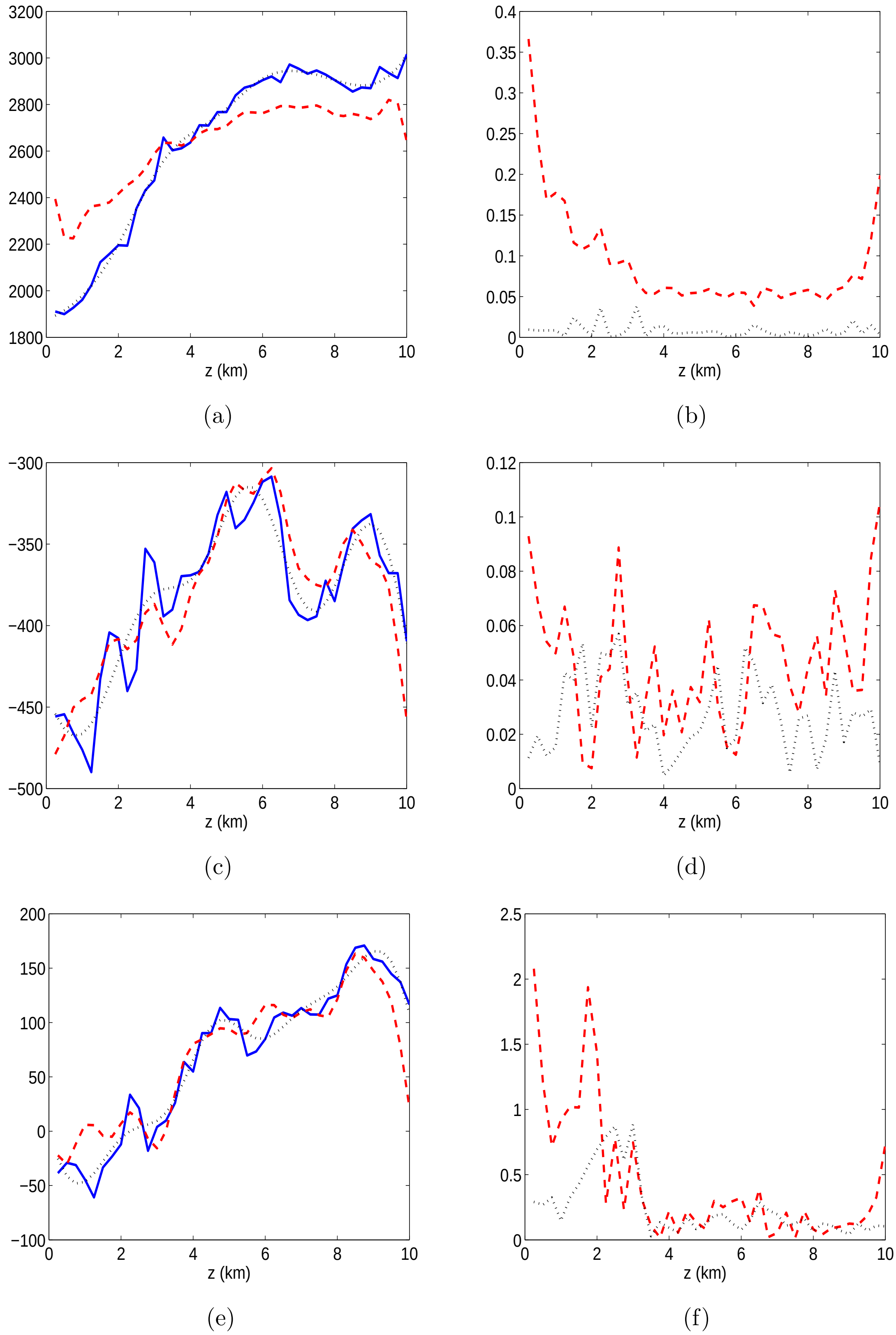

Figure 7.7: Fourier descriptors (blue) for wavenumbers 0 a), 1 (c), and 2 (e) as functions of z-level at t=60 hours, and their approximations using 10 Fourier basis functions (red dashed) and RBF's (red dashed-dotted). The relative errors of the representations in (a), (c), and (e) are depicted in (b), (d), and (f) respectively.

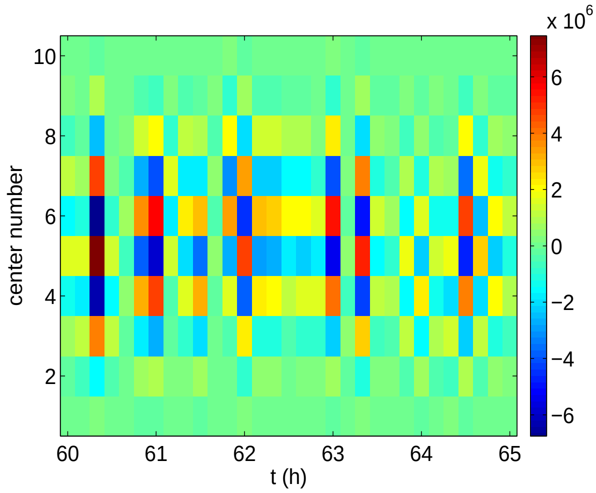

(a)

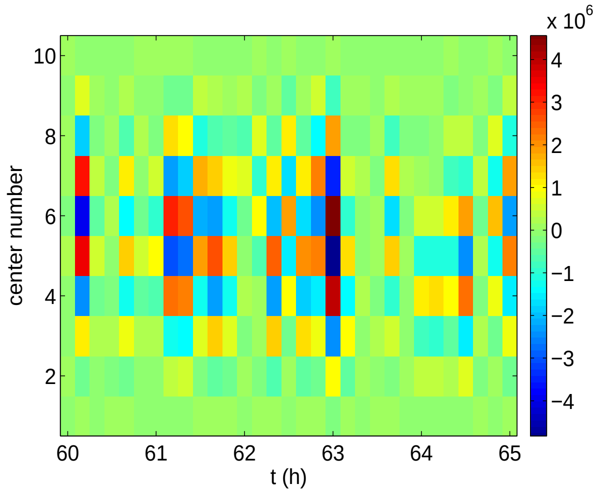

(b)

Figure 7.8: Weights of RBF centers across varying initial time for first (a) and second (b) Fourier descriptor.

dimensional model using Fourier descriptors and appropriate vertical modes showed that the structure can be viewed as lower dimensional, both in the azimuthal and the vertical directions. Moreover, the amount of information contained within the lower dimensional data set characterizes the degree of axisymmetry in the model during a mature state, and the "shape-based coordinate" eliminated the problem of a nonstationary vortex center. The temporal evolution of the LEEI can be studied by analyzing the time series of the coefficients associated with the spatial basis functions, which is the subject of future work. Further work in this direction will include a similar analysis for an intensifying storm, where the complexity increases due to the nonstationary evolution and interaction of mesovortices.

Chapter 8

Lagrangian coherent structures involved in vortical hot tower interaction

8.1 Summary

Vortical hot towers (VHT's) have been recently recognized as the key coherent structures present during tropical cyclone (TC) intensification. Though obvious from inspection as warm core localized mesovortices, their interaction and role in the transfer of energy is a difficult problem, since the structures are inherently 3-dimensional, and highly time-dependent. So far, no Lagrangian studies have attempted to capture either of these properties. Current Lagrangian methods can handle time-dependent structures effectively, however most applications have been to 2D flows with weak time-dependence. In this chapter, we apply new Lagrangian techniques developed for 3D coherent structures, to study the dynamics of VHT's. Our findings are that (1) VHT's are elliptic structures with parabolic boundaries, and (2) associated with VHT's are hyperbolic structures that determine the mixing of energy and the merging of VHT's during intensification. The relation between the VHT's and the hyperbolic structures confirms that the interaction of mesovortices has the ability to dictate the transport of material into a single ring of high vorticity.

8.2 Background and overview

The study of tropical cyclones has attracted much recent interest, with the level of mathematical sophistication in these studies steadily increasing. While most of these efforts have focused on mature storms, the recent discovery of structures and processes dominating tropical cyclogenesis have sparked growing interest in the intensification process. Knowing whether a particular tropical storm will intensify is of obvious importance to coastal communities, shipping, and marine assets, and a better understanding of the process involved in intensification can be expected to lead to improved prediction of hurricane formation.

Tropical cyclogenesis is an inherently 3D and asymmetric process, marked by the spinup of individual moist convective mesovortices [SMN09], which are found in the tropical atmosphere prior to the formation of a tropical depression. There are two proposed mechanisms for the spinup of TC's. The first is through sea-surface winds that transfer energy to the core through wind induced surface heat exchange (WISHE), [MNSP09]. The second mechanism is through the interaction of warm-core vortex structures, termed vortical hot towers (VHT's), [HMD04]. The VHT's are assumed to be the key coherent structure present during TC formation [MNCS06, DMW09]. Their role for intensification is highly important, as the axisymmetric vortex does not develop until the temperature in the surrounding environment reaches the temperature in the VHT's. Thus, the thermal transport properties associated with the interaction of VHT's play a key role for intensification.

VHT's are localized structures creating a protected environment [McW84] which supports the conversion of latent heat into rotational energy [SH82, HS86] during their lifecycle of approximately 1 hour. Though VHT's have a small horizontal scale, their upscale organization is a mechanism for the transport of energy into a single vortex [MNCS06]. Their relation to environmental flow is not well understood, although in [DMW09] the low entrainment rate of cat's eye features is proposed as a potential mechanism for less disturbance from the environment. The studies of [FR99] and [FR01] provide some insight into the effects of environmental flow for mature storms, but the case of a developing storm is still not understood.

Understanding the transport induced by VHT interaction requires advanced mathematical techniques, due to the spatio-temporal complexities of the velocity fields. VHT's are the most obvious coherent structure during intensification, and are seen as regions of high convection and vorticity. They are also trackable, and robust through changing wind fields.

However, their role in the transport of thermodynamic properties cannot be fully understood without knowledge of the related flow dividing structures associated with VHT's. The interaction between mesovortices can be characterized by the coherent structures between them, which either allow or prohibit interaction. The manifolds linking VHT's cannot be found by Eulerian methods, since this requires to trajectories. The time-dependence of the velocity fields implies that the manifolds are of finite length. The appearance of these connecting structures has been seen in Eulerian phase portraits, see e.g. [PMFS03, DMW09], but they are difficult to track and visualize due to the time-dependence and shear present in tropical cyclones.

A new class of finite-time Lagrangian methods allows for the detection of Lagrangian coherent structures (LCS's), which are the finite-time analog of stable and unstable manifolds. Haller and coauthors [HP97, HY00, Hal00] proposed finite-time Lyapunov exponents (FTLE's) as a method for measuring trajectory separation, and maximal ridges of an FTLE field mark LCS's. This method was shown to be robust under approximation errors of the velocity fields [Hal02], and it allows to treat time-dependence of a velocity field. Recently, there have been many applications of FTLE's by the dynamical systems community to a variety of fluid flows. The applications to atmospheric flows have been more limited, but several studies have ventured into this area. In [SH09], Chapter 4, and Chapter 5, FTLE's have been applied to tropical cyclones, and in [TMH$^+$09], FTLE's are used in a study of the subtropical jetstream.

Though FTLE's are easily computed, and handle time-dependence and approximation errors of velocity data, they do not differentiate between hyperbolicity and shear effectively, and are therefore limited for atmospheric flows. The study of Chapter 5 showed that the methods of [HI03] could be used even in the presence of large-scale shear to detect LCS's. Though the LCS's were not manifolds, since they move with the Rossby wave speed, they were shown to be robust across time, and influence the systematic transport of trajectories.

The 2D method of separating shear was extended to 3D in Chapter 6, and was used to compute a Lagrangian eye-eyewall interface during a mature, but still highly time-dependent velocity field. In this study, 3D flow separation has been decomposed into several hyperbolic and shear components. An additional benefit of the method was that it offers faster convergence than FTLE's. The key ingredient in the approach of Chapter 6 was a specific choice of coordinates adapted to the helical trajectory motion. Though the VHT interaction is clearly more complex than the evolution of a single vortex, the coordinate system proposed in Chapter 6 is still valid, as long as trajectories entrained in vortices remain there over sufficiently long time periods. We note that other studies [PMFS03, Saf81, Pro99, SDM06, Tru54] have investigated the interaction between and entrainment of particles by vortices using different methods.

In this study, we apply the methods of Chapter 6 to a 3D intensifying tropical cyclone, and examine the LCS's involved in VHT interaction. We show that while the VHT's constitute an important type of LCS, which is parabolic, the hyperbolic LCS's separating the VHT's are shown to control the transport of material into the core, and are thus the important LCS's involved in tropical cyclogenesis. Our study also shows the length scales over which VHT's can interact, and demonstrates that multiple VHT's may be involved in this interaction [HMD04], which may result in the upscale organization proposed by [MNCS06].

The outline of this chapter is as follows. Section 8.2 provides an overview of the coordinate system and the Lagrangian methods used in this study. For further mathematical details we refer to Chapter 6. In Section 8.3, the model from which the velocity data are calculated is described, along with numerical details regarding trajectory calculations. Our main results are presented in Section 8.4. The structures shown by the Lagrangian fields indicate two phases of hurricane intensification, an initial cryatallization phase (5-20 hours) with many VHT's present and arranged symmetrically, and a diabatic vortex merger phase (20-30 hours) that leads to the formation of an eyewall, We conclude, in Section 8.5, with further remarks on the relation between Lagrangian hyperbolic structures and VHT's, and an outlook on future studies stimulated by the results of this chapter.

8.3 Model and numerical details

The model used in this study is the fifth generation Penn State/NCAR mesoscale model (MM5), [GDS95] and [Dud93]. The model run is a fully 3D nonhydrostatic vortex evolved with bulk aerodynamic scheme and initialized from a moist idealized axisymmetric vortex which is a high resolution run of experiment S5 from [NSM08]. Surface fluxes are uncapped and allowed to vary with wind speed, which allows WISHE amplification. Though the initial condition is axisymmetric, asymmetries develop quickly in the form of convective bursts, and then vanish leaving only the low wavenumber asymmetries during the mature state, here for $t > 50$ hours. The VHT's begin to emerge at about 5 hours in this simulation. In this study we examine fields from times of t=0 to 50 hours during intensification.

Velocity data is calculated on a set of four 3D nested grids in the horizontal plane with $x - y$ spacing of 1.67 km on the innermost domain of 300×300 km. Velocity data for trajectory computations is taken only from the innermost grid. Vertical coordinates are given on σ-levels, and vary in time, with a time-step of 2 min. Trajectory integrations are performed using a fourth order Runge-Kutta scheme, on grids of evenly spaced points in a box of size 220 km by 220 km by 16 km in x, y, and z respectively, with horizontal resolution of 1 km, and vertical resolution of 250 m, resulting in approximately 2.5 million trajectories at each initial time.

Integration times using Lagrangian methods are chosen long enough to resolve structures while minimizing computation, particularly in the case of a moving time frame. Here, we have chosen $T = 1$ hour as the primary integration time, which is consistent with the typical time of existence of a VHT, and may allow the assumption of slow time-dependence along trajectories. The initial time, t, is varied between 5 and 30 hours, which is a characteristic time range for VHT interaction during the intensification phase.

For this study, the numerical methods and choice of coordinate frame presented in Chapter 6 are used for computation of the Ψ_{22} fields. In addition, the angle of rotation ϕ is used as a measure of shear. The 3D FTLE-fields and 2D "planar" FTLE-fields, which are computed by ignoring the vertical component of 3D trajectories and using the definitions from Chapter 3.4.1. The planar FTLE is better suited for the aspect ratio of atmospheric models. The Ψ_{22} fields are more suitable for atmospheric flows since zero vertical velocity reduces the Ψ_{22} field to the R-field described in Chapter 5.

8.4 Lagrangian fields

The Lagrangian fields display coherent sets of time-dependent structures, which can be visualized over varying initial times. To illustrate the spatial forms of these structures, we show in Figure 8.1 the planar (at fixed z-level) FTLE, Ψ_{22}, and ϕ fields at $z = 1$ km. and $t = 10$ hours, along with zooms highlighting a particular structure. The FTLE field shows many high regions of separation, including vortices and hyperbolic lines, while the Ψ_{22} field shows only hyperbolic separation, and the shearing is captured by the angle of rotation ϕ.

8.4.1 Structures and asymmetry

The LCS's are coherent through varying z-levels, showing the 3D nature of the structures, which indicates that vortex interaction plays a crucial role in the transport and organization of energy. Since the vortices reach heights of 10 km, well above the sea-surface, the role of WISHE in the transport of energy is seen as less important than the vortex interaction.

Initial crystalization phase

At 5 hours, the VHT's can be recognized as ringlike structures in the planar FTLE fields, see Figure 8.2(ace). Potential temperature contours indicate that the structures at this phase are highly localized, and regions of high potential temperature are at the same places as the vortex rings. The Ψ_{22} ridges located between the vortex rings have the form of a "crystal lattice" with approximately hexagonal symmetry, that acts as a barrier to interaction between the vortices, see Figure 8.2(bde). We note that the VHT's emerge just after 5 hours, but the forward integration time of 1 hour incorparates velocity data over the time range of $5 \leq t \leq 6$ hours, allowing the VHT's at 5.5 hours to been seen in Lagrangian fields at $t_0 = 5$ hours.

At 10 hours (Figure 8.3), many VHT's are present in an annulus of about 60 to 80 km, seen as rings in the planar FTLE field, and as countours of high potential temperature. Filamentation has developed from the rings showing more interaction with neighboring VHT's. The filaments are also ridges of the Ψ_{22} field, which confirms that they are hyperbolic. There are two types of ridges surrounding mesovortices. In the first case, a Ψ_{22} ridge is circular and almost enclosing a region of localized high potential temperature. The mesovortex is then protected by the hyperbolic ridge, and does not interact with surrounding mesovortices. In the second case, a ridge and a valley are aligned at the boundary of the mesovortex, with the attracting set showing interaction of outside air with the mesovortex. After the mesovortex is allowed to interact, the ridge is no longer protecting the vortex, and generally lengthens as it is advected with the mean flow. The ridge then either vanishes, as its role is complete, or governs the interaction between adjacent mesovortices. This behavior is in contrast to observations reported in [PMFS03] for 2D barotropic mesovortex interaction, which suggest that partial interactions may occur. With the stong temporal variation of the VHT's, and lifetimes of only 1 hour, the interaction seen here is either splitting, or complete merger, since a weaker VHT is annihilated by a stronger one.

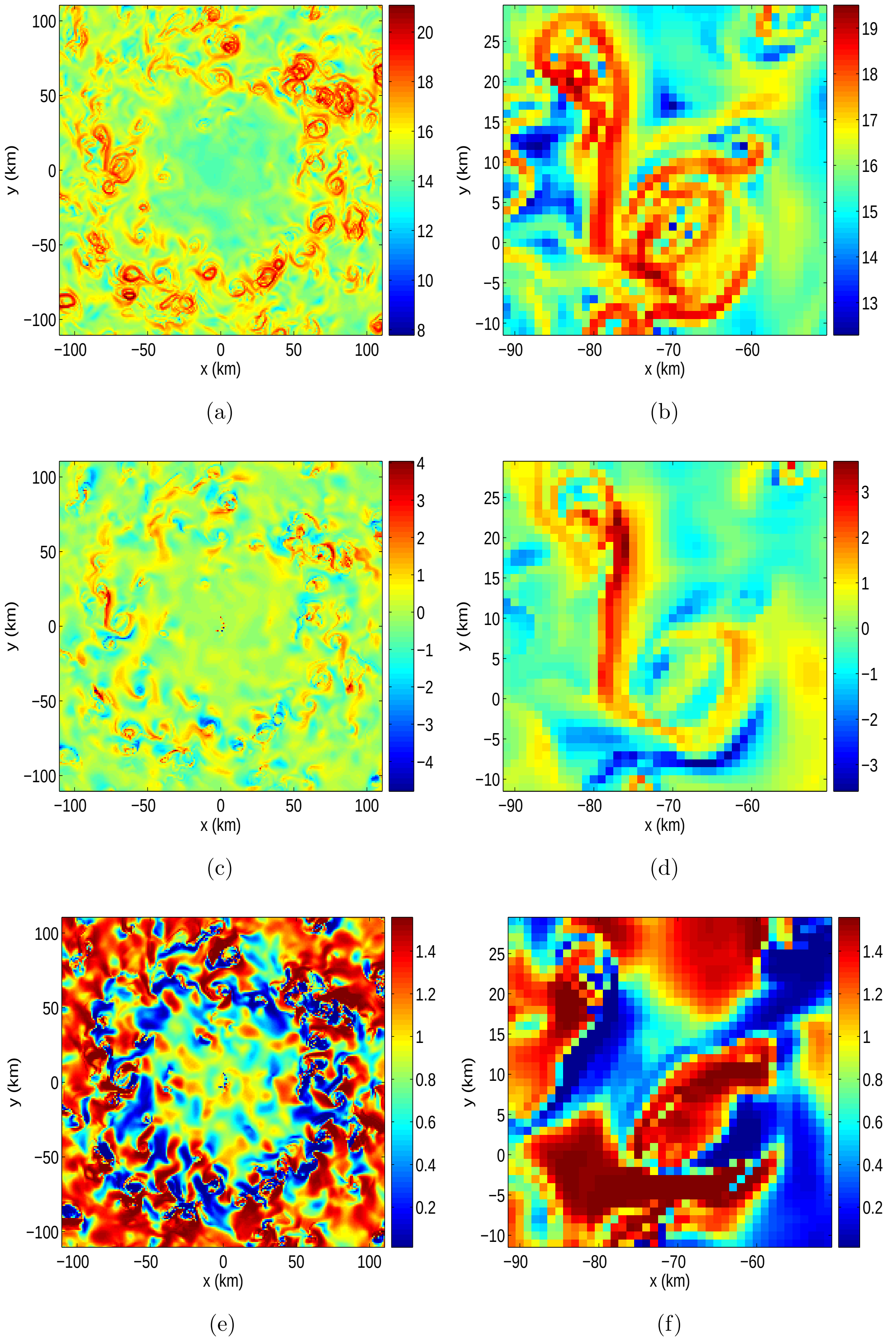

Figure 8.1: Planar FTLE, Ψ_{22}, and ϕ fields in (a), (c), and (e) respectively, at initial time of 10 hours with integration time of 1 hour. A zoom into a particular structure is shown in (b), (d), and (f).

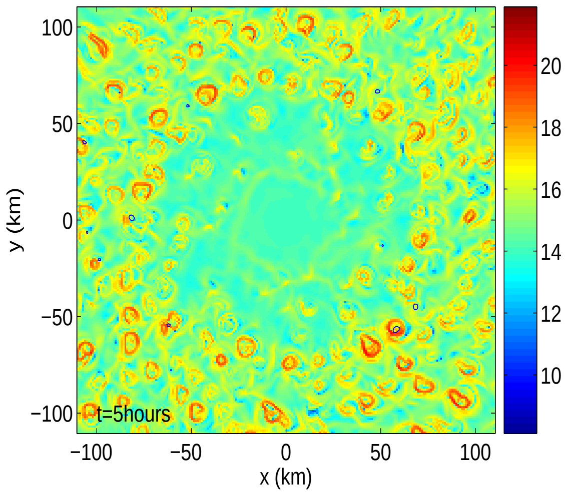

(a)

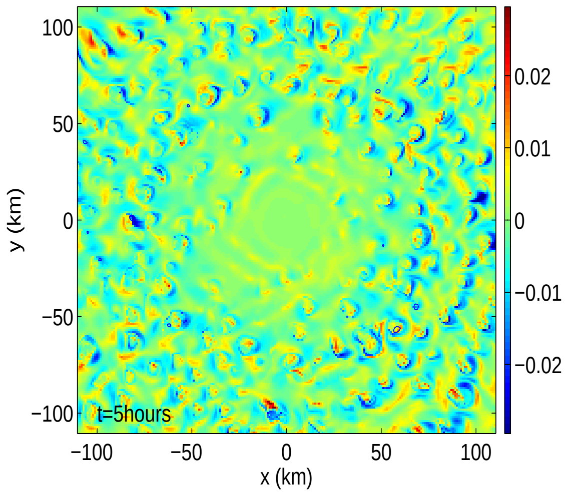

(b)

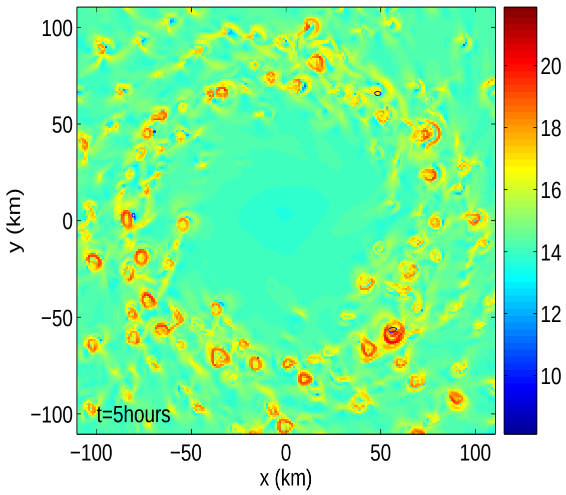

(c)

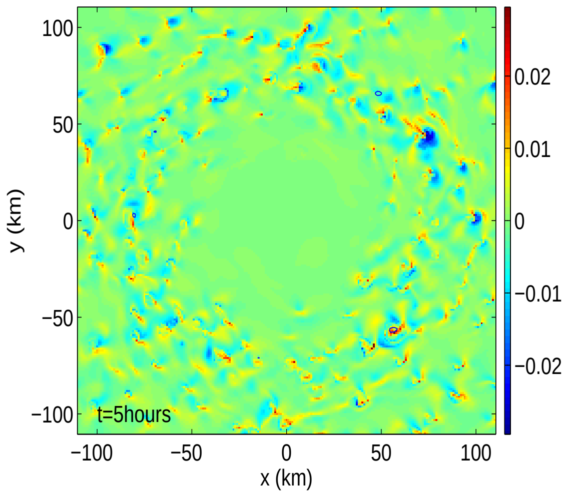

(d)

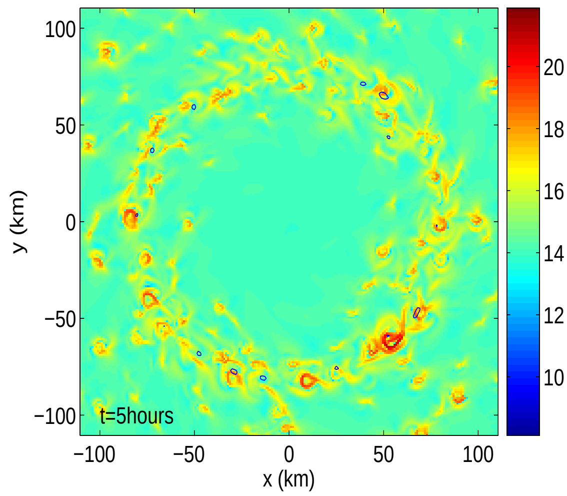

(e)

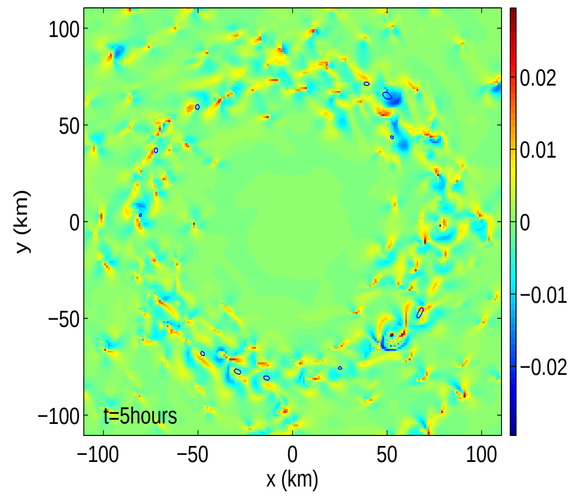

(f)

Figure 8.2: Planar FTLE fields (left column) and planar Ψ_{22} (right column) fields at z-levels of 1 km (a,b), 4 km (c,d), and 7 km (e,f) with 1 hour integration time and vorticity contours overlaid at initial time of 5 hours

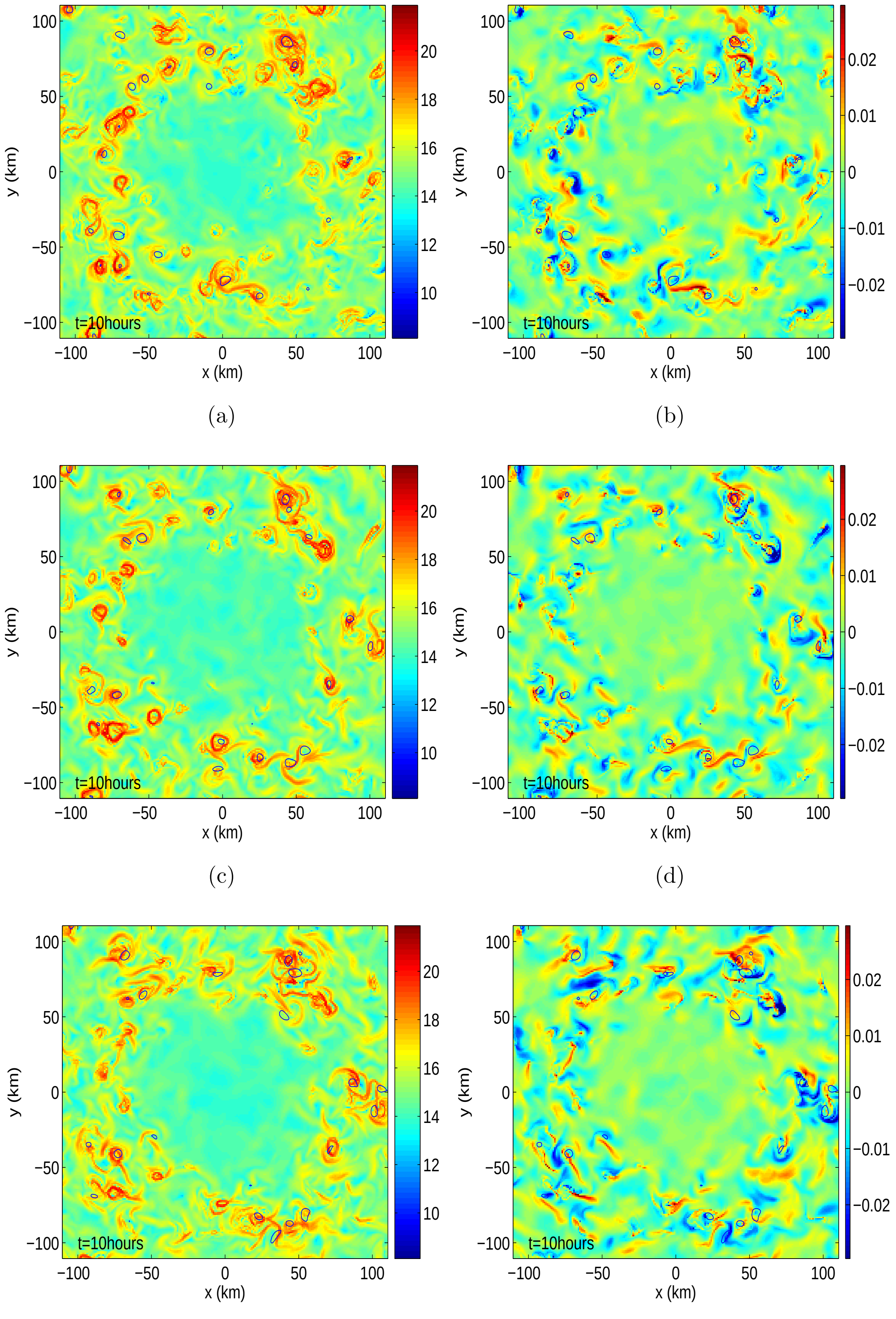

(a) (b)

(c) (d)

(e) (f)

Figure 8.3: Planar FTLE fields (left column) and planar Ψ_{22} (right column) fields at z-levels of 1 km (a,b), 4 km (c,d), and 7 km (e,f) with 1 hour integration time and vorticity contours overlaid at initial time of 10 hours

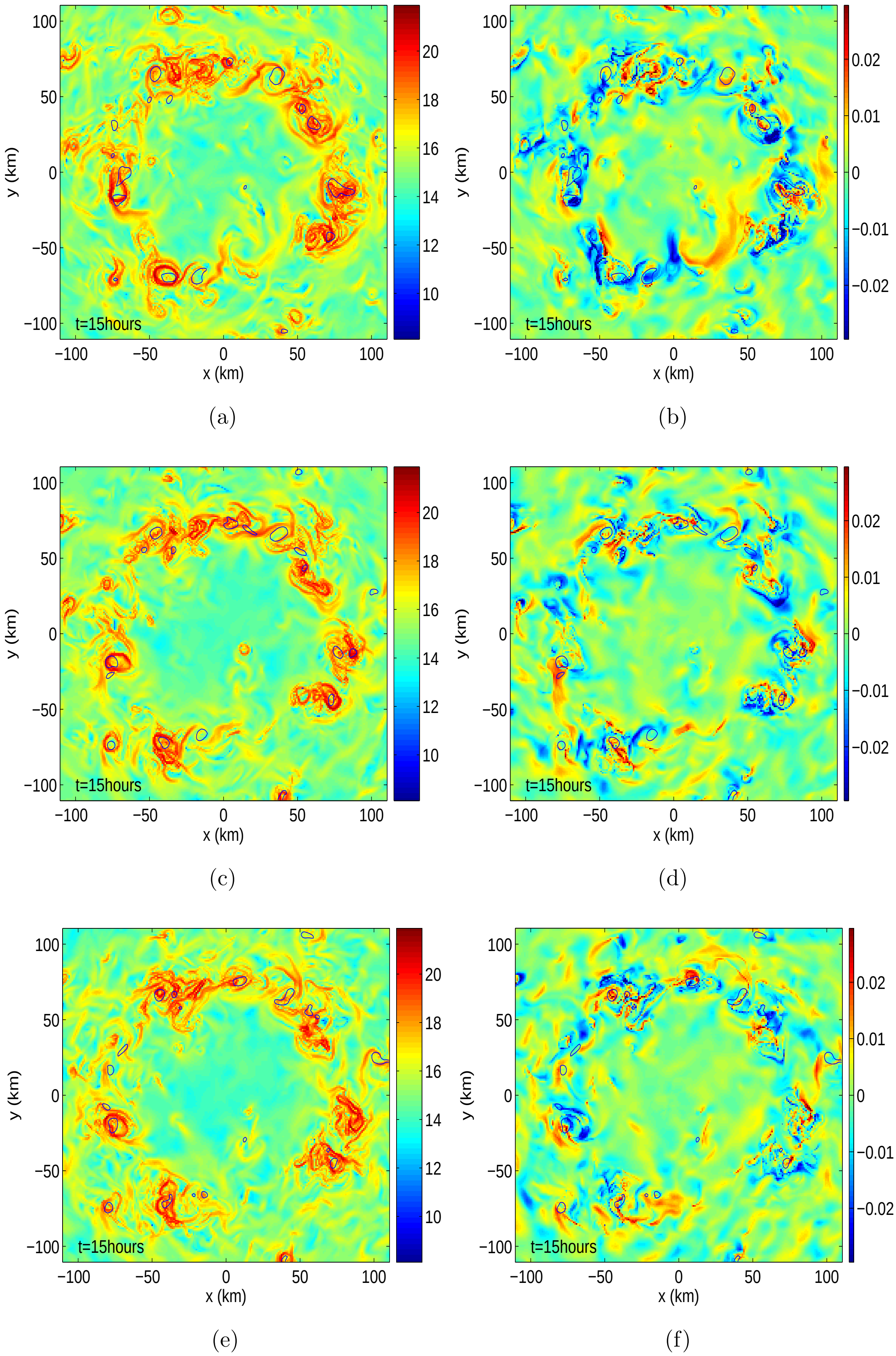

Figure 8.4: Planar FTLE fields (left column) and planar Ψ_{22} (right column) fields at z-levels of 1 km (a,b), 4 km (c,d), and 7 km (e,f) with 1 hour integration time and vorticity contours overlaid at initial time of 15 hours.

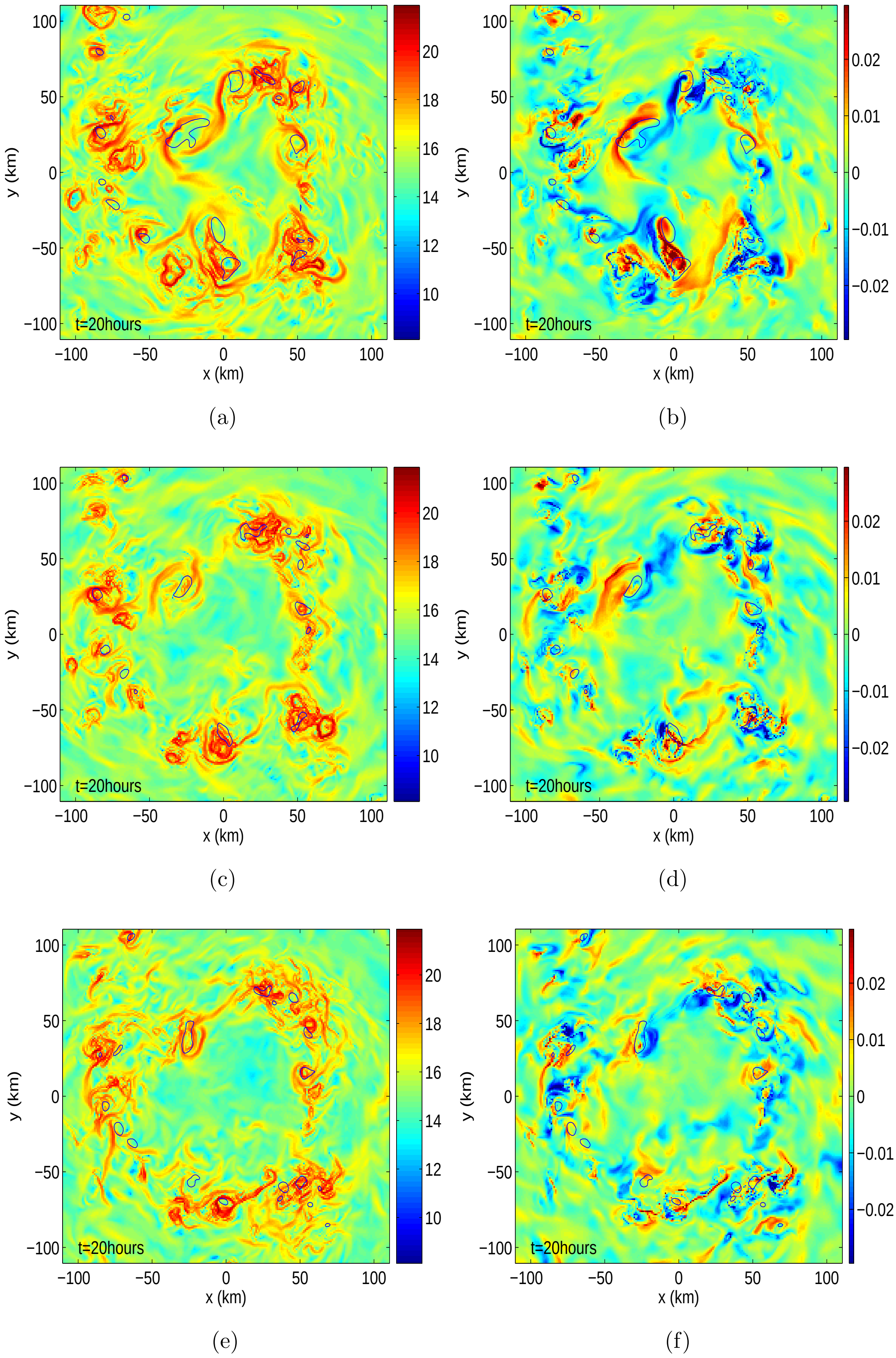

Figure 8.5: Planar FTLE fields (left column) and planar Ψ_{22} (right column) fields at z-levels of 1 km (a,b), 4 km (c,d), and 7 km (e,f) with 1 hour integration time and vorticity contours overlaid at initial time of 20 hours

Eyewall formation

At 15 hours, the lattice structure has broken down (Figure 8.4), and at 20 hours (Figure 8.5), the number of mesovortices has been greatly reduced as many mergers and annihilations have occured. Triangular and square patterns formed by the dominant LCS's show that the remaining structural asymmetries are dominated by wavenumbers 3 and 4. Higher potential temperature air has entered into the core, and the breaks in the LCS lattice open pathways for the transport of material to the core. The fields between 20 and 30 hours initial times are shown in Figures 8.6 and 8.7.

Generally, the domain of influence of each mesovortex is determined by the length of the manifolds emanating from it. During the crystalization phase, e.g. at 10 hours (Figure 8.3), the manifolds extend only to adjacent VHT's, and do not control any transport beyond the adjacent VHT's. By contrast, at 20 hours (Figure 8.5), the strength of the LCS's is much more intense, and some hyperbolic manifolds reach a length of over 50 km. The position of the longest manifold observable in Figures 8.6 and 8.7 is a connecting structure between mesovortices on opposite sides of the eventual primary vortex, which shows that the VHT's do not have interactions only with adjacent VHT's, but act along flow boundaries that will eventually define the axisymmetric vortex. At this stage, the set of LCS's do not completely enclose the eye, but gaps in the annulus remain which allow transport across the inner core boundary. At 50 hours, the gaps have closed and the eyewall formation is completed.

In [MNSP09] it is noted that as asymetries develop, the higher wavenumber asymetries appear first, but then disappear as the storm evolves toward a single vortex, whereas the low wavenumber asymmetries remain even after the storm has reached a steady vortex state. In our simulation, at 20 hours the wavenumber 4 asymmetry remains.

The structure of the VHT's in our 3D study is quite different from the 2D study of [PMFS03] and other studies in fluid mechanics, because of the lack of complete enclosure and presence of convection. In the 2D case, the vortex grows as it entrains additional fluid, and then splits a trailing shear layer of outflow from the vortex, often resulting in splitting into multiple vortices [OD10]. In the study of [PMFS03], the dominant vortex grows as it entrains the other vortex. For VHT interaction, we see that the size of VHT's generally grows as their entrainment of fluid increases. However, the open top of the VHT allows rising air to exit above $z = 10$ km, while there are two inflows present, at the sea surface and at $z = 6 - 9$ km [MNCS06, HMD04].

The role of the manifolds also extends beyond entrainment and interaction, and helps to dictate movement of VHT's relative to the mean flow as a boundary with friction. For counterclockwise motion, a VHT located radially inward from an LCS will move slower than the mean flow, while an LCS located radially outward moves faster. This can lead to a merger or splitting of nearby LCS's as they move upstream or downstream relative to each other.

8.4.2 Diabatic vortex merger

During the time period from 20 hours to 30 hours, several prominant vortices remain intact for longer than the normal 1 hour lifecycle and reach diameters of about 30 km. The merger of weaker vortices into the stronger vortex is illustrated in Figure 8.6, and can be clearly seen in an animation of the images.

A prominant vortex, labeled A in Figure 8.6 at 20 hours undergoes two types of mergers in the next 10 hour period. First, the vortex merges with smaller vortices that are located radially outward by a process of anihilation of the smaller vortices. The high vorticity in the outer vortices is filtered and contained within a tangle of manifolds. The outer vortices merge as the tangle unfolds into a single manifold at 24 hours. Merger of this new vortex with the inner vortex occurs at 26 hours when the manifolds unwind and release the vortex from its protective core in a pinchoff.

After the vortex has no manifold protecting it from interaction, it merges through a nearby tangle and becomes an elongated region of vorticity, which forms a portion of the eventual eyewall. The merger occurs first between 26 and 28 hours, and again between 28 and 30 hours. After the merger, the manifolds that protected the vortices have unwound and are located radially inward from the elongated vortex, now serving as a barrier to the center of the storm. The elongation and merger of primary VHT's is coincident with a higher rate of rotation. The VHT travels about one half rotation about the storm center for each 2 hour segment during the period from 20 to 26 hours, while it travels a full rotation during a 2 hour period from 28 hours to 30 hours, which indicates that an increase in angular velocity is a result of the upscale organization of vorticity through VHT interaction. Note that the length of the manifolds during the period of slower rotation is longer than the distance travelled by a trajectory during a 1 hour integration time, and that the coherent structures are far more resillient than the 1 hour lifetimes of VHT's. The tight closure of manifolds around a VHT eliminates interaction, while the unwinding allows additional entrainment by the VHT, which is subsequently pinched off from the manifold.

8.5 Concluding remarks

We have shown that during the intensification phase of a hurricane, the dynamics of VHT's play a crucial role in the formation of a (nearly) symmetric eyewall. Lagrangian coherent structures were located which dictate the transport of particle trajectories, and hence energy, to the hurricane core. Localized VHT's entrain air with high potential temperature, but the existence of hyperbolic LCS's surrounding the VHT's form a lattice that prohibits interaction between mesovortices. As the higher wavenumber asymetries begin to vanish, it is these LCS's that provide a pathway for the transport of energy to the core, while still forming a protective barrier around the core. The 3D nature of the structures shows that their role in the interaction of VHT's and in the organization of transport to the core is vital for the intensification process, perhaps more vital than WISHE which occurs only near the sea-surface.

Though this study has been conducted using model data calculated from an idealized initialization, our 3D Lagrangian methods resultted in 3D continuous LCS's persisting over varying initial time. The lengths of the manifolds suggest that the choice of integration time must be well adapted to the time-dependence of the storm data, but a proper choice of scales is certainly a reasonable adaptation of any method. The methods used in this study are applicable to any time-dependent vortex flows, and may uncover aspects of transport that have been unattainable by other methods. In particular, the application to intensifying storms in the crucial cases of African Easterly waves and a sheared tropical cyclone will provide insight into real storm intensification. In addition, the methods can be used to investigate interaction of a primary vortex with environmental flow.

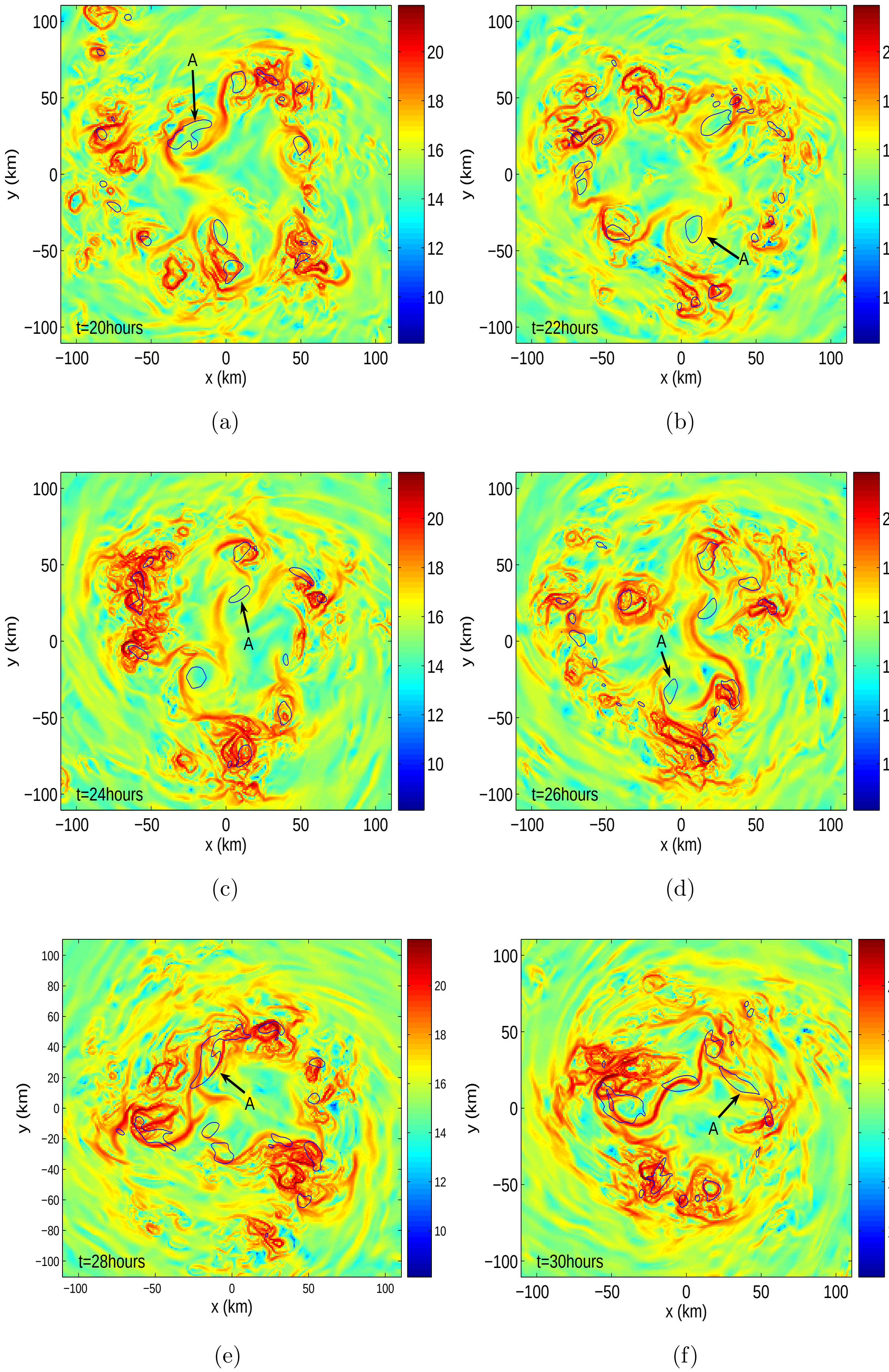

Figure 8.6: Planar FTLE fields with 1 hour integration time and vorticity contours overlaid at times from 20 hours to 30 hours every 2 hours.

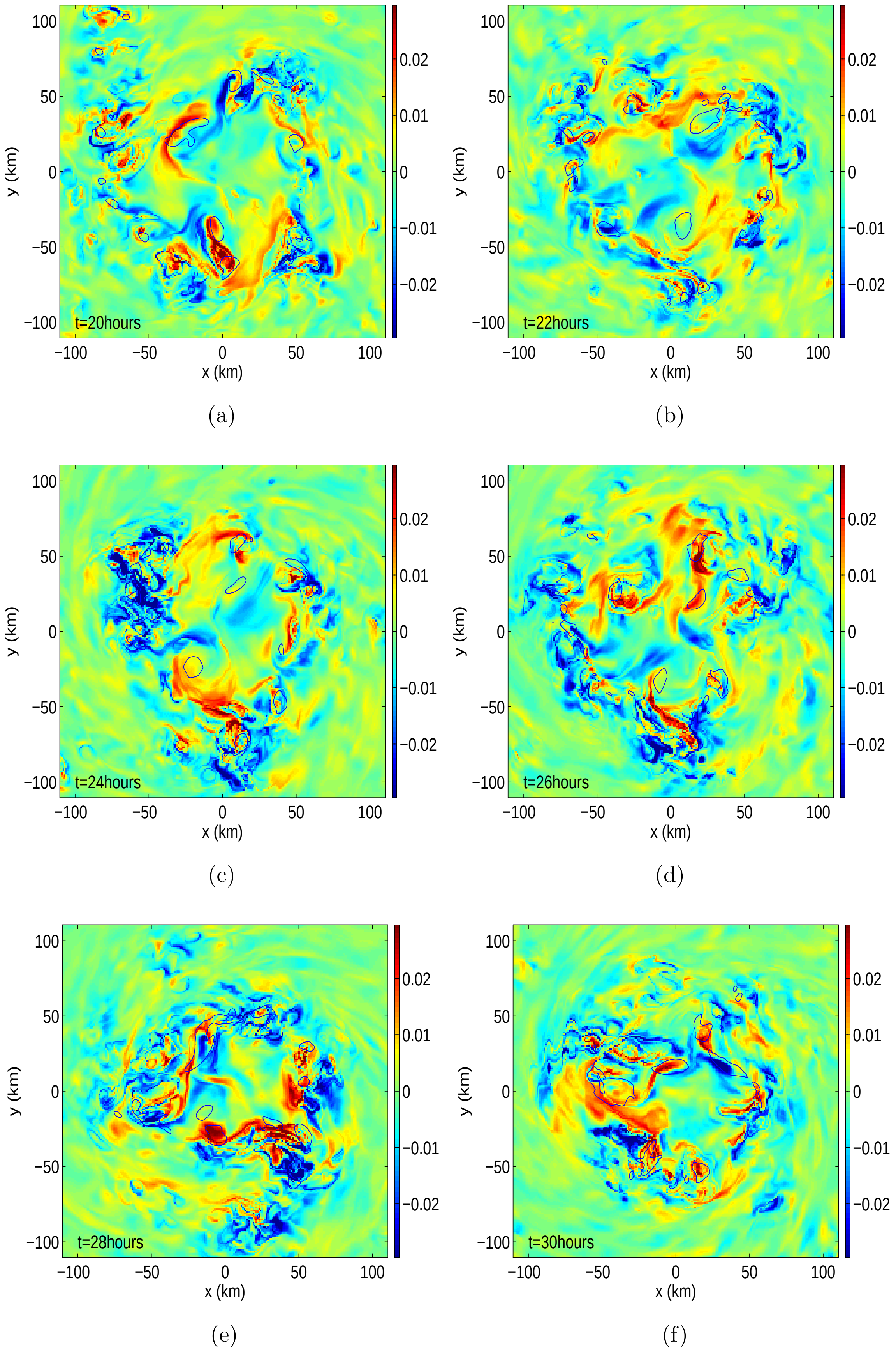

Figure 8.7: Planar Ψ_{22} fields with 1 hour integration time and vorticity contours overlaid at times from 20 hours to 30 hours every 2 hours.

Chapter 9

Conclusions

This study has introduced many concepts from dynamical systems pertaining to finite time transport in time-dependent flows to the field of tropical cyclone dynamics. The challenges of atmospheric data sets and tropical cyclones required the adaptation of many of the techniques and development of new techniques. Additionally, ideas from image processing have been used to viualize results, but still in a limited way.

There are many key advances and more questions that arise as a result of this study. The advances in Lagrangian dynamics lead to alternative methods with improved algorithms over existing Lagrangian methods. The applications of the methods to atmospheric models provide new methods of data analysis, which lead to new ideas about the dynamics and mixing that are present during a TC lifecycle.

Mathematically, the ideas presented here extend many of the methods in Lagrangian dynamics to a moving time frame and a 3D domain, which allows the analysis of mixing on intermediate time scales. The adaptation to the difficult domains and aspect ratios of atmospheric data sets along with the time scale problem was the main focus of the axisymmetric study. A variety of mixing rates were adapted and found to be meaningful indicators of hurricane intensity. For the barotropic model, high shear led to the use of a decomposition of the Lagrangian flow separation into hyperbolic and shearing components. Time dependent mixing rates were developed that measured transport across shear lines. The ideas of a moving time frame from the axisymmetric study were again used in the study and shown to be appropriate for a variety of flows. The key result of the study was that the question of whether persistent coherent structures could exist in dominant shear was answered affirmatively, and the structures were shown to have a tremendous impact on transport, and subsequent vortex breakdown. The 2D shear separation was extended to 3D, and a computational algorithm for extracting 3D fields followed after a specific coordinate transformation and rotation. The decomposition of the Lagrangian separation into three hyperbolic and three shearing components was crucial for extracting a continuous in time hyperbolic surface during a mature state that was not seen by other methods. The 3D method was shown to be particularly useful for atmospheric data sets due to the aspect ratio. Additional ridge extraction methods were developed that extracted the nearly cylindrical 3D surface. In the dynamical eyewall study, the methods were extended across varying initial time to produce a time-dependent eye-eyewall interface. The ridge extraction algorithms were automated over varying images to produce a continuously evolving structure. The ridge extraction algorithm was aided by the use of Fourier descriptors, which provided a natural data reduction to a shape-based coordinate over varying z-levels and initial times. Additional data analysis on z-levels showed a significant data reduction on the storm as a whole. The study of VHT interaction had the key mathematical result that hyperbolic structures shown to exist between vortices determine the later interaction, and in many cases annihilation. Symmetries were also shown to exist within the Lagrangian structures that are not evident using other methods, giving a new perspective on the formation of a primary vortex from mesovortices.

The use of the new mathematical tools developed here and by others have shown significant scientific results on the behavior of TC's. In the axisymmetric study, short time fluctuations in intensity were shown to be caused by mixing episodes. The time frame of the events support the argument that gravity waves causing local buoyancy in the eye promote a transfer of energy that leads to higher intensity. The study on the barotropic model shows that the interaction of mesovortices is determined by hyperbolic structures that persist through shear. Moreover, the length of the structures determines the degree of interaction, and may shield the mesovortices from environmental factors. The 3D eyewall study, while mostly mathematical, showed that the eye-eyewall boundary was an almost closed hyperbolic surface, and the boundary dictated the trajectory transport between the two regions. An extension to varying initial time in the time-dependent eyewall study showed that the asymetries of the eyewall could be characterized over varying time, and showed the degree of axisymmetry on the inner core from a transport perspective durng a mature state. The VHT study showed that hyperbolic structures were present and abundant during the intensification phase, and dictated the interaction of mesovortices. The hyperbolic LCS's provided a mechanism for the upscale organization of vorticity. The number of mesovortices and hyperbolic structures show the loss of higher wavenumber asymmetries during the transition to a mature storm.

Though many questions have been answered by this study, many remain. Specifically, the use of these techniques on real data during intensification has the opportunity to drive a great amount of future research that can increase our knowledge of TC intensification much further. The time-scale flexibility and methods for handling difficult 3D data sets have the potential to confirm new theories such as marsupial theory, and may show the importance of environmental factors to the strength and stability of the inner core. Additional use of data reduction and image processing may also show structural properties of the LCS's that are important for storm development.

Bibliography

[ABC+97] V. Artale, G. Boffetta, A. Celani, M. Cencini, and A. Vulpiani. Dispersion of passive tracers in closed basins: Beyond the diffusion coefficient. *Phys. Fluids*, 9:3162–3171, 1997.

[AJFOGL96] T. M. Antonsen Jr., Z. Fan, E. Ott, and E. Garcia-Lopez. The role of chaotic orbits in the determination of power spectra of passive scalars. *Phys. Fluids*, 8:3094–3104, 1996.

[AM78] D. G. Andrews and M. E. McIntyre. An exact theory of nonlinear waves on a Lagrangian mean flow. *J. Fluid Mech.*, 89:609–646, 1978.

[BE97] M. Bister and K. Emanuel. The genesis of Hurricane Guillermo:TEXMEX analyses and a modeling study. *Mon. Wea. Rev.*, 125:2662–2882, 1997.

[BE98] M. Bister and K. Emanuel. Dissipative heating and hurricane intensity. *Meteor. Atmos. Phys.*, 65:233–240, 1998.

[BM91] P. G. Black and F. D. Marks. The structure of an eyewall meso-vortex of Hurricane Hugo (1989). In *19th Conf. on Hurricanes and tropical Meteorology proceedings*, pages 579–582, Miami, FL, 1991. Amer. Meter. Soc.

[Bra02] S. A. Braun. A cloud-resolving simulation of Hurricane Bob (1991): Storm structure and eyewall buoyancy. *Mon. Wea. Rev.*, 130:1573–1592, 2002.

[BW92] P. G. Black and H. E. Willoughby. The concentric eyewall cycle of Hurricane Gilbert. *Mon. Wea. Rev.*, 120:947–957, 1992.

[CBY03] Y. Chen, G. Brunet, and M. K. Yau. Spiral bands in a simulated hurricane. Part II: Wave activity diagnostics. *J. Atmos. Sci.*, 60:1239–1256, 2003.

[CK94] G. F. Carnevale and R. C. Kloosterziel. Lobe shedding from propogating vortices. *Physica D*, 76(1-3):147–167, 1994.

[CPMB07] T. A. Cram, J. Persing, M. T. Montgomery, and S. A. Braun. A Lagrangian trajectory view on transport and mixing processes between the eye, eyewall, and environment using a high resolution simulation of hurricane Bonnie (1998). *Journal of Atmospheric Sciences*, 64:1835–1856, 2007.

[CW00] C. Coulliette and S. Wiggins. Intergyre transport in a wind-driven, quasi-geostrophic double gyre: An application of lobe dynamics. *Nonlin. Proc. Geophys.*, 7:59–85, 2000.

[CY01] Y. Chen and M. K. Yau. Spiral bands in a simulated hurricane. Part I: Vortex Rossby wave verification. *J. Atmos. Sci.*, 58:2128–2145, 2001.

[dFHG04] F. d'Ovidio, V. Fernandez, and E. Hernandez-Garcia. Mixing structures in the Mediterranean Sea from finite-size Lyapunov exponents. *Geophy. Res. Lett.*, 31(17):L17203, 2004.

[DG04] J. O. Dabiri and M. Gharib. Fluid entrainment by isolated vortex rings. *Journal of Fluid Mechanics*, 511:311–331, 2004.

[DMW09] T. J. Dunkerton, M. T. Montgomery, and Z. Wang. Tropical cyclogenesis in a tropical wave critical layer: easterly waves. *Atmos. Chem. Phys.*, 9:5587–5646, 2009.

[Dud93] J. Dudhia. A non-hydrostatic version of the Penn State-NCAR mesoscale model: Validation tests and simulation of an atlantic cyclone and cold front. *Mon. Wheather Rev.*, 8:1493–1513, 1993.

[Dun80] T. Dunkerton. A Lagrangian mean theory of wave, mean- flow interaction with applications to nonacceleration and its breakdown. *Rev. Geophys.*, 18(2):387–400, 1980.

[DW96] J. Duan and S. Wiggins. Fluid exchange across a meandering jet with quasiperiodic variability. *J. Phys. Oceanogr.*, 26:1176–1188, 1996.

[ECL02] J. D. Eldredge, T. Colonius, and A. Leonard. A vortex particle metod for two-dimensional compressible flow. *Journal of Computational Physics*, 179(2):371–399, 2002.

[Ema97] K. A. Emanuel. Some aspects of inner core dynamics and energetics. *J. Atmos. Sci.*, 54:1016–1026, 1997.

[ENB94] K. A. Emanuel, J. D. Neelin, and C. S. Bretherton. On large scale circulations in convecting atmosphere. *Q. J. R. Meteorol. Soc.*, 120:1111–1143, 1994.

[FCFD95] K. S. Fine, A. C. Cass, W. G. Flynn, and C. F. Driscoll. Relaxation of 2D turbulence to vortex crystals. *Phys. Rev. Lett.*, 75:3277–3280, 1995.

[FJ69] N. L. Frank and H. M. Johnson. Vortical cloud systems over the tropical Atlantic during the 1967 hurricane season. *Mon. Wea. Rev.*, 97:124–129, 1969.

[FR99] W. M. Frank and E. A. Ritchie. Effects of environmental flow upon tropical cyclone structure. *Mon. Wea. Rev.*, 127:2044–2061, 1999.

[FR01] W. M. Frank and E. A. Ritchie. Effects of vertical wind shear on the intensity and structure of numerically simulated hurricanes. *Mon. Wea. Rev.*, 129:2249–2269, 2001.

[GDS95] G. Grell, J. Dudhia, and D. Stauffer. A description of the fifth generation Penn State-NCAR mesoscale model (MM5). *NCAR Tech. Note NCAR/TN*, 398:1–138, 1995.

[GGTH07] C. Garth, F. Gerhardt, X. Trioche, and H. Hagen. Efficient computation and visualization of coherent structures in fluid flow applications. *IEEE Transactions on Visualization and Computer Graphics*, 13(6):1464–1471, 2007.

[GRH07] M. A. Green, C. Rowley, and G. Haller. Detection of Lagrangian Coherent Structures in 3D Turbulence. *J. Fluid Mech.*, 572:111–120, 2007.

[Hal00] G. Haller. Finding finite-time invariant manifolds in two-dimensional velocity fields. *Chaos*, 10:99–108, 2000.

[Hal01a] G. Haller. Distinguished material surfaces and coherent structures in three-dimensional fluid flows. *Physica D*, 149:248–277, 2001.

[Hal01b] G. Haller. Lagrangian structures and the rate of strain in a partition of two-dimensional turbulence. *Physics of Fluids*, 13:3365–3385, 2001.

[Hal02] G. Haller. Lagrangian coherent structures from approximate velocity data. *Physics of Fluids*, 14:1851–1861, 2002.

[Hal04] G. Haller. Exact theory of unsteady separation for two-dimensional flows. *J. Fluid Mech*, 512:257–311, 2004.

[Hal05] G. Haller. An objective view of a vortex. *J. Fluid Mechanics*, 525:1–26, 2005.

[HI03] G. Haller and R. Iacono. Stretching, alignment, and shear in slowly varying velocity fields. *Physical Review E*, 68:056304–1–6, 2003.

[HJLB09] R. A. Houze Jr., W. C. Lee, and M. M. Bell. Convective contribution to the genesis of Hurricane Ophelia (2005). *Mon. Wea. Rev.*, 137:2778–2800, 2009.

[HMD04] E. A. Hendricks, M. T. Montgomery, and C. A. Davis. On the role of vortical hot towers in tropical cyclone formation. *J. Atmos. Sci.*, 61:1209–1232, 2004.

[HMG01] M. Huber, J. C. McWilliams, and M. Ghil. A climatology of turbulent dispersion in the troposphere. *Journal of the Atmospheric Sciences*, 58:2377–2394, 2001.

[HP97] G. Haller and A. Poje. Finite time transport in aperiodic flows. *Physica D*, 119:352–380, 1997.

[HS86] J. J. Hack and W. H. Schubert. Nonlinear response of atmospheric vortices to heating by organized cumulus convection. *J. Atmos. Sci.*, 43:1559–1573, 1986.

[HS09] E. A. Hendricks and W. H. Schubert. Transport and mixing in idealized barotropic hurricane-like vortices. *Quart. J. Roy. Meteor. Soc*, 135:1456–1470, 2009.

[HY00] G. Haller and G. Yuan. Lagrangian coherent structures and mixing in two-dimensional turbulence. *Physica D*, 147:352–370, 2000.

[ISW02] K. Ide, D. Small, and S. Wiggins. Distinguished hyperbolic trajectories in time-dependent fluid flows: analytical and computational approach for velocity fields defined as data sets. *Nonlinear Processes in Geophysics*, 9(3/4):237–263, 2002.

[JL01] B. Joseph and B. Legras. Relation between kinematic boundaries, stirring, and barriers for the antarctic polar vortex. *J. Atmos. Sci.*, 59:1198–1212, 2001.

[JW02] C. K. R. T. Jones and S. Winkler. Invariant manifolds and Lagrangian dynamics in the ocean and atmosphere. *Handbook of dynamical systems*, 2:55–92, 2002.

[KE01] J. Kossin and M. D. Eastin. Two distinct regimes in the kinematic and thermodynamic structure of the hurricane eyewall. *J. Atmos. Sci.*, 58:1079–1090, 2001.

[KL02] T. Y. Koh and B. Legras. Hyperbolic lines and the stratospheric polar vortex. *Chaos*, 12:382–394, 2002.

[KS01] J. Kossin and W. H. Schubert. Mesovortices, polygonal flow patterns, and rapid pressure falls in hurricane-like vortices. *J. Atmos. Sci.*, 58:2196–2209, 2001.

[Lek03] F. Lekien. *Time-dependent dynamical systems and geophysical flows.* PhD thesis, California Institute of Technology, 2003.

[LH82] B. M. Lewis and H. F. Hawkins. Polygonal eyewalls and rainbands in hurricanes. *Bull. Amer. Meteor. Soc.*, 63:1294–1300, 1982.

[Lin98] T. Lindeberg. Edge detection and ridge detection with automatic scale selection. *International Journal of Computer Vision*, 30(2):117–154, 1998.

[LL04] F. Lekien and N. Leonard. Dynamically consistent Lagrangian coherent structures. In S. Bocaletti, B. J. Gluckman, J. Kurths, L. M. Pecora, R. Meucci, and O. Yordanov, editors, *8th experimental chaos conference*, volume 742, pages 132–139, Florence, Italy, 2004.

[MBAB06] M. T. Montgomery, M. M. Bell, S. A., and M. Black. Hurricane Isabel (2003): New insights into the physics of intense storms. Part I: Mean vortex structure and maximum intensity estimates. *Bull. Amer. Met. Soc.*, 87:1349–1354, 2006.

[McI80] M. E. McIntyre. *Toward a Lagrangian-mean description of stratospheric circulations and chemical transports*. Phil. Trans. Roy. Soc., London, series a edition, 1980.

[McW84] J. C. McWilliams. The emergence of isolated coherent vortices in turbulent flow. *J. Fluid Mech.*, 140:21–43, 1984.

[ME98] M. T. Montgomery and J. Ensgonio. Tropical cyclogenesis via convectively forced vortex Rossby waves in a three-dimensional quasigeostrophic model. *J. Atmos. Sci.*, 55:3176–3207, 1998.

[MHP+07] M. Mathur, G. Haller, T. Peacock, J. E. Ruppert-Felsot, and H. L. Swinney. Uncovering the Lagrangian skeleton of turbulence. *Physical review letters*, 98:144502–1–144502–4, 2007.

[ML97] M. T. Montgomery and C. Lu. Free waves on barotropic vortices. Part I: Eigenmode structure. *J. Atmos. Sci.*, 54:1868–1885, 1997.

[MNCS06] M. T. Montgomery, M. E. Nichols, T. A. Cram, and A. B. Saunders. A vortical hot tower route to tropical cyclogenesis. *J. Atmos. Sci.*, 63:355–386, 2006.

[MNSP09] M. T. Montgomery, V. S. Nguyen, R. K. Smith, and J. Persing. Do tropical cyclones intensify by WISHE? *Q. J. R. Meteorol. Soc.*, 135:1697–1714, 2009.

[MSW04] A. Mancho, D. Small, and S. Wiggins. Computation of hyperbolic trajectories and their stable and unstable manifolds for oceanographic flows represented as data sets. *Nonlinear Processes in Geophysics*, 11(1):17–33, 2004.

[MSWI03] A. M. Mancho, D. Small, S. Wiggins, and K. Ide. Computation of stable and unstable manifolds of hyperbolic trajectories in two-dimensional, aperiodically time-dependent vector fields. *Physica D*, 182:188–222, 2003.

[Mur86] T. Muramatsu. The structure of polygonal eye of a typhoon. *J. Meteor. Soc. Japan*, 64:913–921, 1986.

[MVD02] M. T. Montgomery, V. A. Vladimirov, and P. V. Denissenko. An experimental study on hurricane mesovortices. *J. Fluid Mech.*, 471:1–32, 2002.

[MW98] N. Malhotra and S. Wiggins. Geometric structures, lobe dynamics, and Lagrangian transport in flows with aperiodic time-dependence, with applications to Rossby wave flows. *J. Nonlinear Science*, 8:401–456, 1998.

[Nak96] N. Nakamura. Two-dimensional mixing, edge formation, and permeability diagnosed in area coordinates. *J. Atmos. Sci.*, 53:1524–1537, 1996.

[NM02] D. S. Nolan and M. T. Montgomery. Nonhydrostatic, three-dimensional perturbations to balanced, hurricane-like vortices. Part I: Linearized formulation, stability and evolution. *J. Atmos. Sci.*, 59:2989 3020, 2002.

[NSM08] S. A. Nguyen, R. K. Smith, and M. T. Montgomery. Tropical-cyclone intensification and predictability in three dimensions. *Q. J. R. Meterol. Soc.*, 134:563–582, 2008.

[OD10] C. O'Farrell and J. O. Dabiri. A Lagrangian approach to identifying vortex pinch-off. *Chaos*, 20:017513–1–9, 2010.

[Ott89] J. M. Ottino. *The kinematics of mixing: stretching, chaos, and transport.* Cambridge University Press, 1989.

[PH99] A. C. Poje and G. Haller. Geometry of cross-stream mixing in a double-gyre ocean model. *Journal of Physical Oceanography*, 29(8):1649–1665, 1999.

[PM03] J. Persing and M. T. Montgomery. Hurricane superintensity. *J. Atmos. Sci.*, 60:2349–2371, 2003.

[PMFS03] R. Prieto, B.D. McNoldy, S.R. Fulton, and W.H. Schubert. A classification of binary tropical-cyclone-like vortex interactions. *Mon. Wea.Rev.*, 131:2656–2666, 2003.

[Pro99] A. Provenzale. Transport by coherent barotropic vortices. *Annual Review of Fluid Mechanics*, 31:55–93, 1999.

[RD09] B. Rutherford and G. Dangelmayr. A 3D Lagrangian hurricane eye-eyewall computation. Preprint, submitted to Quart. J. Roy. Met. Soc., 2009.

[RDP+09] B. Rutherford, G. Dangelmayr, J. Persing, M. Kirby, and M. T. Montgomery. Lagrangian mixing in an axisymmetric hurricane model. Preprint, submitted to Atmos. Chem. Phys, 2009.

[RDP+10] B. Rutherford, G. Dangelmayr, J. Persing, W. H. Schubert, and M. T. Montgomery. Advective mixing in a nondivergent barotropic hurricane model. *Atmos. Chem. Phys.*, 10:475–497, 2010.

[RE87] R. Rotunno and K. Emanuel. An air-sea interaction theory for tropical cyclones. part ii:evolutionary study using a nonhydrostatic axisymmetric numerical model. *Journal of the Atmospheric Sciences*, 44:542–561, 1987.

[RH97] E. A. Ritchie and G. Holland. Scale interaction during the formation of typhoon Irving. *Mon. Wea. Rev.*, 125:1377–1396, 1997.

[RMB05] P. D. Reasor, M. T. Montgomery, and L. Bosart. Mesoscale observations of the genesis of Hurricane Dolly (1996). *J. Atmos. Sci.*, 62:3151–3171, 2005.

[RMMJG99] P. D. Reasor, M. T. Montgomery, F. D. Marks Jr., and J. F. Gamache. Low wavenumber structure and evolution of the hurricane inner core observed by airborne dualDoppler radar. *Mon. Wea. Rev.*, 128:1653–1680, 1999.

[RMN09] M. Riemer, M. T. Montgomery, and M. E. Nichols. A new paradigm for intensity modification fo tropical cyclones: Thermodynamic impact of vertical wind shear on the inflow layer. *Atmospheric Chem. Phys. Discuss.*, 9:10711–10755, 2009.

[RMPJ99] A. Rogerson, P. D. Miller, L. J. Pratt, and C. K. R. T. Jones. Lagrangian motion and fluid exchange in a barometric meandering jet. *J. Phys. Oceanogr.*, 10:2635–2655, 1999.

[Rol65] H. Roll. *Physics of the marine atmosphere.* Academic Press, 1965.

[Saf81] P. G. Saffman. Dynamics of vorticity. *Journal of Fluid Mechanics*, 106:49–58, 1981.

[Sam92] R. M. Samelson. Fluid exchange across a meandering jet. *J. Phys. Oceanogr.*, 22:431–440, 1992.

[SDM06] S. C. Shadden, J. O. Dabiri, and J. E. Marsden. Lagrangian analysis of fluid transport in empirical vortex rings. *Physics of Fluids*, 18(4):047105–1–11, 2006.

[SH82] W. H. Schubert and J. J. Hack. Inertial stability and tropical cyclone development. *J. Atmos. Sci.*, 39:1687–1697, 1982.

[SH03] E. Shuckburgh and P. Haynes. Diagnosing transport and mixing using a tracer-based coordinate system. *Physics of Fluids*, 15:3342–3357, 2003.

[SH08] A. Surana and G. Haller. Ghost manifolds in slow-fast systems, with applications to unsteady fluid flow separation. *Physica D*, 237:1507–1529, 2008.

[SH09] T. Sapsis and G. Haller. Inertial particle dynamics in hurricanes. *J. Atmos. Sci.*, 66:2481–2492, 2009.

[Sha92] K. Sharif. *Dynamics of a class of vortex rings.* PhD thesis, Stanford University, 1992.

[Sha06] S. Shadden. *A dynamical systems approach to unsteady flows.* PhD thesis, California Institute of Technology, 2006.

[SIJ08] H. Salman, K. Ide, and C. K. R. T. Jones. Using flow geometry for drifter deployment in Lagrangian data assimilation. *Tellus A.*, 60(2):321–335, 2008.

[SIM95] G. B. Smith II. and Montgomery. Vortex axisymmetrization and its dependence on azimuthal wavenumber or asymmetric radial structure changes. *Quart. J. Roy. Meteor. Soc.*, 121:1615–1650, 1995.

[SL92] K. Shariif and A. Leonard. Vortex rings. *Annual Review of Fluid Mechanics*, 24:U235–U279, 1992.

[SL02] D. R. Sotiropolous, F. Webster and T. C. Lackey. Experiments on Lagrangian transport in steady vortex-breakdown bubbles in a confined swirling flow. *Journal of Fluid Mechanics*, 466:215–248, 2002.

[SLM05] S. C. Shadden, F. Lekien, and J. E. Marsden. Definition and properties of Lagrangian coherent structures from finite-time Lyapunov exponents in two-dimensional aperiodic flows. *Physica D*, 212:271–304, 2005.

[SM93] L. J. Shapiro and M. T. Montgomery. A three-dimensional balance theory for rapidly rotating vortices. *J. Atmos. Sci.*, 50:3322–3335, 1993.

[Sma63] J. Smagorinsky. General circulation experiments with the primitive equation. I: The basic experiment. *Mon. Wea. Rev.*, 91:99–164, 1963.

[SMN09] R. K. Smith, M. T. Montgomery, and V. S. Nguyen. Tropical cyclone spin up revisited. *Q. J. R. Meteorol. Soc.*, 134:1385–1395, 2009.

[SMT$^+$99] W. H. Schubert, M. T. Montgomery, R. K. Taft, T. A Guinn, S. R. Fulton, J. P. Kossin, and J. P. Edwards. Polygonal eyewalls, asymmetric eye contraction, and potential vorticity mixing in hurricanes. *J. Atmos. Sci.*, 56:1197–1223, 1999.

[SMZ05] R. K. Smith, M. T. Montgomery, and H. Zhu. Buoyancy in tropical cyclones and other rapidly rotating atmospheric vortices. *Dyn. Atmos. Oceans*, 40:189–208, 2005.

[SS08] S. Shin and R. K. Smith. Tropical cyclone intensification and predictability in a minimal three-dimensional model. *Q. J. R. Meteorol. Soc.*, 134:1385–1395, 2008.

[TCH10] W. Tang, P. W. Chan, and G. Haller. Accurate extraction of LCS over finite domains, with application to flight safety analysis over Hong Kong International Airport. *Chaos*, 20:017502, 2010.

[TMH$^+$09] W. Tang, M. Mathur, G. Haller, D. Hahn, , and F. Ruggiero. Lagrangian coherent structures near a subtropical jet stream. *J.Atmos.Sci.*, preprint, 2009.

[TPGB00] G. M. Treece, R. W. Prager, A. H. Gee, and L. Berman. Surface interpolation from sparse sections using region correspondence. *IEEE Transactions on Medical Imaging*, 19(11):1106–1114, 2000.

[Tru54] C. Truesdell. *The kinematics of vorticity.* Indiana Uiversity Press, 1954.

[VHG02] G. A. Voth, G. Haller, and J. P. Gollub. Experimental measures of stretching fields in fluid mixing. *Physical Review Letters*, 88(25):254501, 2002.

[VT80] V. A. Vladimirov and V. F. Tarasov. Formation of a system of vortex filaments in a rotating liquid. *Izv. Akad. Nauk SSSR, Mekhanika Zhidkosti i Gaza*, 1:44–51, 1980.

[VTSG03] G. A. Voth, G. D. T.C. Saint, and J. Gollub. Mixing rates and symmetry breaking in two-dimensional chaotic flow. *Physics of Fluids*, 15:2560–2566, 2003.

[WD06] V. Wirth and T. J. Dunkerton. A unified perspective on the dynamics of axisymmetric hurricanes and monsoons. *J. Atmos. Sci.*, 63:2529–2547, 2006.

[Wig05] S. Wiggins. The dynamical systems approach to Lagrangian transport in oceanic flows. *Annual Review of Fluid Mechanics*, 37:295–328, 2005.

[Wil01] H. E. Willoughby. Tropical cyclone eye thermodynamics. *Mon. Wea. Rev.*, 126:3053–3067, 2001.

[YM02] H. Yamada and T. Matsui. Preliminary study of mutual slip-through of a pair of vortices. *Physics of Fluids*, 21(2):292–294, 2002.

[ZY02] Y. L. Zhang, D. L. and M. K. Yau. A multiscale numerical study of Hurricane Andrew (1992). Part V: Inner core thermodynamics. *Mon. Wea. Rev.*, 130:2745–2763, 2002.